Title

Dynamics of ice shelf rift propagation and iceberg calving inferred from geodetic and seismic observations

Author

Bassis, Jeremy N.

Publication Date

2007

UNIVERSITY OF CALIFORNIA, SAN DIEGO

Dynamics of Ice Shelf Rift Propagation and Iceberg Calving inferred from Geodetic and Seismic Observations

A dissertation submitted in partial satisfaction of the
requirements for the degree Doctor of Philosophy
in
Earth Sciences

by

Jeremy N. Bassis

Committee in charge:

J.B. Minster, Chair
H.A. Fricker, Co-Chair
Y. Fialko
F. Gilbert
D. Lubin
S. Nemat-Nasser

2007

The dissertation of Jeremy N. Bassis is approved, and it is acceptable in quality and form for publication on microfilm:

Co-Chair

Chair

University of California, San Diego

2007

After six years of graduate school, it is difficult to be anything other than jaded. This dissertation is dedicated to my grandparents, Sam and Sylvia Bassis, who after more than eight decades in this world, remain optimistic. While neither of them are scientists, their selflessness, interest and curiosity in the outside world make them not only ideal grandparents and human beings, but model scientists.

TABLE OF CONTENTS

LIST OF FIGURES

LIST OF TABLES

ACKNOWLEDGEMENTS

Over the past six and a half years that I have been a graduate student I have grown both older and fatter. I'm not sure about wiser or even smarter, but definitely more tired; it is those people that kept me going near the end, when all seemed hopeless, that I am most grateful to. In particular, I need to thank Christine, who helped whenever she could, even while desperately trying to finish her own dissertation. During those stressful months, Rokc was always happy and enthusiastic to see me, regardless of my mood and eagerly encouraged me to share her hobbies of eating meat, walking on the beach and finding stinky things to role in.

My parents and grandparents have always been supportive, although mystified why I would continue through to grade 23 without improved prospects for financial remuneration. Nonetheless, despite their misgivings, they never stopped being encouraging, even when they had no idea what I was working on or why. My father, in particular, has been exceptionally supportive over the past several months, emailing me high paying job postings that I would be qualified for, had I pursued a higher degree in something more useful than geophysics, such as physics or mathematics.

In addition to family and canine support, many at SIO and UCSD have helped me along the way. I owe a dept of gratitude to my committee members who provided many useful suggestions and criticisms along the way. I need to thank the chair of my committee, Bernard Minster who gave me the academic freedom to work on what I wanted, and more importantly, the freedom to make my own mistakes. This was a good student-adviser relationship because Bernard didn't burden me with an excess of advice, advice I probably would have ignored anyway (my parents will confirm that). I also would like to thank the co-chair of my committee, Helen Fricker, without whom I would never have gotten the opportunity to go to Antarctica or to study iceberg calving. Helen slogged through many early drafts of the dissertation providing needed, although not always appreciated, editorial advice that substantially improved the final document. It is also with Helen that I worked most closely and from whom I received the bulk of my guidance; although some of that advice was ignored. I would also like to thank the rest of my committee, Freeman Gilbert, Yuri Fialko, Dan Lubin and Sia Nemat-Nasser, all of whom provided encouragement and necessary criticism. Freeman Gilbert showed me that good scientific writing is not necessarily boring. Yuri shared with me the joys of fracture mechanics and Sia provided helpful suggestions about visco-elastic fracture. Dan explained the grim reality of the politics of climate change science.

Two additional people played a substantial role in shaping my dissertation but, unfortunately, are not officially committee members. Christina Hulbe was supposed to serve on my committee and admirably discharged her duties, but due to an administrative error, does not appear as an official committee member. Christina had the great fortitude and patience to spend four hours on the telephone in a hotel room listing to my presentation and participating in the defense, despite plans to leave for Antarctica the following week. Her careful criticism and encyclopedic knowledge of the glaciologic literature helped to put my work in a broader historical context. Richard Coleman, who should be a full committee member, was instrumental in getting funding for the field work on the Amery Ice Shelf. And despite being located in the opposite hemisphere, he taught me much about Geodesy and GPS processing while providing invaluable scientific guidance from his antipodal vantage point. Richard Coleman (unlike my very own parents) flew from Hobart, Tasmania to be present at my dissertation defense; a feat all the more remarkable since he was not an official committee member.

I am also indebted to all those who helped me during the Antarctic field season in which I participated. Mike Woolridge deserves special thanks because, as our field training officer, his duty was to keep me alive, something I'm exceptionally grateful for. I also learned a lot about explosives and a little bit about active source seismology from Mark Lackey and, his student, Kath McMahon. But none of the work I did would have been possible without the assistance and support from many people at Davis station. No less significant has been the participation of Dennis Darnell, Jim Behrens and Marianne Okal in subsequent field seasons. Without their expertise and dedication in the field, the data that forms the foundation of this dissertation would never have been collected. In the aftermath of field seasons, Yehuda Bock has been a tremendous help in processing GPS data and was kind enough to let me use RTD to process the GPS data collected in the field.

Finally, my fellow graduate students have enriched my experience at SIO over the past six years. It has been during the many discussions (and sometimes arguments) with Jasper Konter about things that I knew nothing about that I learned that the deep Earth is, surprisingly, interesting. I had many great discussions about inverse theory with my compatriot in the ICESat lab, Adriane Borsa. I also, incidentally, prevented him from running over and disemboweling a cow with a rented car during field work in Utah. These are the experiences that make graduate life worth it. But I also need to acknowledge those that make it possible. The staff at SIO have always been supportive and I must thank Karen Scott, not only for administrative advice and her knack for speedy reimbursements, but also for doing her best to make my life easier over the past six years.

Chapter 2, in full, has been published in Geophysical Research Letters, J.N. Bassis, H.A. Fricker, R. Coleman, J.B. Minster. Episodic propagation of a rift on the Amery Ice Shelf, East Antarctica. The dissertation author was the primary investigator and author of this paper.

VITA

2000	B.S., Physics, Pennsylvania State University
2000-2006	Research Assistant Scripps Institution of Oceanography, University of California, San Diego
2007	Ph.D., Earth Sciences Scripps Institution of Oceanography, University of California, San Diego.

PUBLICATIONS

J.N. Bassis, H.A. Fricker, R. Coleman, J.B. Minster, 2005: Episodic Propagation of a Rift on the Amery Ice Shelf, East Antarctica. *Geophysical Research Letters*, doi: 10.1029/2004GL022048

Fricker, H. A. and Bassis, J. N. and Minster, B. and MacAyeal, D. R.,2005:ICESat's new perspective on ice shelf rifts: The vertical dimension . *Geophysical Research Letters*, doi: 10.1029/2005GL025070

Fricker, H. A. and Young, N. W. and Coleman, R. and Bassis, J. N. and Minster, J.-B.., 2005:Multi-year monitoring of rift propagation on the Amery Ice Shelf, East Antarctica. *Geophysical Research Letters*, doi: 10.1029/2004GL021036

Martinez, M. and Harder, H. and Kovacs, T. A. and Simpas, J. B. and Bassis, J. et al.., 2003:OH and HO_2 concentrations, sources, and loss rates during the Southern Oxidants Study in Nashville, Tennessee, summer 1999. *Journal of Geophysical Research (Atmospheres)*, doi: 10.1029/2003JD003551

PRESENTATIONS

J.N. Bassis, H.A. Fricker, R. Coleman, J.B. Minster, 2005: New Insight into Ice Shelf Rift Propagation from Geodetic and Seismic Monitoring, *American Geophysical Union, Fall Meeting*, San Francisco.

J.N. Bassis, H.A. Fricker, J.B. Minster, 2004: The Role of Plastic Necking in Ice Shelf Rifting: A Comparison with Lithospheric Rifts, *American Geophysical Union, Fall Meeting*, San Francisco.

J.N. Bassis, H.A. Fricker, R. Coleman, J.B. Minster, 2003: An Investigation Into the Causes and Limiting Factors of an Active Rift on the Amery Ice Shelf: Fieldwork and Modeling Results, *American Geophysical Union, Fall Meeting*, San Francisco.

J.N. Bassis, A. Borsa, J.B. Minster, 2001: Estimating Surface Slope and Roughness over the Greenland Ice Sheet Through Deconvolution of Laser Altimeter Waveforms, *American Geophysical Union, Fall Meeting*, San Francisco.

ABSTRACT OF THE DISSERTATION

Dynamics of Ice Shelf Rift Propagation and Iceberg Calving Inferred From Geodetic and Seismic Observations

by

Jeremy N. Bassis
Doctor of Philosophy in Earth Sciences
University of California, San Diego, 2007
J.B. Minster, Chair
H.A. Fricker, Co-Chair

Iceberg calving accounts for two thirds of the mass discharged from the cryosphere to the ocean. Despite the prominent role that iceberg calving plays in the mass balance of ice sheets and glaciers, it remains one of the most poorly understood glaciological processes. Iceberg calving is preceded by the formation and propagation of fractures that sever the entire ice thickness. These fractures, known as rifts, can propagate for decades before an iceberg detaches. This dissertation presents results from three targeted field campaigns of geodetic and seismic measurements around the tip of a propagating rift on the Amery Ice Shelf, East Antarctica in 2002-03, 2004-05 and 2005-06. These observations are the first *in situ* measurements of rift propagation on an ice shelf.

Chapter 1 provides the motivation and background that inspired a detailed study of ice shelf rifting. Chapter 2 presents results from the first field season where it was shown that rift propagation is episodic. In Chapter 3 the detailed seismic network that was installed over the following two field seasons was exploited to accurately map the spatial and temporal trends in seismicity. In Chapter 4 data from automatic weather stations were used in combination with field measurements to show that neither winds, ocean currents nor tides trigger

rift propagation. In Chapter 5 we look at vertical deformation around the rift using data from both our global positioning system receivers and elevation profiles across the rift obtained from a satellite laser altimeter (ICESat). Using these two data sources, we show that the pattern of deformation along the rift walls is consistent with normal faulting. In Chapter 6 we derive an empirical non-dimensional stability parameter that predicts when unstable retreat of tidewater glaciers and ice shelves will occur. The stability parameter is validated using data from several Alaskan tidewater glaciers, two Greenland glaciers and three Antarctic ice shelves. Chapter 7 summarizes the work done and suggests directions for future research.

Chapter 1

Introduction

> A fact is a simple statement that everyone believes. It is innocent, unless found guilty. A hypothesis is a novel suggestion that no one wants to believe. It is guilty, until found effective.
>
> – Edward Teller

1.1 Objectives and Motivation

Ice is a metamorphic rock which, unlike most other rocks, has a melting point readily achievable near the surface of the Earth. It is for this reason that ice deforms so easily and that the ice sheets and glaciers have such a fascinating and dynamic range of behavior. It is also for this reason that observations of the deformation of ice provide much needed insight into the deformation processes that may (or may not) occur deep within the Earth. Of course, understanding the evolution of ice sheets and glaciers has also become an increasingly important (and occasionally controversial) focus of scientific inquiry as consensus has grown in the belief that anthropogenic warming is affecting the global climate. The focus of this dissertation is on iceberg calving, and it is the impact of the iceberg calving process on the cryosphere and climate system that is the primary motivation for this study.

Iceberg calving remains a poorly understood process despite the fact that calving is the primary process through which the cryosphere sheds mass to the ocean. Calving accounts for up to 2/3rds of the total loss while basal melting accounts for the remaining third (Jacobs et al., 1986; Van der Veen, 1999). The calving process is driven by the formation and propagation of large-scale rifts (fractures tens of kilometers long that penetrate the entire ice thickness of hundreds of meters). These rifts can propagate for decades before eventually becoming iceberg detachment boundaries (Lazzara et al., 1999; Joughin et al., 2004b). The tabular icebergs that detach in this manner are spectacularly large and can generate considerable media attention. For example, the three icebergs that calved from the Ross and Ronne ice shelves in 2000 contained approximately 40 000 km^3 of ice - several times the annual accumulation for the catchment area drained by the corresponding ice shelf sectors (Lazzara et al., 1999). Typically recurrence intervals for large bergs vary between ice shelves but tend to be of the order of several decades (Budd, 1966; Scambos et al., 2004). Although infrequent, when these events do occur they remove large amounts of ice very quickly. While large calving events are necessary to maintain the mass balance of the Antarctic ice sheet, the concern is that these events may become more frequent in response to atmospheric and oceanic warming. Small perturbations in calving frequency can translate into significant effects on the mass balance of the ice sheet. This concern has been increased by recent studies, which show that the ice sheet is losing more mass (by calving and basal melting) than it gains (by snowfall) (Rignot et al., 2002; Thomas et al., 2004; Velicogna and Wahr, 2006).

Relatively little is currently known about the processes and mechanisms involved in generating and propagating the rifts that precede iceberg detachment (Lazzara et al., 1999). This ignorance hinders attempts to predict realistically the effect of ocean and atmospheric warming on future ice shelf evolution under various climate change scenarios. Early studies in the 1970s provided a theoretical framework to explain the initiation and downward propagation of crevasses. Without any *in situ* measurements to test these theories, intellectual progress stalled over the next two decades. The advent of remote sensing in glaciology over the past 20 years rekindled interest in iceberg calving. This interest reached an apex in 2002 with the rapid disintegration of sections of the Larsen Ice Shelf. Unfortunately, the occasional “snap shots” that satellite imagery provide was not sufficient to resolve the short time scale dynamics that are fundamental to improving our understanding of fracture propagation processes. The work presented in this dissertation aims to remedy this deficiency using detailed *in situ* measurements around an actively propagating rift on the Amery Ice Shelf. Field measurements are used in combination with satellite imagery and theoretical models to determine the importance of different mechanical processes. The specific questions we seek to address are:

- *Is there a component of rift propagation that is seismic, or is it entirely aseismic?*
- *Is rift propagation quasi-continuous or episodic? If it is episodic, what determines the recurrence interval between events?*
- *What are the primary forces that drive propagation? Is rift propagation primarily driven by the internal stress of the ice or is it largely determined by short term environmental variables (e.g. wind stress, ocean swell, ocean tides)?*
- *How much variation is there in rift propagation rates on long (years to decades) and short (days to months) time scales?*

The specific questions are designed to advance our knowledge of the details of rift propagation. The long-term aim of this research is to *determine the sensitivity of iceberg calving rates to climatic change.* To do this we need to develop realistic models of ice fracture that can be used in conjunction with coupled ice shelf-ocean models. Currently, numerical models of ice shelves either do not incorporate calving at all, or treat iceberg calving using over simplified “calving laws”. A common calving law used for these studies is that icebergs detach when the ice thickness decreases below a critical value (Paterson, 1994; Grosfeld and Sandhäger, 2004). Without fracture physics within these models, any quantitative prediction of the response of the ice sheets to climate change is seriously compromised.

1.2 Ice Sheets and Climate Change

Ice sheets contain 60% of the world's fresh water (Hook, 2005), for this reason arid countries have often looked wistfully to polar regions and there has been no lack of fanciful proposals to transport ice from Antarctica to water poor regions. Furthermore, it has been hypothesized that a massive influx of cold dense fresh water from the ice sheet could disrupt the pattern of thermohaline circulation of the ocean with severe global scale climatic and ecological implications.

In addition to storing much of the Earth's fresh water, ice sheets also play a prominent role in sea level rise. At present rates, we would only expect a 20 cm rise in sea level over the next hundred years. However, the Antarctic ice sheet contains enough water to raise sea level by a total of 57 m (Hook, 2005) and the estimating the contribution of ice sheets to sea level rise remain one of the largest uncertainties in sea level rise projections. Present sea level rise is approximately 2 mm per annum. While the largest part of this signal presently comes from thermal expansion of the ocean, the cryospheric contribution is about a third of the total (0.7 mm per annum). Most of this is accounted for by melting alpine glaciers (Arendt et al., 2002). At present rates we would only expect a 20 cm rise in sea level over the next hundred years. An increase in melt rates or iceberg discharge from the ice sheets could significantly increase sea level projections by an order of magnitude. Despite the concern this scenarios raises, our current knowledge of ice sheet dynamics and interaction with other components in the climate system is insufficient to gauge the effect that long term climatic changes will have an ice discharge. Improving this deficiency in our knowledge remains a serious scientific challenge to the current generation of glaciologists, geophysicists and climate scientists.

One of the observations with the most far reaching consequences is that

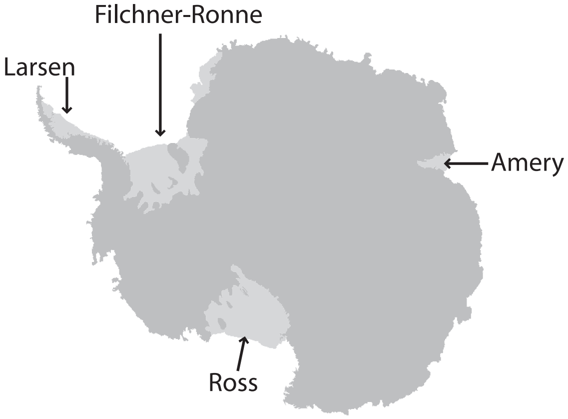

Figure 1.1: Sketch map of Antarctica showing the locations of the major ice shelves..

90% of the ice from Antarctica is drained through small fast flowing ice streams and fast flowing tributary glaciers (Paterson, 1994; Bamber et al., 2000). These ice streams are far more dynamic than previously thought and appear to be exhibit substantial century time scale variability caused by thermomechanical instabilities and interaction with the soil near the base of the ice. The potential for rapid flow means that the time scale of ice sheet collapse may be an order of magnitude less than previously thought. While still controversial, one of the pathways through which this could occur is the removal of the ice shelves that are believed to "buttress" flow from the interior of Antarctic Ice Sheet (Oppenheimer, 1998).

1.3 Ice Shelves and Iceberg Calving

1.3.1 Ice Sheets and their stability

Antarctica is surrounded by floating platforms of ice, hundreds of meters thick, called ice shelves. The largest embayed ice shelves that surround Antarctica (Ross, Filchner-Ronne and the Amery - see Figure 1.1) are responsible for redistributing most of the mass from the ice sheet to the Southern Ocean, either through iceberg calving (∼75%) or basal melt (∼25%) (Jacobs et al., 1992). Because ice shelves are in direct contact with both the atmosphere and ocean, it is likely that

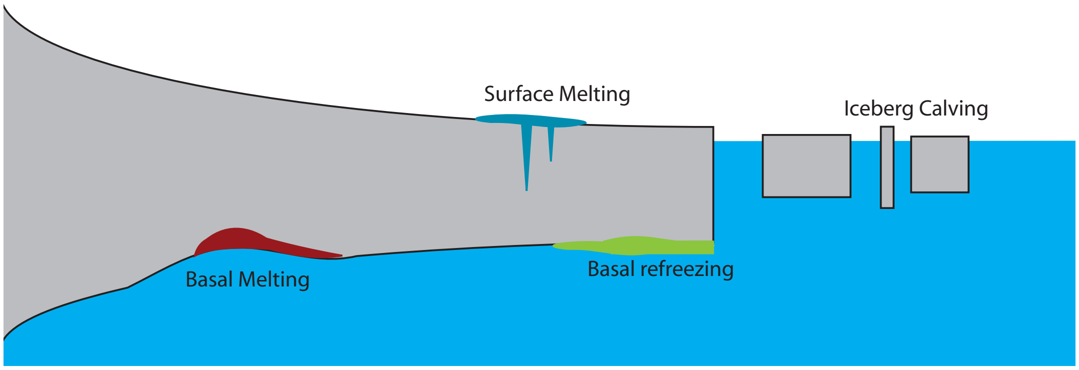

Figure 1.2: Mechanisms of mass loss from ice shelves.

they are also sensitive indicators of climate change (Mercer, 1978). However, we do not yet know how ice shelves will change in response to increased atmospheric or oceanic temperatures. For example, the recent melt-water-related catastrophic breakup of sections of the Larsen Ice Shelf (LIS) has demonstrated that strong atmospheric warming can lead to very rapid change by enabling intense hydrologic fracturing of the ice. Alternatively, a warming ocean can gradually erode an ice shelf by increasing basal melt causing a slow decrease in thickness over time (Rignot et al., 2002; Shepherd et al., 2001). While these changes will not directly affect sea level rise (ice shelves are freely floating), they do directly contribute to the fresh water budget of the Southern Ocean (e.g. Jacobs et al., 1992) and, because of their potential influence on flow from the grounded ice sheet (so called "buttressing"), may also have an indirect influence on sea level. Monitoring ice shelves is therefore an important component in understanding the ice sheet system. Most ice shelves form within embayments where resistive back-stresses from the walls and other "pinning" points (e.g. bottom protrusions that cause isolated grounding points) limit the rate at which these shelves can spread. This indicates that a freely spreading ice shelf is not stable.

1.3.2 Iceberg Calving

Icebergs detach when one or several fractures near the ice terminus isolate an iceberg. For ice shelves, large fractures that penetrate the entire ice shelf thickness (termed "rifts"), tend to originate along sharp pointed segments of the ice margin, pinning points or suture zones between ice streams (Lazzara et al., 1999; Fricker et al., 2002). Occasionally, rifts formed near the grounding zone advect for centuries and then reactivate as they approach the ice shelf front. Iceberg calving occurs as part of a cycle where the front advances (by ice flow) beyond it's embayment walls and then retreats (by iceberg calving). These quasi-periodic cycles of advance and retreat result in the sporadic production of immense tabular icebergs with typical recurrence intervals of many decades. For example, the three icebergs that calved from the Ross and Ronne ice shelves in the year 2000 contained approximately 4000 km^3 of ice - several times the annual accumulation for the catchment area drained by the corresponding ice shelf sectors (Lazzara et al., 1999). In addition, the ice front continually sheds small bergs but the cumulative volume of these is minuscule compared with that of the less frequent icebergs. While production of these large bergs is part of the expected behavior of ice shelves, the retreat and subsequent disintegration of fringing ice shelves of the northern Antarctic Peninsula is not (Scambos et al., 2003). These disintegrations appear to be rare events that are related to regional climate warming of ~2.5°C over the past 50 year (Vaughan and Doake, 1996). Evidence shows that the Larsen Ice Shelf had been stable for the past 9000 years (Domack et al., 2004) suggesting that the disintegration of ice shelves is a very different mode of calving distinct from the usual pattern of sporadic discharge of large tabular bergs. There is some evidence of seasonal rift propagation on ice shelves (Fricker et al., 2005b), that has been speculated to be caused by melt water, but there is little evidence for a seasonal variation in calving rates for the large ice shelves of Antarctica (Lazzara et al., 1999; Jacobs et al., 1986; Fricker et al., 2002).

1.3.3 Rift Propagation

Relatively little is currently known about the processes and mechanisms involved in generating and propagating the large rifts that precede their detachment from ice shelves. This ignorance hinders attempts to realistically predict the effect of ocean and atmospheric warming on future ice shelf evolution under various climate change scenarios. Fracture is a complicated process that occurs over a large range of temporal and spatial scales. Relevant spatial scales are:

- *microscopic scale* ($\sim 10^{-9}$ m to 10^{0} m) associated with atomic forces between atoms and molecules and grain scale processes that are directly responsible for nucleation of fracture

- *mesoscopic scale* ($\sim 10^{-1}$ m to 10^{2} m) of crevasses, crevasse networks and fracture networks that form ahead of the tips of propagating rifts

- *rift scale* ($\sim 10^{2}$ m to 10^{5} m) associated with the propagation of through cutting fractures that sever the entire ice shelf depth. These fractures are the largest in the glaciological world and can extend over 100s of kilometers.

- *ice shelf scale* ($\sim 10^{4}$ m to 10^{6} m) of large scale flow of the ice shelf. If coherent fracture networks span the entire ice shelf, disintegration occurs

Each of these length scales has an associated time-scale as well. For example, large-scale rift propagation occurs over decades while small defects in the ice can lead to localized ruptures that last less than a second. Most laboratory scale experiments probe phenomena with length scales ranging between microscopic and mesoscopic, while the most geophysically significant fractures are much longer in length. This introduces a disconnect between the processes and mechanisms studied in laboratory experiments with those studied in field experiments. Whether the laboratory experiments can be extrapolated several orders of magnitude to larger length scales is currently not known.

1.4 Previous Studies

Early theoretical studies focused on the bending stresses caused by the imbalance between glaciostatic pressure and hydrostatic pressure at the glacier front (Reeh, 1968; Fastook and Schmidt, 1983; Hughes, 1992). At the front, the imbalance between the glaciostatic weight of the ice and the hydrostatic pressure of the water, results in a net outwardly directed tensile stress. This type of mechanism results in a stress maximum at about one ice thickness from the ice front (Reeh, 1968), suggesting that icebergs should also have the characteristic size of one ice thickness. While this may be true for tidewater glaciers, it is not clear how this type of mechanism can generate the large tabular icebergs that calve from the Antarctic ice shelves that have widths of tens of kilometers or more.

A different approach to ice shelf fracture has been to attempt to treat the fracture process using linear elastic fracture mechanics (LEFM). In this approach ice is modeled as a brittle solid and fracture is assumed to occur if the stress concentrated at the tip reaches a critical value (e.g. Lawn,1993). This approach dates back several decades to the pioneering work of Weertman (1974) and Nemat-Nasser et al. (1979), both of whom used dislocation-based fracture mechanics to study the penetration depth of crevasses. Increasingly sophisticated analytic, numerical, and experimental techniques have since been applied to the study of crevasses to include more complicated effects, such as water pressure within crevasses, interaction of multiple crevasses and even thermodynamic processes such as freezing of water within ice fractures (Fastook and Schmidt, 1983; Vaughan, 1993; Van der Veen, 1998; Rist et al., 2002; Alley et al., 2005). Most of these studies concentrated on vertical propagation of crevasses. None of these studies were able to test any of their ideas against actual field data. This may be because working in heavily crevassed or rifted areas is often quite dangerous and mounting field campaigns is expensive logistically.

Satellite images have provided the first glimpse of the rift propagation process from a safer vantage point. Lazzara et al. (1999) used AVHRR, and NOAA infrared and SAR imagery to monitor the calving of the three large bergs that calved from the Ross Ice Shelf in 2000. In a series of papers, MacAyeal et al. (1998), Rignot and MacAyeal (1998) and Hulbe and MacAyeal (1999) used interferometry and ice shelf modeling to try to infer the mechanical role of mélange (a mixture of snow and ice types that infills the rifts) in rift propagation. Larour et al. (2004b) extended these studies by combining interferometery with LEFM modeling to study horizontal rift propagation rates of a rift system on the Ronne Ice Shelf. They concluded that mélange was an important component gluing the rift walls together. Joughin et al. (2004b) used satellite radar data to study the widening of a system of rifts on the Ross Ice Shelf in the stage immediately before calving. Fricker et al. (2002) used a combination of imagery dating back to the CORONA mission (1962) to monitor the evolution of a rift system on the Amery Ice Shelf. Fricker et al. (2005b) used MISR images to measure propagation rates of two rifts on the Amery Ice Shelf. They found a seasonal pattern in rift propagation rates, where rifts lengthened faster in the summer than in the winter. However, the temporal resolution of satellite imagery is not adequate to resolve all of the spatial and temporal scales involved in fracture. For example,

All of these studies assumed that the internal glaciological stress within the ice controlled initiation and propagation of rifts. In contrast, Holdsworth and Glynn (1981) suggested that flexural waves excited by coupling with ocean swell might be responsible for detachment of large tabular icebergs. There was no observational evidence to support this theory but in light of recent measurement on the Ross Ice Shelf, MacAyeal et al. (2006) has resurrected this theory. They have suggested that large storms generated in the North Atlantic can propagate across entire ocean basins and trigger ice shelf fracturing. They hypothesized that these swell events may be instrumental in causing the breakup of icebergs and possibly in triggering propagation of rifts. This hypothesis is particularly intriguing because of the potential for providing a method for synchronous increased discharge of icebergs, one of the mysteries of Heinrich events (e.g. Clarke et al.,1999). If storms can trigger iceberg calving, then roughening of the North Atlantic may have been a factor in the generation of an armada of icebergs believed to have been produced by the Laurentide ice sheet (Heinrich, 1988; Bond and Lotti, 1995; MacAyeal, 1993).

These observations indicate that iceberg calving is a key process that enables rapid change in the cryosphere. It is not known how prolonged atmospheric and ocean warming will affect calving rates. Increased atmospheric and oceanic temperatures may lead to an increase in the number or size of calving events. Although, with the exception of melt-water triggered disintegration of sections of the Larsen Ice Shelf, (Scambos et al., 2003), this connection has not yet been established. A more controversial theory is that iceberg calving could actually be a catalyst for climate change (Hughes, 1986; Meier and Post, 1987; Van der Veen, 1996). For example, Hughes (1986) suggests that small perturbations related to calving can amplify by leading to a reduction in back-stress near the calving front that then triggers increased velocities and greater thinning rates of the ice.

To study rifting on the appropriate time-scales it is necessary to combine satellite observations with near-continuous field observations around the tips of propagating rifts. This is particularly important because we currently do not even have an understanding of what forces drive rift propagation. The only way progress in understanding iceberg calving can be made is by systematic measurements from which the varying hypotheses can be tested.

1.5 Ice Rheology

Over short time scales (seconds) ice deforms like an elastic solid, while over long time scales (years) ice behaves like a viscous fluid. This dichotomy is largely irrelevant for most glaciological purposes because the time scales considered by glaciologists are so long that elastic deformation of the ice is largely negligible. Yet, fracture of ice contains a spectrum of time scales, varying from the very fast time scale of individual rupture events that might last for for less than one second to the much slower rate of long term rift propagation that can occur over decades. The distinction between elastic and viscous behavior is crucial because most of the framework of fracture mechanics is only applicable to how elastic materials fail.

The rheology of ice consists of a spectrum of constitutive relations that vary depending on the load and loading rate as well as thermodynamic conditions. Laboratory experiments on ice as well as seismic measurements indicate that ice behaves like an elastic solid over short periods with Young's Modulus (E) ranging between 1-10 GPa (Hobbs, 1974). Less well known is the viscous rheology of ice. Overwhelmingly, the most common form for the flow law of ice is a power law first postulated by Glen (1952) and generalized by Nye (1957):

$$\dot{\epsilon_{ij}} = A\tau^{n-1}s_{ij} \quad ; \quad s_{ij} = \sigma_{ij} - P\delta_{ij} \tag{1.1}$$

τ is the second invariant of the stress tensor, n is the flow-law exponent, A is the rate constant, s_{ij} is the stress deviator and P is the pressure. The second invariant is given by:

$$2\tau^2 = s_{11}^2 + s_{22}^2 + s_{33}^2 + 2(s_{12} + s_{13} + s_{23})^2 \tag{1.2}$$

When applied to ice, equation 1.1 is called "Nye's Generalization of Glen's flow law". This type of rheology was first introduced at least as early as 1929 (Norton, 1929) and had been widely used in metallurgy decades prior to Glen's work on ice. For semantic and multi-disciplinary clarity in this dissertation we refer to this type of constitutive relation as "power-law creep".

It is common in the literature to choose $n = 3$ as the flow law exponent although Glen (1952) concluded that $n = 3.5$ was most appropriate for stresses of the order of a few hundred kPa. At very low stress Hutter (1983) argued, based on physical reasons, that a Newtonian, $n = 1$ rheology must apply. At much higher stresses where recrystallization of ice occurs the power law is also believed to hold; n may be much higher with typical values of the order of $n = 10$ (Hutter, 1983). It is usually more convenient to use the inverse of equation 1.1 and express the stress deviator in terms of the strain rate, $\dot{\epsilon_{ij}}$:

$$s_{ij} = \frac{1}{A\tau^{n-1}}\dot{\epsilon_{ij}} \tag{1.3}$$

Using equation 1.3 an "effective" stress dependent viscosity can be defined:

$$\eta_{eff} = \frac{1}{A\tau^{n-1}} \tag{1.4}$$

Alternatively, by using the relationship between the second strain rate invariant $\dot{\gamma}$ and the second stress invariant τ:

$$\tau = A^{1/n}\dot{\gamma}^{1/n} = B\dot{\gamma}^{1/n} \tag{1.5}$$

We can also express the stress in terms of the strain rate:

$$s_{ij} = B\dot{\gamma}^{\frac{1}{n-1}}\dot{\epsilon_{ij}} \tag{1.6}$$

Again, the term $B\dot{\gamma}^{\frac{1}{n-1}}$ represent an effective (strain rate dependent) viscosity:

$$\eta_{eff} = B\dot{\gamma}^{\frac{1}{n-1}} \tag{1.7}$$

Despite the ubiquitous use of Glen's flow law in glaciology a variety of other theoretical and empirical functions can also be used to describe the rheology of ice. Hutter (1983) considered a variety of alternative parametrization and showed that a wide variety of them can fit the measurements at least as well, and often better than the commonly used cubic flow law. More recently, Goldsby and Kohlstedt (2001) proposed a grain-size dependence to flow, often termed "superplastic". This list is by no means an exhaustive list of all of the rheologies ascribed to ice under different conditions. Given the wide variety of flow laws used and proposed in the literature, results that are sensitive to the particular parametrization of rheology should be viewed with caution.

1.6 Overview

The primary goal of this dissertation is to improve our knowledge of the driving forces and mechanisms that lead to the calving of large tabular icebergs from Antarctic ice shelves. While the literature on crevasse initiation using linear elastic fracture mechanics (LEFM) has grown substantially over the past three decades there are still very few studies that involve actual observations of initiation and propagation of crevasses or rifts in the field. This paucity of data - partly due to the great dangers involved in making measurements in these environments - has stalled the development of more realistic theories of ice fracturing. The measurements presented in this dissertation constitute the first attempt at dedicated *in situ* measurements of ice shelf rift propagation. A preview of what is to come is briefly summarized below.

Chapter 2: In the first chapter we describe the location of our study sites and introduce the methodology and instrumentation used to study rifting. We present results from a pilot study during which we deployed global positioning system receivers in combination with seismometers around the tip of an actively propagating rift on the Amery Ice Shelf. This chapter is already published (Bassis et al., 2005).

Chapter 3: Chapter 3 describes two follow-up studies during the Austral summers of 2004-05 and 2005-06. We investigate the spatial pattern of seismicity and compare the distribution of seismic event magnitudes with common patterns found for earthquakes. We also compare the field measurements with satellite derived rift lengths and discuss causes for changes in propagation rates between field seasons. This time, we are able to compare results from three field seasons.

Chapter 4: In Chapter 4 we use the results obtained in Chapter 3 to examine the role of environmental variables on rift propagation. We compare the timing of the episodic bursts of propagation with tidal amplitudes and wind speeds from nearby automatic weather stations. We also compare the timing of rupture events with the arrival of the tsunami generated by the December 26th Sumatra earthquake.

Chapter 5: In contrast to the previous three chapters that focused primarily on horizontal deformation associated with rift propagation, in Chapter 5 we look at vertical deformation near the rift walls determined from our GPS and present both elastic and viscous flexure models that indicate that the rift walls are asymmetric.

Chapter 6: In Chapter 6 we take a different approach to the problem and consider a "mean field" approach to the stability of ice shelves and tidewater glaciers. We use dimensional analysis in conjunction with data from several stable and retreating ice shelves and glaciers to derive an empirical stability parameter. The primary focus of this chapter is to try a more direct approach to understanding the potential sensitivity of iceberg calving on climate change.

Chapter 7: In Chapter we take a look at the bigger picture and summarize results from the previous 6 chapters. We also discuss future directions necessary to continue advancing our knowledge of iceberg calving.

Chapter 2

Episodic Rift Propagation

> A scientific truth does not triumph by convincing its opponents and making them see the light, but rather because its opponents eventually die and a new generation grows up that is familiar with it.
>
> – Max Planck

Abstract

We investigate ice shelf rift propagation using a combination of GPS and seismic measurements near the tip of an active rift. These measurements reveal that propagation occurs in episodic bursts, which were identified based on swarms of seismicity accompanied by rapid rift widening. The bursts last approximately 4 hours and are separated by 10-24 days. In between bursts, the rift widens at a rate comparable to that of ice shelf spreading. Comparison of automatic weather station data and tidal amplitudes show that the propagation bursts are not directly triggered by winds or tides, suggesting that rift propagation is driven by the background glaciological stress in the ice shelf. We show that the ice debris that partly fills the rift may play a role in controlling the rate of propagation.

2.1 Introduction

Iceberg calving from ice shelves is a key process in determining the amount of mass lost from the Antarctic ice sheet, accounting for up to two thirds of the total loss (Jacobs et al., 1992). Because the ice shelves are in direct contact with both atmosphere and ocean, it is likely that they are sensitive indicators of climate change and may experience enhanced melting (surface and basal) and increased calving rates in a warming climate (Mercer, 1978; Hughes, 1983). The recent melt-water-related catastrophic collapse of sections of the Larsen Ice Shelf (LIS) (Scambos et al., 2003) has emphasized the need to improve our understanding of calving processes. Furthermore, the subsequent acceleration of tributary glaciers of the Antarctic Peninsula in the months and years after sections of the LIS collapsed (De Angelis and Svarkca, 2003; Scambos et al., 2004) has confirmed that ice shelves do influence ice sheets.

Satellite imagery has recently provided the first glimpse of the processes which lead to the calving of large tabular icebergs from ice shelves (Lazzara et al., 1999; Joughin et al., 2004b; Fricker et al., 2005b). The first stage of this calving process is the initiation of "rifts", which we use to describe fractures that penetrate the entire ice shelf thickness, as opposed to "crevasses" which are not through-cutting. Once initiated, rifts then propagate, sometimes for decades, until multiple rifts isolate an iceberg which then detaches.

Historical records show that large tabular bergs are produced sporadically with typical recurrence times of 50-100 years (Budd, 1966) and despite their large size, appear to have little effect on the long-term ice flow. Unlike the disintegration of parts of the peninsular ice shelves, the production of tabular bergs is part of a normal cycle in which the ice shelf advances beyond its confining embayment or pinning points and subsequently retreats by calving. However, the lessons we have learned from the Antarctic Peninsula suggest that the calving process may also be sensitive to climate change (Scambos et al., 2003). Since iceberg calving can rapidly remove large amounts of ice, this process may be important in determining the future stability of the ice sheet. Despite this prominent role we know very little about the mechanisms and controlling forces that lead to rift initiation and propagation. This ignorance hinders any attempt to assess accurately how ice sheets will respond to future climate change. Here we describe the results of a field experiment specifically designed to improve our understanding of rift propagation.

2.2 Location of Survey and Description

Our field site was located near the front of the AIS. The last major calving event from the AIS occurred in late 1963 or early 1964 when a iceberg ∼10 000 km^2 was reported to have detached (Budd, 1966). The AIS is predicted to reach its pre-calving 1963 position in the mid 2020's (Fricker et al., 2002). The Amery is therefore poised for another major calving event within the next 20 years.

In the meantime, an intermediate-sized iceberg (30 km by 30 km) - colloquially known as the "Loose Tooth" - is expected to detach around 2006 [In retrospect, we now know that this is a premature estimate. Our current projections suggest that the Loose Tooth will detach within the next 5-10 years]. The associated active rift system (Figure 2.1) consists of two longitudinal-to-flow rifts ∼30 km apart that initiated about 20 years ago (L1 and L2) and two transverse-to-flow rifts (T1 to the west and T2 to the east) that initiated at the tip of L1, forming a triple junction that was first observed in 1995. Both rifts T2 and T1 occur in the transition zone where transverse-to-flow strain rates begin to exceed longitudinal-to-flow strain rates (Young and Hyland, 2002). T2 currently propagates at about 4 m/day (Fricker et al., 2005b). When it connects with L2, an iceberg 900 km^2 containing over 300 GT of ice will calve. Analysis of historical ice-front data suggests that a similar Loose-Tooth sized event preceded the last major calving event of 1963-64 (Fricker et al., 2002).

Our survey was focused on the tip of T2 during the 2002-2003 austral summer. In this region, ice shelf flow is approximately 3 m/day (1.1 km/year) in a northeasterly direction, and the ice shelf is ∼400 m thick. We deployed 6 dual

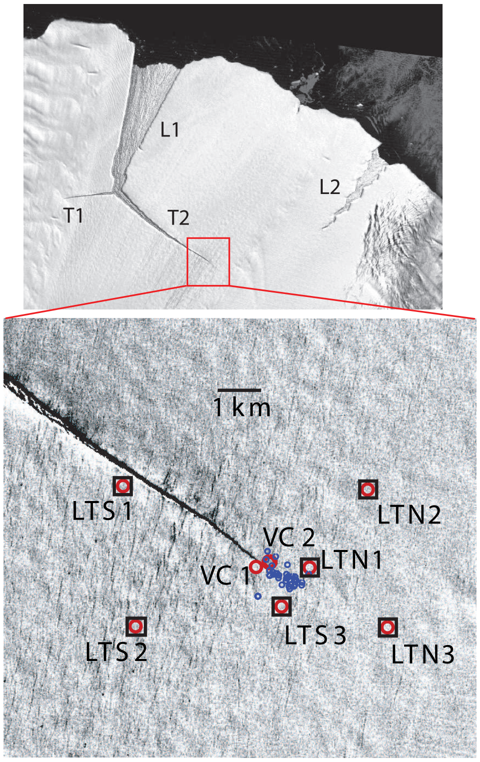

Figure 2.1: (a) LANDSAT 7 ETM image of the Loose Tooth rift system acquired on Mar. 2, 2003. (b) Location of instruments around the tip of rift T2 overlaid on LANDSAT 7 image (acquired on Nov. 7, 2002). Seismometers are plotted as circles, GPS are squares. Epicenters of seismic events are shown as blue dots.

frequency GPS receivers operating at 30 s (0.033 Hz) and 8 vertical component L-4C seismometers recording at 0.1 s (10 Hz) around the rift tip (Figure 2.1) for 46 days starting on December 8, 2002. Two additional seismic stations (VC1 and VC2) were deployed on either side of the rift, within 10 m of the edge. Of the GPS baselines, LTS3-LTN1 had the greatest sensitivity to rift opening since it was the shortest baseline ($\sim$ 1km), and because the rift tip propagated between these two stations during the observation period.

In the field we noted that T2 propagates through a field of normal-to-rift crevasses typically spaced several hundred meters apart. During the initial instrument deployment we only observed a few of these crevasses, since snow bridges covered them. At the end of the survey period, snow bridges had sagged considerably, revealing a widespread array of crevasses extending far ahead of the rift tip. All of the rifts (L1, T1 and T2) are filled with a mixture of ice blocks and snow that had fallen in from the sides. This debris which partially fills the rift is often called mélange.

2.3 Data Processing and Results

All GPS receivers recorded continuously over the 46 day period of the survey (December 8, 2002 through January 26, 2003), except LTN3 which suffered daily power gaps of up to 12 hours due to solar panel regulator problems. Three seismic stations were omitted from the analysis: two which failed to record data (LTN2 and LTN3) and another (LTS2) which was inadvertently deployed on top of a crevasse.

2.3.1 GPS

All GPS data were processed as kinematic sessions relative to LTS3 using the RTD software package (Bock et al., 2000). This approach has the advantage that the positions can be solved for at each epoch (i.e. every 30 s), generating a times series of positions for each station relative to LTS3. Furthermore, any common motion due to ice flow and tides experienced at each site. After processing, all outliers outside 3.5 times the interquartile range (∼5 cm) were discarded. The censored time series was then smoothed using a 2-hour median filter. Experiments showed that smoothing with narrower windows did not reveal any recognizable short period signal.

All baseline lengths exhibit an average linear trend in length consistent with large-scale ice shelf spreading, with transverse-to-flow strain rates slightly larger than longitudinal-to-flow strain rates. There are no detectable systematic differences between rates of extension of baselines that span the rift and those that do not. The shortest baseline, LTS3-LTN1, which spans the rift tip, has three jumps in baseline length on days 1, 12 and 37 of the survey (Figure 2.2 (a)). All three jumps occur over a 4 hour period with magnitudes of approximately 1 cm, normal to the rift. After each jump, the rate of extension of the normal-to-rift baseline increases. The component parallel to the rift axis does not exhibit any jumps, but does show a small acceleration over the 46 days of the deployment. We did not see corresponding jumps in the lengths of any other baselines, which are all considerably longer and therefore have larger associated noise levels than the 1 cm signal seen for baseline LTS3-LTN1.

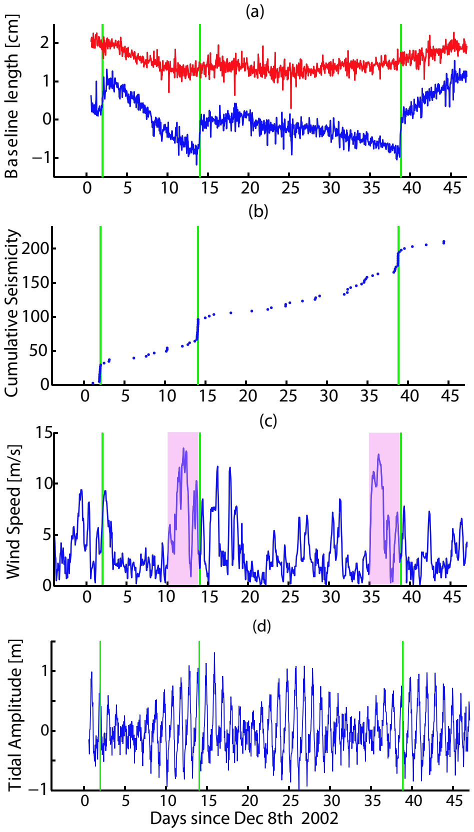

Figure 2.2: (a) Detrended time series of baseline lengths. Normal-to-rift component is the blue line. Parallel-to-rift component is vertically offset and shown in red. (b) Cumulative seismicity at LTN1. (c) Wind speeds from AWS. Two of the three bursts of propagation were preceded by periods of high winds (shaded region). (d) One hour tidal amplitudes for LTS3 obtained by processing the GPS data relative to fixed rock sites. Green line shows times of the three bursts of propagation.

2.3.2 Seismicity

During the 46 days of the survey we identified 305 seismic events that were recorded at three or more stations. Although all arrivals showed high signal-to-noise ratios, they had corner frequencies higher than 5 Hz. Seismograms were thus under-sampled and distorted by the anti-aliasing filter, precluding waveform analysis for source studies. In this study, we are only interested in rift tip events. We therefore culled the data set by discarding long duration and poorly sampled events, and keeping only those with earlier arrivals and larger amplitudes at stations near the tip, reducing the dataset by 60%. We used a grid search with constant P-wave velocity across the ice shelf to locate all events where we could identify a first arrival at four stations (locations shown in Figure 2.1). Although there is considerable scatter, the locations cluster around the rift tip. We tested the robustness of this distribution by using P-wave velocities ranging from 1500 m/s (porous firn) to 3500 m/s (cold ice). This changed the scatter, however the center of the distribution remained about the same.

The cumulative seismicity is shown in Figure 2.2 (b). Background seismicity of around 2-3 events per day is punctuated by swarms of 12-14 events over 4 hours that occur on days 1, 12 and 37. The timing of these swarms coincides with the jumps in GPS baseline length (Figure 2.2 (a)).

2.4 Discussion

There are several possible sources for the seismic signals shown in Figure 2.2 (b), including; rupture associated with propagation of the rift; snow bridge collapse; ice-front calving events; and propagation of normal-to-rift crevasses. While we cannot completely rule out these other sources, we think that most of the seismicity is due to rift propagation. Waveforms generated by snow-bridge collapse would have longer durations and lower frequency content. Ice-front calving events and propagation of crevasses are also unlikely sources, since these events would not cluster around the rift tip nor would they cause the rift to widen. The coincidence of seismic swarms with rapid rift widening reinforces our belief that the sources are bursts of rift propagation.

One plausible interpretation of our observations is that each seismic event recorded during the propagation bursts represents an individual tip rupture event and the rift propagates forward via a sequence of these small events. This is reminiscent of the quasi-stable stick-slip behavior described in ice fracture experiments (Rist et al., 2002). Alternatively, it may be evidence of a mechanisms where the rift propagates by the coalescence of micro-cracks ahead of the main crack tip as observed in some fracture experiments (Schulson, 2001). This idea is supported qualitatively by the fact that these bursts occur within a finite time interval, instead of a single propagation event. Macroscopically, we can relate the sequence of individual rupture events to a pseudo-continuous propagation rate. Based on satellite image analysis, we estimate that the rift propagated 200 m over 46 days (Fricker et al., 2005b). If we assume that propagation occurred exclusively during the three bursts, then the average propagation speed during each burst is less than 1 cm/s, five orders of magnitude slower than the expected velocity of critical crack propagation (i.e. body wave speeds) (Lawn, 1993).

We initially thought that the episodic bursts of propagation might be caused by external stresses (e.g. tides, ocean swell, storms). A comparison of wind speeds from the closest automatic weather station (Figure 2.2 (c)) and tidal amplitudes (determined from our GPS by processing relative to a fixed rock site LDBF); Figure 2.2 (d)) shows that the bursts do not coincide with periods of higher than average winds or tides. This suggests that there is no instantaneous cause and effect relationship between these environmental forcings and propagation. However, two of the three bursts did occur within three days of periods of sustained winds (shaded part of Figure 2.2 (c)), suggesting there might be some relationship with prolonged winds. If this were the case, we would expect the rift would propagate faster in the winter when the winds are strongest, contrary to the multi-year observations of Fricker et al. (2005b). Our observations do not support the hypothesis that instantaneous environmental stresses are the sole drivers of rift propagation. However, we cannot gauge the effect of longer term environmental stresses that did not vary significantly over our observation period (e.g. due to variations in sub-ice shelf ocean currents, mélange thickness). These factors may modulate the background glaciological stress. As the Loose Tooth becomes progressively decoupled from the ice shelf, environmental stresses may have a greater influence on rifting.

Another possible contributor to rift propagation is the internal stress of the ice. The experiments of Rist et al. (2002) demonstrated that the initiation of crevasses in response to the internal stress of the ice shelf can be described using linear elastic fracture mechanics (LEFM). Larour et al. (2004a) applied the geometry of a double cantilevered beam to model rift propagation on the Ronne Ice Shelf, and treated the fracture process using LEFM. This loading configuration has the advantage that it results in stable rift growth. However, because the driving force is gravity, we believe it is more appropriate to treat the system as load-controlled, i.e. the gravitationally induced stresses are independent of rift length. If this is true, what forces resist propagation to maintain stable rift growth? We believe that the answer to this question comes from considering how the mélange inside the rift modifies the stress field. The stress opening the rift, ΔP, has a glaciological component (σ_{glac}), a hydrostatic component (S_h) and a viscous component (P_v):

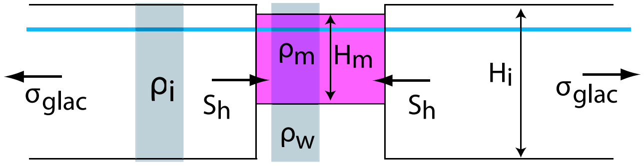

Figure 2.3: Cartoon illustrating the horizontal forces acting on the rift walls. S_h is the difference between the depth averaged pressure through a column of ice shelf and through the rift (shaded regions).

$$\Delta P = \sigma_{glac} - S_h - P_v \tag{2.1}$$

S_h can be found using a simple force balance between the depth averaged pressure within the rift and that of the surrounding ice shelf (illustrated in Figure 2.3):

$$S_h = \rho_i g \frac{H_i}{2} \times \left\{ 1 - \frac{\rho_m}{\rho_i} \left(\frac{H_m}{H_i} \right)^2 - \frac{\rho_i}{\rho_w} \left[1 - \left(\frac{\rho_m}{\rho_i} \right)^2 \left(\frac{H_m}{H_i} \right)^2 \right] \right\} \tag{2.2}$$

where ρ_i, ρ_w, ρ_m are the depth averaged densities of ice, water and mélange respectively and H_i, H_m are the thicknesses of the shelf ice and mélange. The viscous pressure drop, P_v is caused by movement of the mélange within the rift. It is clear from equations (2.1) and equation (2.2) that a decrease in mélange thickness will result in a decrease in ΔP. With no mélange (i.e. $H_m = 0$) S_h is largest and ΔP is smallest. Rapid propagation of the rift will result in the formation of a tip cavity which will be free of mélange (although it will quickly fill with sea water) resulting in a decrease in ΔP. This decrease in driving stress will stabilize, or possibly even arrest, further propagation. This implies that the average rate of propagation is limited by how quickly new mélange is formed. Accumulation of new mélange by wind-blown snow and marine ice formation will be too slow to affect propagation on the weekly time scales considered. However, following a propagation burst, it is likely that sea water in the tip cavity will rapidly begin to freeze onto the cold rift walls and blocks of ice from the rift walls will slump into the rift, wedging it open. Both of these processes will result in a rapid accumulation of mélange near the tip which will again increase the driving stress. This suggests that the episodic propagation that we observe may be caused by a cycle during which slumping of ice blocks into the rift combined with freezing of water onto the walls ratchet the rift open in a series of discrete bursts.

2.5 Conclusions

We have shown that over the 46-day observation period, rift propagation occurs episodically in bursts of growth of 4 hours duration, with recurrence intervals of 10 and 24 days. The average propagation rate during each burst is very low suggesting that rift propagation is predominantly subcritical. In between bursts, the rift widens at a rate comparable to that of normal ice shelf flow, indicating that the budding iceberg is still tightly coupled with the ice shelf. The bursts of propagation that we have observed are not directly triggered by either tides or winds, suggesting that the primary driving force is the background glaciological stress of the ice shelf. This driving force may be reduced after a propagation burst by the formation of a tip cavity, which can stabilize propagation. We speculate that following each propagation burst, slumping of ice blocks into the rift and freezing of water onto the walls may wedge the rift open again in a series of episodic propagation events. Future field seasons will provide further insight into the importance of these processes.

This chapter, in full, has been published in Geophysical Research Letters, J.N. Bassis, H.A. Fricker, R. Coleman, J.B. Minster. Episodic propagation of a rift on the Amery Ice Shelf, East Antarctica. The dissertation author was the primary investigator and author of this paper.

Chapter 3

Seismicity and Deformation Associated with Rift Propagation

> An expert is a man who has made all the mistakes which can be made in a very narrow field.
>
> – Neils Bohr

Abstract

In this chapter the results presented in the previous chapter are extended using data from two additional field seasons. The subsequent measurements, made during the Austral summers of 2004-05 and 2005-06, enabled us to see how both the rift-induced seismicity and strain rates vary over a three year period. The additional data confirm our earlier findings that rift propagation is episodic, occurring in bursts of several hours with typical recurrence times of several weeks (Chapter 2). The propagation events that we detected were inferred from rapid rift widening measured by our GPS, concurrent with swarms of seismicity detected with our seismometers. We also found that both the number of swarms and the number of events within each swarm decreased slightly during the final field season (2005-06). The timing of the slowdown corresponds with the rift tip propagating into a suture zone where two ice streams merged hundreds of kilometers upstream. This leads

us to speculate that defects within the ice in the suture zone lead to a reduction in stress concentration ahead of the rift tip. In addition to looking at temporal trends in seismicity, we examined the distribution of hypocenter locations. We found that seismic events cluster around the rift tip but extend several kilometers up-rift (towards the triple-junction) from the visible rift tip. Using a rough magnitude scale we show that the size-frequency distribution of "icequakes" is approximately power-law, similar to the famous Gutenberg-Richter law for earthquakes. This has intriguing potential for future comparisons with earthquake studies.

3.1 Introduction

Results from the previous chapter demonstrated that rift propagation occurs in episodic bursts. Each burst, deduced from seismic swarms coincident with rapid rift-widening, lasted approximately 1-4 hours and had recurrence intervals ranging from 10 to 24 days. Unfortunately, with only one field season of measurements, it is difficult to know whether these observations are representative of typical behavior and how varied the recurrence intervals between propagation events may be. In addition, the small number of seismic stations and low sampling frequency made it difficult to accurately locate seismic events.

In this chapter we present results from two additional field seasons during which we deployed a more densely-spaced seismic and geodetic network. The network was specifically designed to improve our ability to identify and locate rift-related icequakes. These measurements were conducted on the Amery Ice Shelf over the Austral summer of 2004-05 and 2005-06. Although one of the goals of this study was to confirm our results from 2002-03, we also wanted to extend the time series of rupture events to provide a better statistical sample of (i) recurrence times between swarms and (ii) the number of events in each swarm and magnitude of rift-widening during each swarm. Although this type of methodology is common when studying earthquakes, it has never before been applied to ice shelf rifts or any other type of glaciological fracture.

3.1.1 Implications for the Mechanics of Ice Shelf Rifting

Improving our knowledge of icequake locations and recurrence intervals between swarms is crucial to developing mechanical models of ice shelf rifting. For instance, we do not yet know how stress accumulates and is released near the rift tip, a process closely intwined with the magnitude and recurrence interval between propagation events. In addition, the spatial distribution of seismic events provides important clues about the rifting process. If seismic events are well localized in a thin strip along the rift then it indicates that strain energy is also concentrated in a narrow region around the rift tip, consistent with the assumptions of linear elastic fracture mechanics (Lawn, 1993). In contrast, if seismicity is more diffuse with a larger radius of fracturing then considerable strain energy might be dissipated by the generation of micro and meso-scale fracturing ahead of the rift tip, consistent with some models of subcritical crack propagation (Atkinson and Meredith, 1987). Another important question is whether seismic events originate at the surface of the ice, the bottom or somewhere in between.

Earthquake mechanics may provide an appropriate analogy to rifting that can be exploited. Figure 3.1 shows three different models of stress accumulation and release discussed by Shimazaki and Nakata (1980) to explain earthquake recurrence intervals. Taking a liberal definition of slip to include rift widening events, we can directly apply models of earthquake recurrence intervals to rift propagation events. Figure 3.1 (a) shows a model that is predictable in both magnitude and time based on the early ideas of Reid (1910). Propagation events occur when the stress near the tip exceeds a critical stress, σ_2. After each propagation event the stress (and slip) drops to a constant value, σ_1, from which it begins to rise again. In this model not only are the time and magnitude of each event predictable, but events are periodic and have equal magnitudes. In the second model (Figure 3.1 (b)), it is assumed that propagation still occurs at a critical stress, σ_2, but the stress drops to different values following each event, leading to different amounts of slip. In this model the size of each event (i.e. amount of slip) varies, but if the

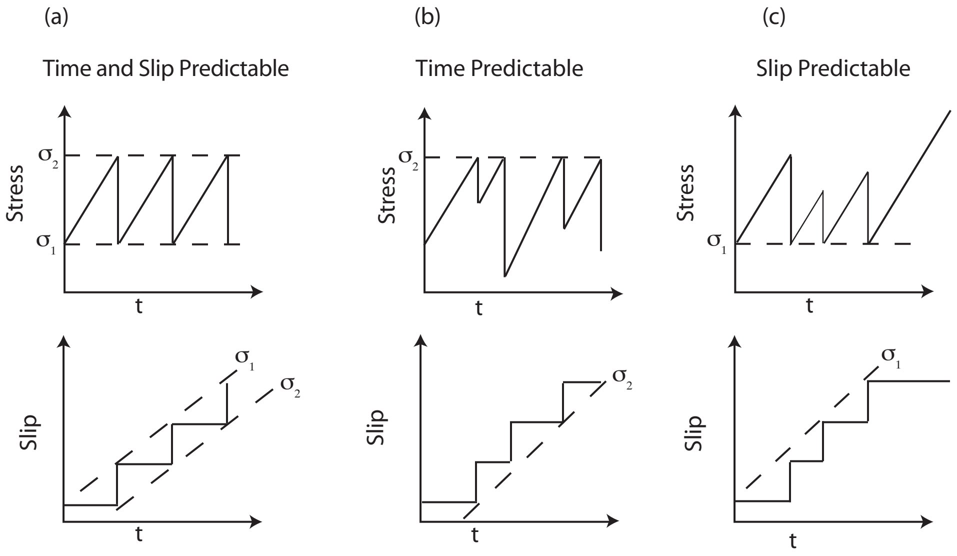

Figure 3.1: Three simple models of recurrence intervals: (a) Both time and slip-predictable; (b) time-predictable; (c) slip-predictable. The time-predictable model is based on the ideas of Reid (1910) in which stress accumulates until it reaches a critical value of σ_2 at which point there is a constant stress drop (and slip) to σ_1. In the time-predictable model fracture occurs at a critical stress σ_2 but the stress drop (and slip) varies. In the slip-predictable model the stress drop is constant, but the critical stress at which fracture occurs varies.

size of the previous event is known, then the time to the next event can be predicted, and this model is therefore called time-predictable. In contrast, the third model assumes that the critical stress at which propagation occurs varies, but that the stress falls to a constant value following each propagation event (Figure 3.1 (c)). This model is called slip-predictable because if the time of the previous propagation event is known, the slip of the next propagation event can be determined but the time of the next event cannot. The final possibility (not illustrated) is that both the critical stress, σ_2, and the final stress after propagation, σ_1, vary (perhaps randomly) between propagation events. In this case neither the size nor the time of events are predictable.

3.2 Overview of Field Campaign

The focus of our seismic network has been high-frequency "icequakes" believed to be generated by ice fracturing events. For this reason, we deployed a densely-spaced network of stations around the tip of rift T2 (Figure 3.2. We had originally planned on deploying seismometers and GPS around both rift T1 and rift T2, however, decreases in funding and logistical support forced us to scale back our plans.

During the Austral summer of the 2002-2003 field season we installed 8 single-component L-4C seismometers recording at 10 Hz (0.1 s) along with 6 dual-frequency GPS receivers recording at 0.033 Hz (30 s) for a 48 day pilot study around the tip of T2 (Chapter 2). During the 2004-05 and 2005-06 seasons we carried out field campaigns with 12 3-component L-28 seismometers and 12 dual-frequency GPS receivers recording at 0.5 Hz (2 s) for 52 days and 81 days, respectively. The higher sampling rate, made possible by the availability of larger capacity hard drives and solid state memory cards, provides greater sensitivity to events occurring over smaller spatial scales.

We positioned instruments several kilometers ahead and behind the rift to maximize the chance that the rift tip would be enclosed by our network (stations k,m and i,h in Figure 3.2) because it was unclear how accurately the surface expression of the rift expressed the true rift tip position. Having a network of stations that enclose the rift tip enables more accurate locations of seismic events to be determined. We also deployed a line of stations normal to the rift at the tip (stations a-f in Figure 3.2). The purpose of these stations was twofold: (1) The baselines can be used to examine the pattern of vertical deformation away from the rift using GPS and (2) four seismometers were placed with of spacing less than 1 ice thickness (400 m) providing sensitivity to very small amplitude events that occur very close to the rift tip. The other stations were placed at intermediate distances to form triangles along the length of the rift from which we could compute strain rates. The geometry of the network (Figure 3.2) was maintained

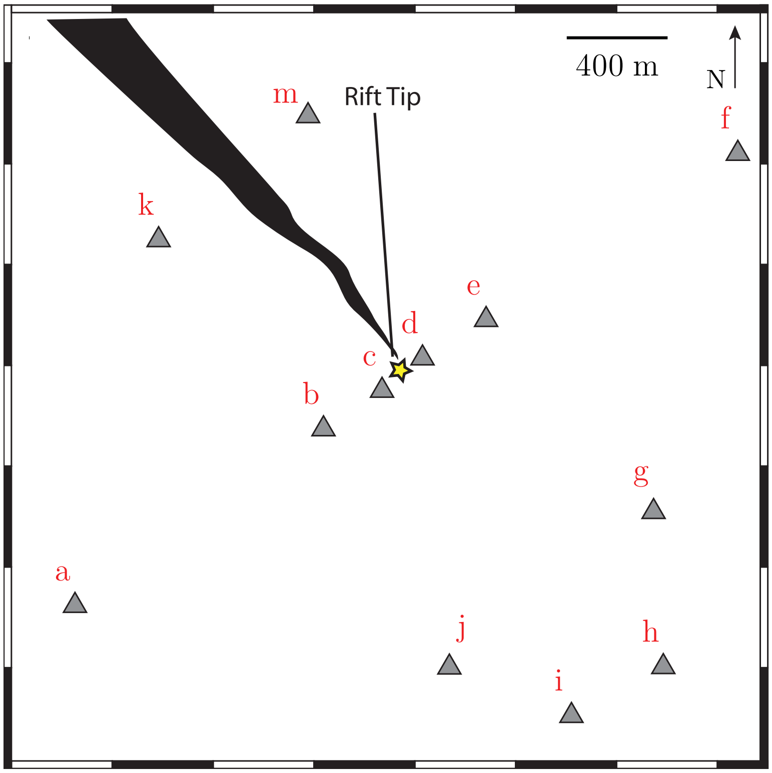

Figure 3.2: Diagram showing the relative positions of GPS and seismometers in relation rift T2. The geometry of the network did not vary between 2004-05 and 2005-06.

between 2004-05 and 2005-06. However, the center of the network was translated to account for both ice-flow and rift propagation so that the rift tip remained close to the center of the network at the beginning of each field season.

The similarity in network geometry facilitates comparisons between the 2004-05 and 2005-06, but the distances between stations were not exactly the same nor do we re-occupy the exact same sites. Comparison between the pilot field study (2002-03) and the following two field seasons (2004-05 and 2005-06) is complicated because not only was the geometry of the network different, but because we also used different seismometers with different sampling frequencies. The low sampling frequency (due to storage limitations) of 10 Hz during the 2002-03 field season combined with the anti-aliasing filter used cut down our bandwidth to frequencies between 1-5 Hz. Unfortunately this barely overlapped with the response of the L-28 seismometers deployed the following two seasons with a natural period of

5 Hz. Most of our L-28 seismometers operated continuously during deployment. During the 2004-05 season, the aluminum poles on which the GPS antenna were placed melted out and tipped over during the first 20 days of deployment, because they were not placed deep enough in the snow. During the 2005-06 field season poles were placed deeper into the snow and the aluminum poles were replaced with wooden poles to minimize heat conduction.

The tip of the rift was not well defined but instead tapered off into a series of micro-scale and meso-scale cracks (Figure 3.3, left panel). We identified a position near the end of this network of fractures as the “best guess” location of the rift tip. This location, determined from helicopter flights was chosen near the region where no cracks were visible on the surface of the ice. This location was typically several kilometers ahead of where the rift tip was identified in satellite images because of errors in geolocating the images and because of the pixel size in the images ($\sim$250 m). We again noticed that the interior of the rift was filled with large blocks of ice that had fallen in from the sides. Some of these blocks were almost completely covered with snow. Between field seasons we saw substantial variation in the amount and thickness of the debris that filled the rift. We were not able to tell whether this was because of active rearrangement of blocks within the rift or seasonal variation in the snow that covered the rift. We also noticed that the rift propagates through a field of longitudinal to flow (and normal-to-rift) crevasses (see Figure 3.3). Early in the field season snow bridges obscured many of these. Later in the season, many of the snow bridges appeared to sag and collapse revealing the full extend of the crevassing. Another feature that we noticed was that the north side of the rift was uplifted by about 1 meter relative to the southern side, with the amount of uplift decreasing towards the tip (see Figure 3.3).

For semantic simplicity we refer to the 2002-03 field season as “season 1” the 2004-05 field season as “season 2” and the 2005-06 field season as “season 3”. Another convention that we adopt is that we reference days of our survey relative to day of year 332 (November 27th, 2004 and November 28th, 2005, respectively).

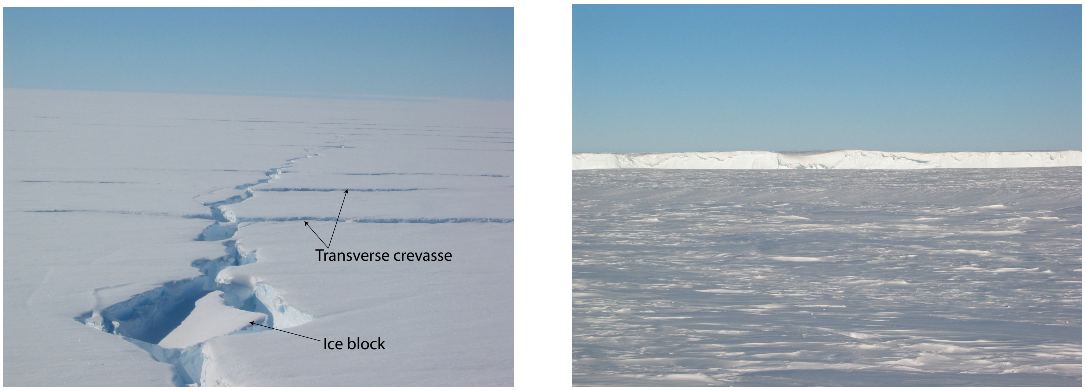

Figure 3.3: Left: photograph taken looking east towards the rift tip showing how the rift tapers off towards the tip. Also note the normal-to-rift crevasses visible; taken by M. Woolridge. Right: photograph taken from the south side of the rift, looking north; taken by R. Coleman.

This facilitates comparison of timing between field seasons. For the purposes of our seismic analysis, we also consider only seismic events detected at four or more stations (described in more detail in section 3.3). This eliminates spurious associations caused by electronic spikes. It also enables us to locate all of the events used in our analysis and to determine whether they have an origin within our study region or originate outside (e.g. small calving events from the ice-front).

3.3 Seismic Processing and Results

3.3.1 Event Detection Algorithm

While hand-picking each seismic arrival would yield more accurate results, the high data volume necessitated automating the procedure. A number of algorithms have been developed over the years to automatically detect seismic events (Withers et al., 1998; Allen, 1982). One of the most popular of these uses the ratio of short-term and long-term average amplitudes of the seismogram (STA/LTA) (Withers et al., 1998; Earle and Shearer, 1994). We have developed a variation of the STA/LTA algorithm specifically designed to detect icequakes that we observed with our high-frequency seismometers. Our implementation of this algorithm consisted of the following steps:

1. Band-pass filter each component (i.e. North, East, Up) in the range f_1 to f_2. Most of the energy in the waveforms is typically in the range 5-50 Hz but we have experimented with different filter windows (detailed below).

2. Calculate the envelope function for each component. The envelope function, defined as the analytic signal multiplied by its complex conjugate, is less phase sensitive than the waveform itself.

3. Calculate the power-time series by summing the squares of the envelope function for each component.

4. Use the power-time series to calculate the median of the signal over a long interval T_{long} and the mean of the signal over a shorter interval T_{short}. Rather than use the long-term mean of the power-time series, as is usually done, we have found that the median is more robust during periods when we have electronic spikes in the data. We found that a long term interval of 1 hour and a short term interval of about 0.25 seconds gave us the best results (see below).

5. When the ratio of the short-term average to long-term median (STA/LTM) exceeds a defined threshold, S_{min}, longer than a pre-defined time period $T_{duration}$, we designate this an event. The time at which the envelope exceeds S_{min} determines the arrival time. We also record the time at which the STA/LTM exceeds both lower and higher thresholds to determine how emergent or impulsive each waveform is. This also gives an estimate of the uncertainty of our arrival time picks. To prevent detecting the same event twice, we have a latency period of 1.5-s before our algorithm is allowed to "trigger" on the next event.

There are several tunable parameters in this algorithm that we have experimented with, including the band-pass window, T_{long} and T_{short}, and the threshold detection limits. For the band-pass window, we ultimately chose a band-pass filter range from 5 to 35 Hz. Because our seismometers had a corner frequency of

5 Hz, using lower frequencies had little effect on our results. Lowering the filter high-pass corner frequency below about 25 Hz smoothes the waveform out to such an extent that picks were correspondingly less accurate. We choose 1 hour for T_{long} but found that varying it between 0.5 hr and 2 hrs had little effect on the arrival times picked. Detections were sensitive to the combination of detection threshold S_{min} and the short-term interval, T_{short}. We needed to chose a relatively short T_{short} because many of the smaller events had durations less than 1 second. We chose the combination of T_{short} and S_{min} in order to best match the arrival times for 200 events that were picked manually.

One drawback to our approach is that we were not able to obtain phase information about waveforms. For most waveforms, we cannot distinguish between the P-wave arrival and the S-wave arrival. Because of the small spatial scale of our network, many seismic stations would be within a distance of one wavelength from the source. At these short distances, the separation of waveforms into P and S waves does not apply. Even for larger source-receiver distances on the order of 1-2 km, we only expect to get a 0.2 second time difference. This makes it unlikely that we will be able to distinguish between P and S waves in our waveforms. The principal difference between our algorithm and those commonly used in earthquake seismology is that in our algorithm, we exploit the lack of differentiation between phases by summing all components. This allows us to pick events that have small signal-to-noise ratios in each individual channel, but are coherent when the channels are summed together.

3.3.2 Event Association Algorithm

We use a simple approach to associate arrivals detected at multiple stations with common events:

1. We first sort all of the arrival times into a list with the earliest detections occurring first, regardless of stations.

2. We then calculate a matrix of travel times between the i_{th} and j_{ith} stations

(δt_{ij}). This is an upper bound on the travel time differences between events recorded at two different stations.

3. For each arrival time in the arrival time list we search for arrival times at other stations that fall within $\Delta = |t^i_{master} - \delta\tau_{ij}|$, where we have labeled the ith arrival time in the list t^i_{master}. We associate all arrival times that we find with the master station. These arrival times are then flagged and cannot be associated with other events.
4. If we find multiple arrival times at the same stations, we decrease our window size until we have only one arrival for each station. For events that are closely spaced this may result in a mis-association but most events are spaced more than several seconds apart. Events separated by less than 2 seconds constitute less than 1% of events that we detected resulting in a negligible effect on our results.

Once our catalog of events has been constructed we remove all known earthquakes using the USGS earthquake catalog.

3.3.3 Event Location Algorithm

We use a two-step procedure to determine event locations. First we determine preliminary locations for all events detected at 4 or more stations using a three-dimensional grid search with a constant velocity model. We then use cross-correlation methods between all events separated by a 3 km radius or less. These adjusted picks are then used to relocate all events using the same grid search algorithm.

Grid Location Algorithm: Our preliminary locations were derived using a three-dimensional grid location algorithm (see e.g. Shearer,1997). We define a three-dimensional grid of points with horizontal range 10 km, depth 400 m (the ice thickness) and spacing between grid nodes 25 m centered on the location of the rift tip identified in the field. We then compute travel times from each grid point to each of our stations using a seismic velocity ranging from 2000 m/s in steps of 500 m/s to 3000 m/s. Because we are assuming a constant velocity, the ray paths are straight lines and the predicted travel time from a source located at (x_m, y_m, z_m) with an origin time t_m to the ith station is simply the Euclidean distance between source and receiver divided by the velocity:

$$T_i^{pred} = t_m + \frac{1}{V}\sqrt{(x_i - x_m)^2 + (y_i - y_m)^2 + z_m^2}$$

Each of our stations are on the surface, therefore $z_i = 0$. For each event, the observed arrival times are compared to the predicted travel times at each grid point and the best fitting location is determined from the smallest residual. Following Shearer (1997) we use the L_1 norm (i.e. absolute value of the differences between predicted travel times and observed travel times):

$$L_1 = \Sigma_i \left| T_i^{pred} - T_i^{obs} \right|$$

The L_1 norm assigns less weight to outliers than the L_2 norm used in traditional least-squares fitting. As pointed out in Shearer (1999) it is not necessary to search for the best fitting origin time for each grid point. The origin time is simply the median or mean of the residuals (for the L_1 and L_2 norm, respectively). We then find the seismic velocity that minimizes the L_1 norm of the residuals for all events at all stations.

Waveform Cross-correlation: One of the major limitations in deriving locations from arrival times is the limited accuracy of the automated arrival time picks. Some improvement could be made by the painstaking process of manual picking but the time overhead is prohibitive for this to be a practical solution. Instead, waveform cross-correlation techniques have been developed to improve the precision of arrival time picks (Poupinet et al., 1984; Ito, 1985; Gillard et al., 1996; Shearer, 1997). Although waveforms of events recorded at different stations may not be similar, different (but closely spaced) events observed at the same station are often similar. For these events we can use waveform cross-correlations to improve the arrival time picks. Unfortunately, this is a computationally expensive task. The number of cross-correlations required for n events is $n(n-1)/2$. With 12 stations and 3 components per station this means we need to compute $n(n-1)/2 \times 36$ cross-correlations. The number of computations become prohibitively expensive for large n. Instead of cross-correlating all events detected at a station with all of the other events detected at that station we reduce the number of cross-correlations by only cross-correlating events that are separated by 3 km or less (as determined by our preliminary grid-location algorithm). For these events, we cross-correlate using a 5-second window around the arrival time of each event and maximum time shift of ±70 samples (0.35 s) after filtering between 5-35 Hz. The window length, filter bandwidth and maximum time shift was chosen to cycle skips when cross-correlating the waveforms. Even with this reduced set we still need to compute over 500 million cross-correlations. After cross-correlating waveforms, we combine the three components (*North, East, Up*) by taking the mean of the cross-correlation coefficient and the mean of the time differences for all three components. We use the difference between time shifts of the two horizontal components as proxy for the precision of the time shifts determined. We found that the differences in timing between the two horizontal components was typically less than 5-10 samples (0.025-0.05 seconds) for a mean cross-correlation coefficient of 0.8 or higher. We only use cross-correlations with a mean cross-correlation coefficient greater than 0.8 to solve for improved timing of events, about 23% of the original dataset. The relation between the vector of adjusted picks and the observed picks can then be expressed as a matrix equation:

$$\mathbf{d} = \mathbf{G}\mathbf{m} \tag{3.1}$$

The vector $\mathbf{d}$ contains a vector of arrival time picks and timing from correlations. The vector $\mathbf{m}$ contains the adjusted picks to be solved for. For example, for three events we would have:

$$\begin{pmatrix} t_1 \\ t_2 \\ t_3 \\ \tau_{12} \\ \tau_{13} \\ \tau_{23} \end{pmatrix} = \begin{pmatrix} 1 & 0 & 0 \\ 0 & 1 & 0 \\ 0 & 0 & 1 \\ 1 & -1 & 0 \\ 1 & 0 & -1 \\ 0 & 1 & -1 \end{pmatrix} \begin{pmatrix} T_1 \\ T_2 \\ T_3 \end{pmatrix} \tag{3.2}$$

We denote the timing differences from the cross-correlations by τ_{ij}, the corrected travel times by T_i and the observed travel times by t_i. Equation 3.2 constitutes an over-determined system that can be solved using standard linear algebra techniques.

3.3.4 Temporal Trends in Seismicity

There was a slight but significant decrease in the rate of seismicity between the two field seasons from about 80 events per day to 63 events per day, roughly a 10% decrease in the frequency of events. To compare in more detail the variations in the the temporal trends in seismicity we computed histograms of the number of events (using three hour bins) for seasons 2 and 3 (upper two panels in Figure 3.4). Inspection of Figure 3.4 shows three swarms of seismicity during the 2004-05 field season. Each of these swarms lasts 1-3 hours and consists of 150-350 events. We see a pronounced change in behavior during the second field season, where we can only identify one clear swarm. The single swarm identified in season 3 contains fewer events (50-100) than each of the three swarms identified in season 2.

We also analyzed the relative magnitudes of the seismic events detected. We determined relative magnitudes of events by taking the log_{10} of the peak amplitude of the seismogram for each event at the station closest to the source of the event. The temporal trend in event magnitudes is illustrated in Figure 3.4. We see that each swarm contains events of all magnitudes. In between swarms, there are

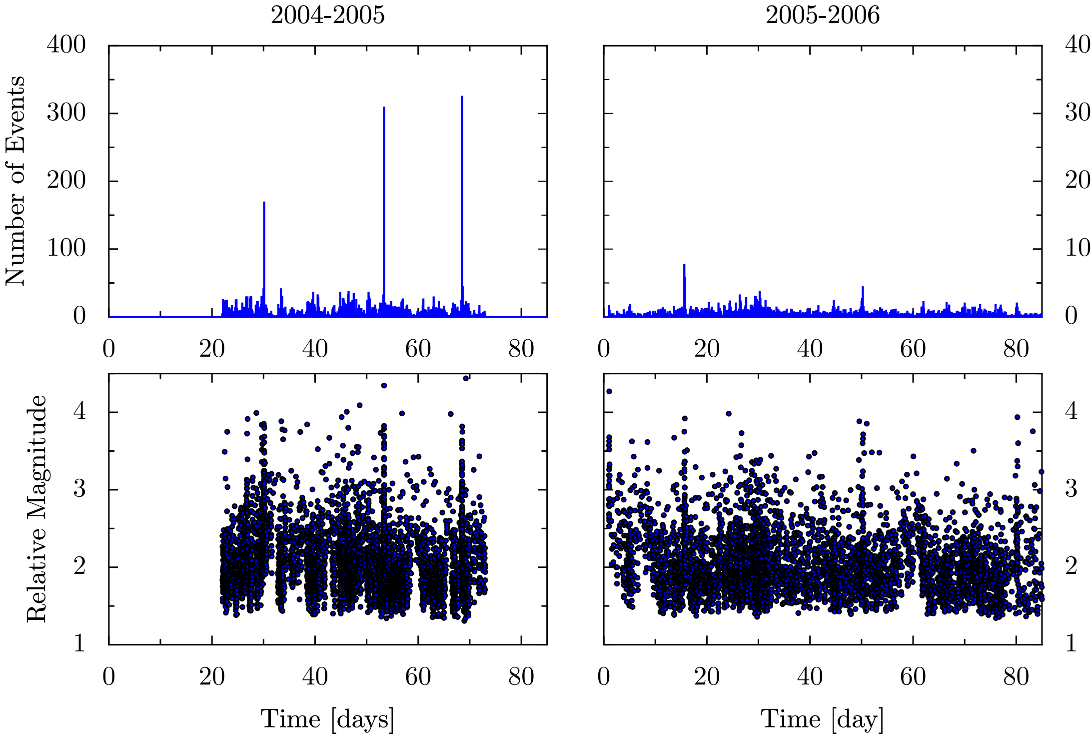

Figure 3.4: Upper panel: Histogram of the frequency of seismic events (bin size = 3-hr) or season 1 and season 2. Lower panel: Temporal distribution of the magnitudes of events for each season.

a few large events but most of the background seismicity consists of low magnitude events.

3.3.5 Event Locations

Figures 3.5 and 3.6 show a map view of the locations of events determined using our grid search algorithm (section 3.3.3) for season 1 and 2, respectively. We found that the best fitting seismic velocity was between 2000 m/s and 2500 m/s - similar to both the shear wave speed in meteoric ice and the velocity in the upper fifty meters of the ice shelf (McMahon and Lackie, 2006). This indicates that the seismic events have shallow epicenters or that we detect little P-wave energy from the waveforms. Also shown in Figures 3.5 and 3.6 is the relative magnitude of events, indicated by the size of the filled circles. Seismic events show strong clustering along the rift axis, with a long tail extending several kilometers

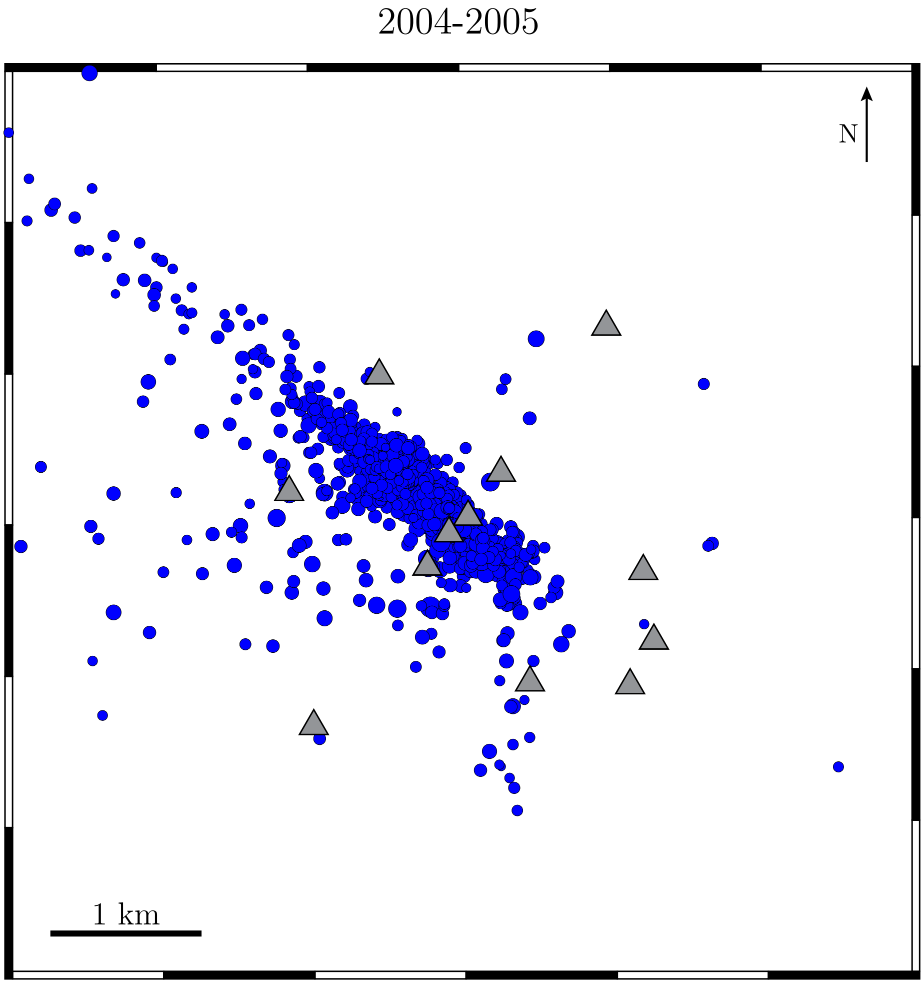

Figure 3.5: Map showing the locations of events (blue circles) that were located with respect to the network geometry for the 2004-05 field season. Size of each circle is proportional to the $\log_{10}$ of the peak amplitude of the seismogram at the station closest to the event. Gray triangles indicate the locations of the seismometers.

up from the rift tip towards the triple-junction. In contrast, there is a decrease in seismicity ahead of the rift tip. In season 2 there is also a large cluster of seismic events with small magnitudes about 500 m ahead of the rift along with a long tail of events of increasing magnitude up-rift. To test whether this spatial pattern of seismicity was caused by the geometry of our network, we cross-validated our results by relocating all events, each time with a different station omitted, for all 12 stations; this is akin to the so-called “jack-knife” method in statistical estimation.

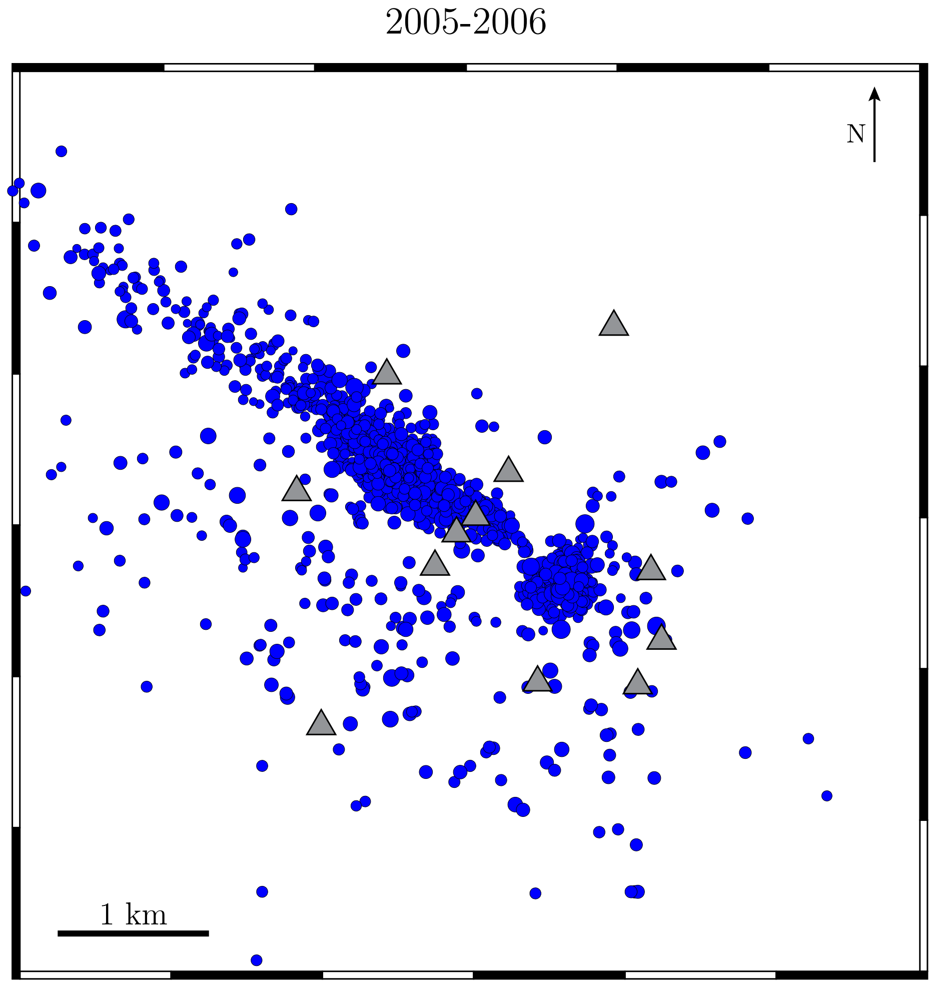

Figure 3.6: Map showing the locations of events (blue circles) that were located with respect to the network geometry for the 2005-06 field season. Size of each circle is proportional to the $\log_{10}$ of the peak amplitude of the seismogram at the station closest to the event. Gray triangles indicate the locations of the seismometers.

This did not significantly affect the horizontal positions of the events nor did it substantially affect the relative magnitudes determined for the events. However, it did significantly alter many of the depths we derived by up to several hundreds of meters. This suggests that our network does not have adequate resolution to determine depths of events. For this reason we restrict our discussion to horizontal positions for the rest of this chapter. To obtain improved vertical locations for the seismic events, it would be necessary to either increase the density of the network such that station spacing was less than one ice thickness (i.e. about 50-100 meters separation) or alternatively bore-hole seismometers could be placed several hundred meters down into the ice. Both of these options are currently too difficult to logistically support. Figures 3.5 and 3.6 show that the locations of events during each seismic swarm were not tightly clustered. Instead they formed linear swaths along the rift. We did not try to identify focal mechanisms for seismic events because it appears that the first detected arrival may be a shear-wave.

3.4 GPS Processing and Results

3.4.1 GPS Processing

GPS data were processed as kinematic sessions using the RTD software package (Bock et al., 2000) (see also Chapter 2). Using this method we obtained positions for each station at each epoch (i.e. every 2 seconds), generating a times series of positions for each station. These positions are relative to a chosen master station. We used the same technique as described in Chapter 2 but the higher sampling rate and shorter baseline distances yielded solutions with less noise. A further advantage of relative kinematic processing is that common motion due to ice flow (lateral) and tides (vertical) are removed. The disadvantage of this technique is that we cannot resolve regional motion due to tides. After processing, all outliers greater than 3.5 times the interquartile range of the detrended baseline lengths were discarded. The censored time series was then smoothed using a 5 minute gaussian-running mean. The higher sampling frequency (2 seconds versus 30 seconds) and shorter baselines between stations in comparison with season 1 enabled us to use a shorter duration filter to obtain a comparable signal reduction in signal to noise ratio. Because the size of the rift-widening signal that we saw during season 1 was $\sim$1 cm, we chose a smoothing interval that reduced the RMS noise of the signal to be of the order of 3- 5 mm, depending on baseline length. GPS data were more challenging to interpret than the seismic data because the

GPS antenna poles fell over early on in season 2.

3.4.2 Strain Rates

Strain rates primarily reflect the large-scale and longer time scale deformation of the ice shelf. To compute strain rates we first tessellated our network of GPS sites into individual triangles using Delaunay triangulation (e.g. Schroeder and Shephard, 1988). We then computed relative velocities between stations using a least-squares fit to the full time series of GPS positions. For most stations, because of the 2 second sampling frequency of our GPS, we had more than 10^5 points to use in estimating the velocity. Because the uncertainty in the standard error decreases like one over the square root of the number of points, this resulted in low standard errors for all of our GPS derived velocities. The velocities were then used to compute strain rates for each triangle separately using standard geodetic techniques (see e.g. Malvern, 1969). The eigenvalues and eigenvectors of the matrix representation of the strain rate matrix then give the principal strain rates and principal axes. The strain rates calculated along with their standard error are displayed in Table 3.1. Standard errors computed were computed for each triangle (see e.g. Taylor, 1997 Chapter 8). The errors shown in Table 3.1 are quite small, typically several orders of magnitude smaller than the strain rates. However, the standard error is almost certainly an underestimate of the true error because the strain rate may vary across each triangle. All strain rates were extensional with typical magnitudes ranging between about $10^{-5} - 10^{-4}$ per day.

The principal axis of the strain rates are displayed in Figure 3.7. Examination of Figure 3.7 shows that the largest principal strain rates occur in triangles anchored on both sides of the rift (triangles $c - d - k$ and $d - c - g$). In these triangles, the principal strain rate is aligned in a direction close to rift-parallel. In contrast, those triangles that outline an area that is entirely on one side of the rift have principal axes that are close to rift-parallel, indicating that normal-to-rift stress is primarily accommodated by rift widening. Looking at the strain rates

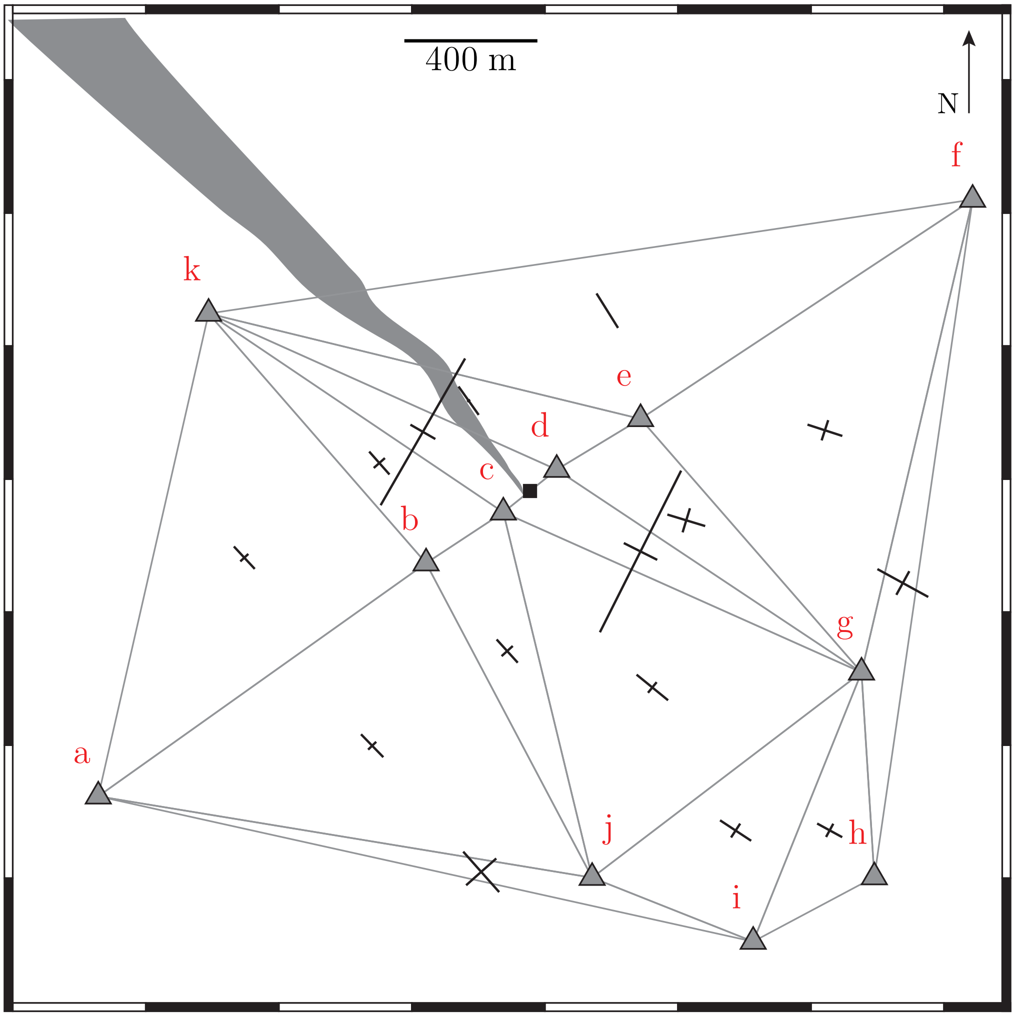

Figure 3.7: Map of the orientation of the principle axes of the strain rate tensor for the 2005-2006 field season (black lines). The length of each axes is proportional to the strain magnitude. The gray triangles show the station triangulation used to calculate each strain rate tensor. The approximate rift tip (shown as a black square) was located between stations c and d. An approximate outline of the rift (filled gray region) is included to show the orientation of each triangle used to compute a strain rate relative to the rift.

Table 3.1: Principal strain rates calculated for each triangle. E_{11} is the smallest principal strain rate and E_{22} is the largest. θ is the angle that the largest principal axis makes with the East-West axis. The formal error in the calculation is probably an underestimate of the true error. The largest uncertainties in the direction of the principal axes was 2 degrees.

triangle	E_{11} [10^{-4} **per day**]	E_{22} [10^{-4} **per day**]	θ [degrees]
j-i-a	0.60 ± 0.0040	0.437 ± 0.0029	42.3
b-k-a	0.37 ± 0.0003	0.127 ± 0.0003	42.2
b-k-c	0.37 ± 0.0003	0.165 ± 0.0004	41.3
b-j-a	0.39 ± 0.0004	0.132 ± 0.0001	44.0
b-j-c	0.39 ± 0.0002	0.169 ± 0.0002	42.6
e-k-f	0.50 ± 0.0400	0.016 ± 0.0372	31.1
d-k-c	0.34 ± 0.0004	2.051 ± 0.0003	60.1
d-e-k	0.41 ± 0.0005	0.041 ± 0.0006	35.8
g-h-i	0.35 ± 0.0004	0.180 ± 0.0006	61.8
g-j-i	0.43 ± 0.0004	0.200 ± 0.0006	56.6
g-h-f	0.67 ± 0.0600	0.322 ± 0.0962	60.9
g-e-f	0.44 ± 0.0300	0.253 ± 0.0204	71.9
g-d-e	0.48 ± 0.0001	0.310 ± 0.0001	73.1
g-j-c	0.50 ± 0.0001	0.164 ± 0.0001	50.6
g-d-c	0.46 ± 0.0003	2.200 ± 0.0001	63.3

ahead of the rift tip (e.g. triangles $i - j - g$, $i - h - g$ and $i - j - a$), we see little evidence for rift-widening, suggesting that the surface expression of the rift is a good indication of true rift position (i.e. the rift tip is not obscured by snow bridges). Overall we see high strain rates across the rift indicating that the rift is widening at a rate that is larger than the glaciological spreading rate seen in triangles confined to the rift. We also see that the orientation of the principal axes of the strain rates rotates counter clockwise in the stations ahead of the rift tip (see, for example, triangles a-i-j, j-i-g, d-g-e).

3.4.3 Vertical Velocities

The vertical strain rate is more difficult to visualize than the horizontal strains. Rather than computing the vertical strain for all triangles in our tessellation, we computed the vertical velocity for each of the GPS stations $a - f$ using least-squares. These six stations that form a straight line normal to the rift axis.

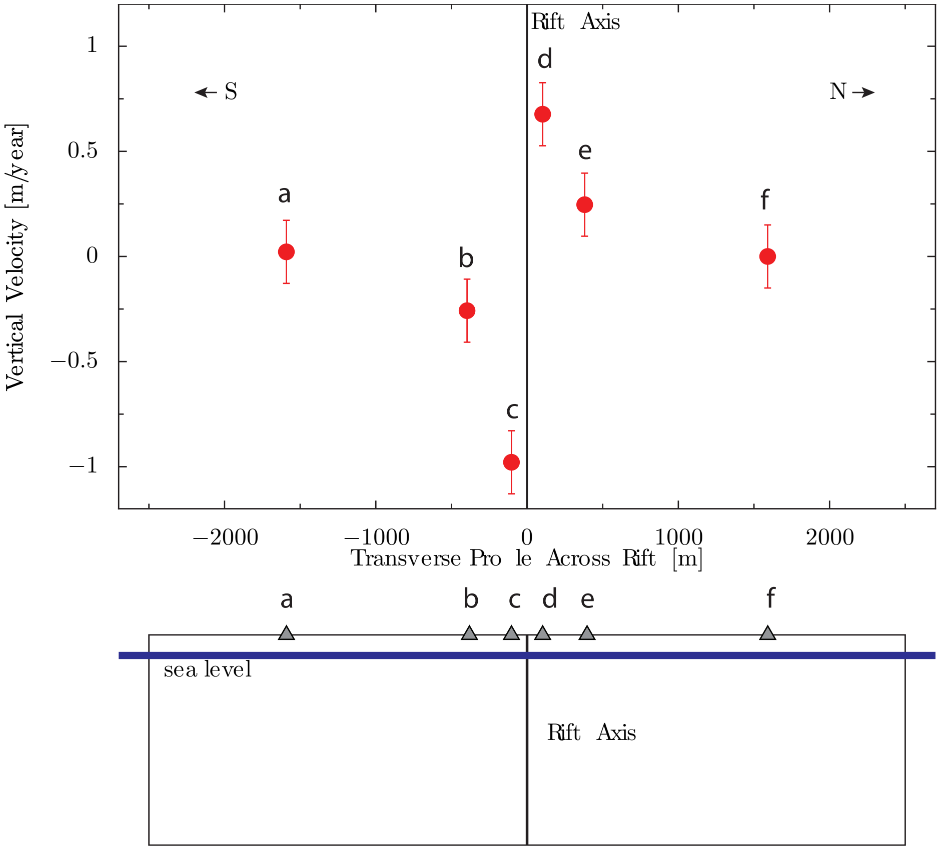

Figure 3.8: Differential vertical velocities for sites a-f. The rift is located at x=0 (indicated by a black line). The northern side of the rift is uplifted relative to the southern side. For this figure we have taken a reference frame so that the mean of the vertical velocity of site a and f are zero. Note the vertical exaggeration in both the upper and lower panels.

We chose our reference velocity to coincide with the mean of the vertical velocity of sites a and f. These relative velocities are shown in Figure 3.8. They suggest that the northern flank of the rift is uplifting relative to the southern flank, similar to what we have observed in the field. We discuss several hypotheses for the uplift in Chapter 5.

3.4.4 Rift Widening

To examine the rift widening signal in more detail, we resolved the rates of baseline extension defined by the stations a-f into rift-normal and rift-parallel components and then subtracted the linear trend to determine baseline residuals,

δD, for each station pairs. In contrast to the strain rates and vertical velocities that are determined by long-term trends, baseline residuals emphasize transient signals that depart from these term trends. Figure 3.9 shows the baseline residual for station pair d-c (see Figure 3.2 for the locations of the sites). We see large transients in all components starting at day 30 that indicate when the poles began to melt out; baseline residuals for this station pair are dominated by the GPS poles falling. Interestingly, the largest component of the transient is initially normal-to-rift and begins slightly after one of the swarms. However, this trend does not apply to all baseline pairs. After day 50 the rate at which the poles are falling accelerates and then we lose all signal beyond day 70. Qualitatively, we see similar trends in all baseline pairs, although the timing and speed at which the poles begin to fall over differs from station pair to station pair. We considered that part of this signal might be a real glaciological signal but the direction and magnitude of motion is incoherent across the GPS network. We know from our instrument recovery that the GPS poles did fall over, suggesting that this is, indeed, the source of the signal.

Figure 3.10 shows two baseline residuals from the 2005-06 field season. The baseline residual for station pair d-e, two stations on the same side of the rift, is shown in the upper panel. The lower panel shows the residual for baseline pair d-b, with two stations on opposite sides of the rift (see Figure 3.2). To stabilize the GPS poles during season 3, poles were drilled down 2 meters using an ice corer and, instead of using aluminum poles, we used wooden poles to minimize heat conduction. This appeared to eliminate part of the problem with GPS poles tipping over. After days 20-30 we again start to see large incoherent transients. One possible explanation for this signal is the “settling” of our GPS poles after temperatures began to increase and partially melt out the poles. In contrast to season 2, the poles did not completely fall over but we believe there was 5-10 cm of “give” that enabled the poles to tip over slightly. An alternative possibility is that the signal is related to processing artifacts, perhaps caused by ionospheric activity. Regardless of the origin, we do not believe that the signal seen in the

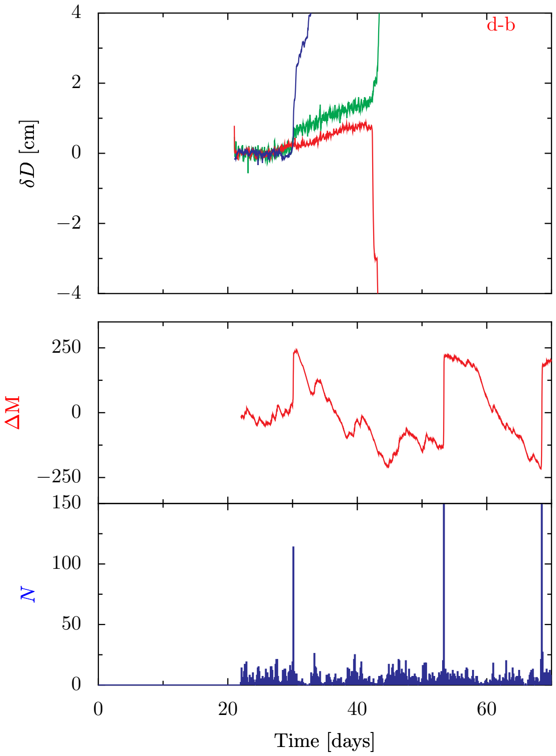

Figure 3.9: Residual for baseline pair d-b during the 2004-05 showing the GPS poles tipping over. Both of these sites began to fall over around day 30. This is the source of the large signal seen in the residual.

GPS represents a real glaciological signal and we therefore do not include this part of the data in the rest of the analysis.

There was one rapid rift widening event coincident with the single swarm of seismicity detected. This event (indicated with a circle in Figure 3.2) is present in the baseline residual that spans the rift (d-b) but not in the baseline residual of the station pair where both stations are on the same side of the rift (d-e). The magnitude of the signal is about ∼1 cm, large compared to the RMS noise in the signal (typically 1-3 mm). Baseline residuals for site pairs d-c (opposite sides of the rift) show a rift widening signal of similar magnitude to station pair d-b of about 1 cm. This similarity in size of the rift widening signal is consistent with a rigid body opening of the rift, as opposed to a deformation distributed over a larger area. We find further confirmation that this signal is rift-related by examining the baseline residual for station pair c-b (same side of the rift) which doesn't show rift widening. The widening is present and of constant magnitude in station pairs that span the rift but is not visible in station pairs on the same side of the rift. This strongly suggests that the signal is rift-related.

3.5 Discussion

Results from all three field seasons are summarized in Figure 3.11. There are three swarms of seismicity during season 1 and 2 and one swarm during season 3 (circled and labeled 1 through 7 in Figure 3.11). For all seasons except season 2 (because the GPS poles tipped over), each seismic swarm is accompanied by ∼1 cm of rift widening. One possibility is that events in the seismic swarms were caused by movement as the GPS poles fell over. Seismic signals related to GPS pole motion would have to travel greater than 1 km through the ice to be detected at 4 or more seismic stations. Moreover, the timing of the seismic swarms does not coincide very well with periods when the GPS poles were most rapidly falling over. The seismic signals and rapid rift widening seen in season 1 and season 2 confirm our conclusion from Chapter 2, that rift propagation is episodic.

In contrast to earthquakes, the recurrence relation between episodic propagation events is short (i.e. several weeks) and this enables us to begin testing various models of stress accumulation (Figure 3.1). If we take the rift widening signal as a measure of the size of each event, then each event is approximately the same size, ∼1 cm. Figure 3.12 shows the slip as a function of time for seasons 1 and 2, where we have assumed that the slip in between rift widening events is small. We have only three events making it difficult to conclusively rule out any of the models. However, with the limited data we have, the best fitting model is slip-predictable (Figure 3.1 (c)). The slopes in the best-fitting line for each of these seasons (dashed black line and dashed blue line, respectively) are statistically identical. This implies that the critical stress at which each propagation event occurs is constant, but that the stress drop varies between events. Unfortunately,

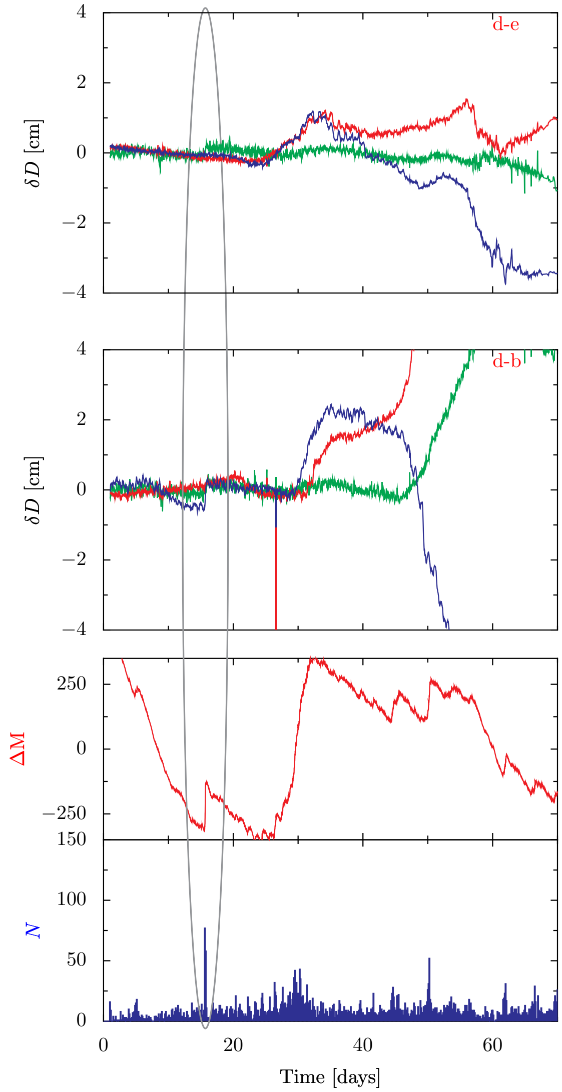

Figure 3.10: Upper panel: Baseline residual for station pair b-e, which are on the same side of the rift. Middle panel: Baseline residual for station pair d-b, which are on opposite sides of the rift. For both of these panels the green line is the vertical component, the blue line is the normal-to-rift component and the red line is the parallel-to-rift component of the baseline residual. Lower panel: Histogram of the number of seismic events (N), bin size is three-hours along with detrended cumulative moment ΔM. One rapid rift widening event was detected that was not related to poles settling (circled). The timing of the rapid rift widening event corresponds to a seismic swarm.

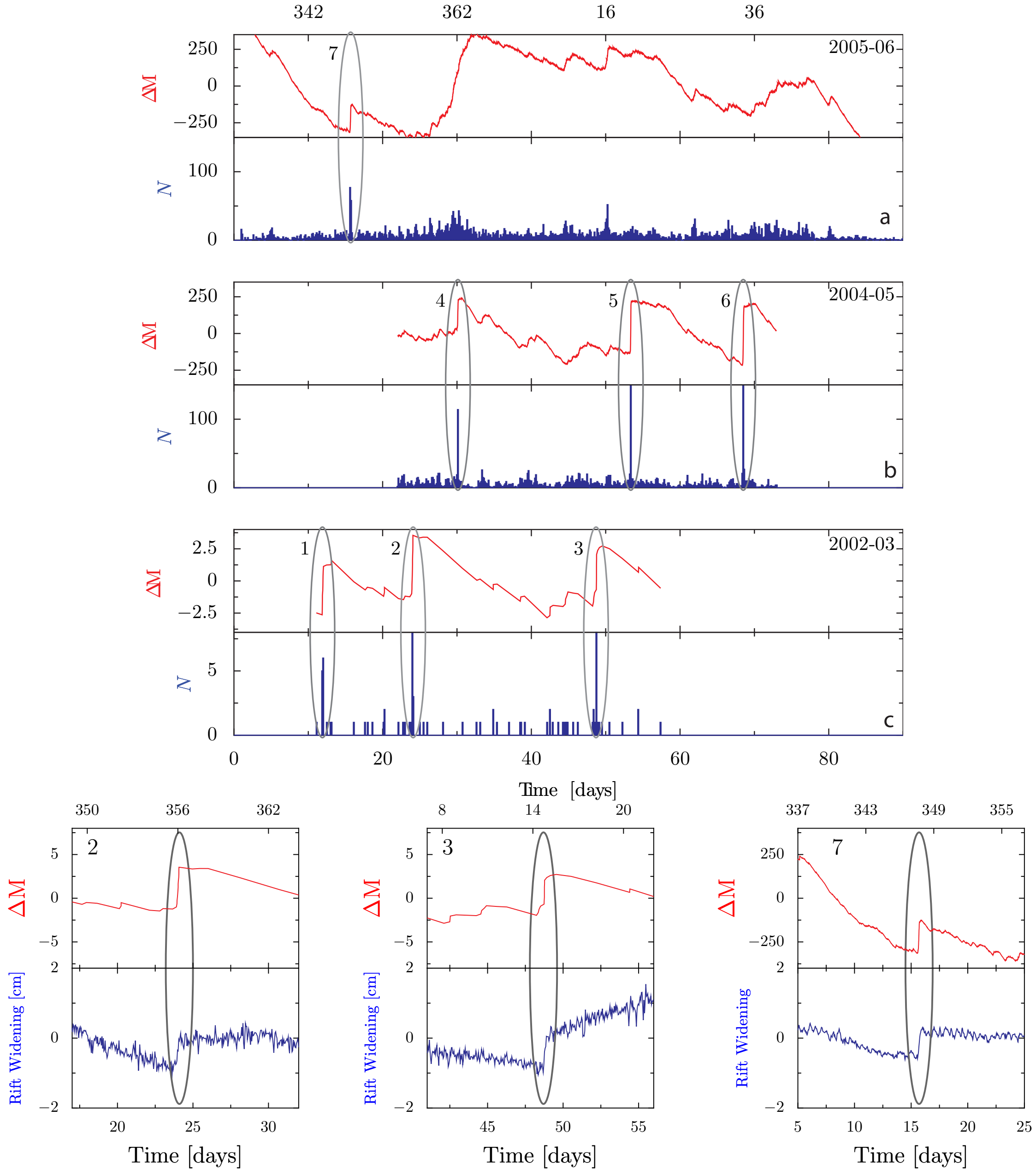

Figure 3.11: De-trended cumulative seismicity (ΔM) with a histogram showing the number of events per three-hour bin for (a) 2002-03 field season, (b) 2004-05 field season and (c) 2005-06 field season. Lower three panels: Zooms showing the rapid rift widening during three of the swarms Each swarm is circled and labeled 1-7 for later reference.

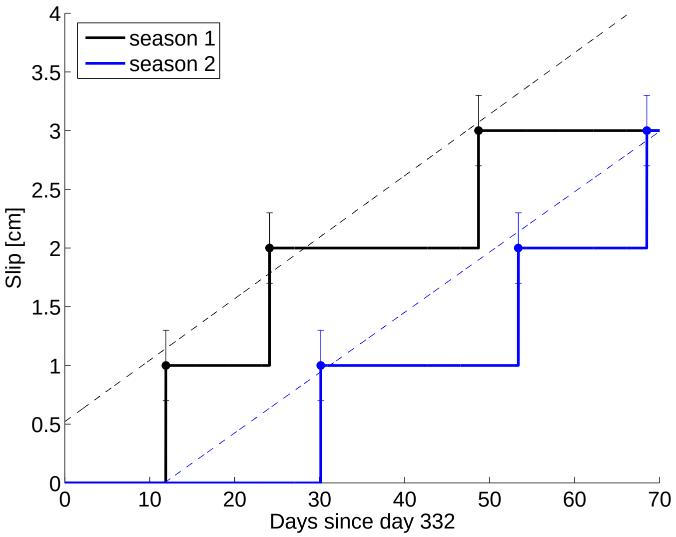

Figure 3.12: Recurrence times of rift widening events for season 1 and 2. The dashed black line indicates the best fitting slip-predictable model for season 1 while the dashed blue line indicates the best fitting slip-predictable model for season 2.

this fit is only marginally better than either of the other two models. Nonetheless these results suggest that we would detect enough propagation events to decide which model is appropriate if we were able to deploy instruments over a full year . However, during season 3 we see a departure from this behavior, where we observe only one seismic swarm over 80 days. This raises the question: What caused the decrease in the number of propagation events?

3.5.1 Comparison of Seismicity with Satellite Imagery

One explanation for the decreased seismicity is that part of the variations we see in the seismicity is merely due to intrinsic variations in propagation rates that are not resolved over the short duration of our field campaigns. To test this it is necessary to obtain continuous measurements over a longer period of time. Another more promising possibility is that the decrease in seismicity is related to the rift slowing down. To see whether the decrease in the rate of seismicity corresponds to a decrease in the rate of long-term rift propagation, we compared our field results with rift propagation rates derived from the Multi-Imaging-Spectral-Radiometer

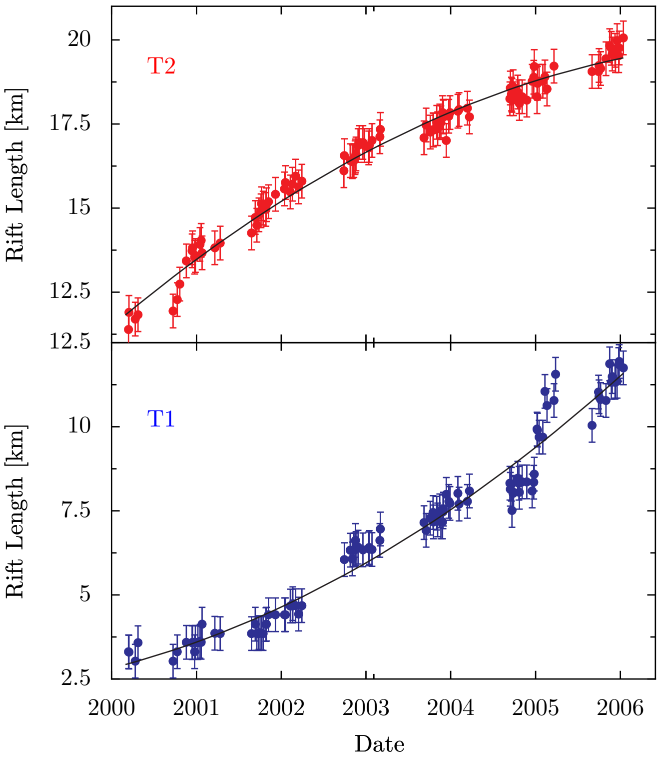

Figure 3.13: Time series of rift lengths for T1 and T2 derived from MISR. Upper panel: Shows rift length of T2. Lower panel: Shows the rift length of T1. The error bars shown are more conservative than those used by (Fricker et al., 2005a). Instead of using 1 pixel we used the maximum decrease in rift length between successive points within each season (i.e. we assume a measurement indicating that the rift closes is due to measurement error).

(MISR) for rifts T1 and T2 (Fricker et al., 2005b). Figure 3.13 shows the rift lengths of T1 and T2 from Fricker et al. (2005b) extended until January 2006. Also shown is a quadratic fit to the time series of rift lengths for both rifts. Measurements are only available between October-March, when there is sufficient light from the sun, hence the gap over each winter. There is an overall decrease in propagation rate for T2 along with a simultaneous increase in propagation rate for T1. This is consistent with our results for T2. It also indicates that these two rifts are not propagating independently of each other. In addition to the long-term trend there is considerable variation in the satellite measurements of rift length. Figure 3.14 shows the MISR measurements that coincide with our field studies. The propagation events that we measure are unresolvable in the MISR data. This

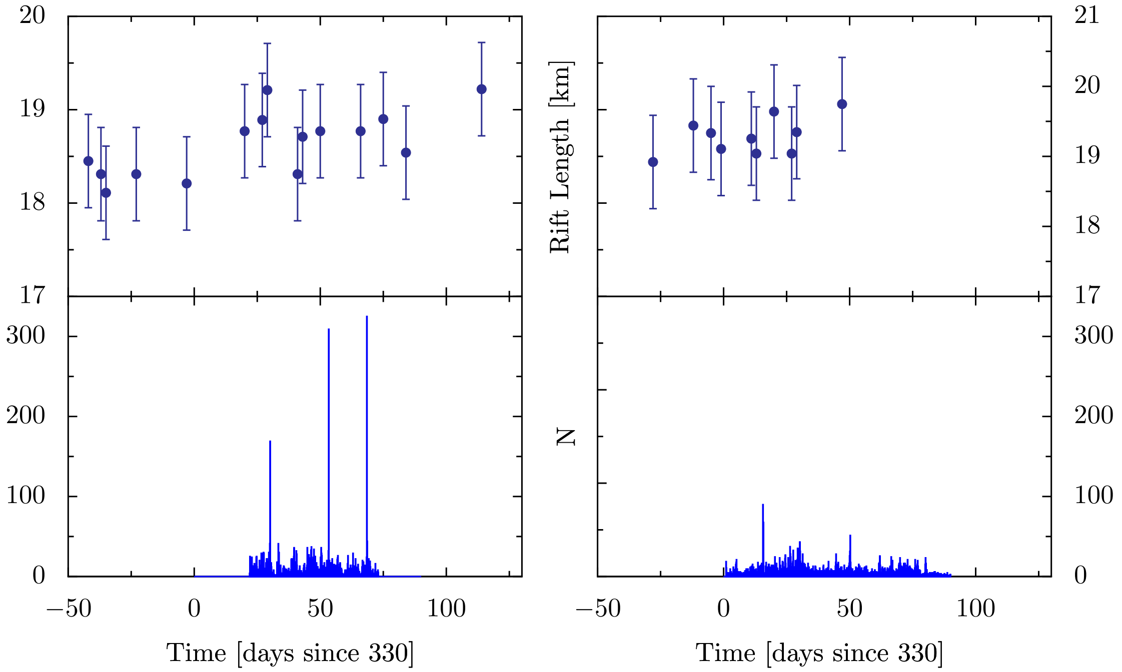

Figure 3.14: Upper panels: Zoom showing MISR derived rift lengths for T2 for each field season. Lower panels: Histogram of the seismicity for each field season.

suggests that the surface expression of each propagation event must be less than ∼500 m, the uncertainty in the MISR measurements.

The decrease in seismicity that we detect also corresponds to a period where rift T2 entered into a suture zone between two flow bands. Figure 3.15 shows a false color MISR image of T2 with the approximate location of the Fisher flowband overlaid. Suture zones tend to be rough and may contain many defects. Thus there may be a decrease in the stress concentrated ahead of the rift tip, causing a decrease in rift propagation rate. This may continue until the tip emerges from the other side. This is similar to what Fricker et al. (2005b) observed for T1. Between 2002-2003 T1 emerged through a suture zone and had a sudden spurt of growth.

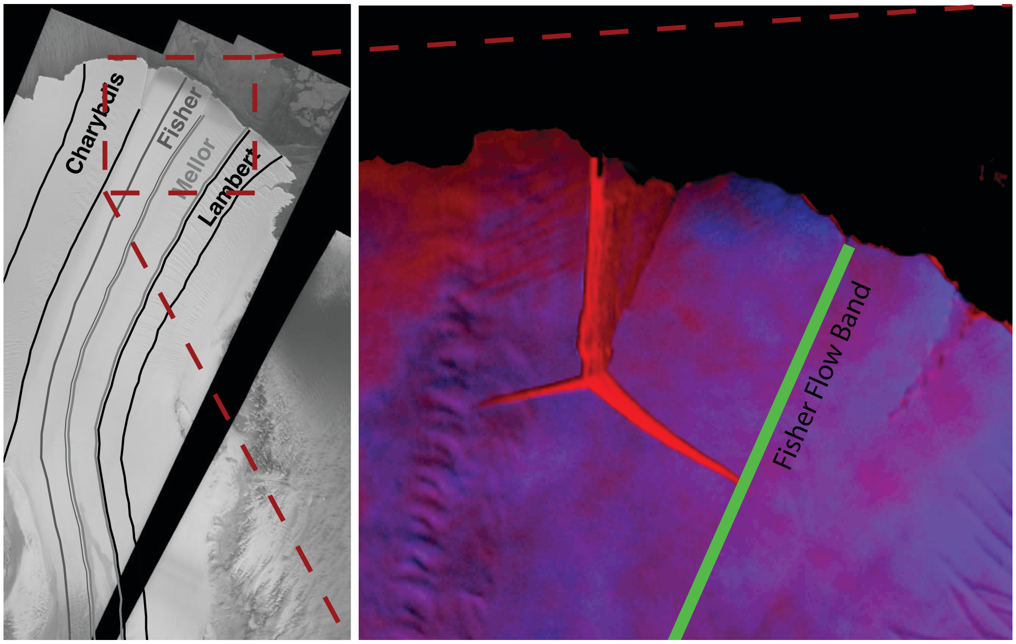

Figure 3.15: Left Panel: Map showing the major flow bands from the dominant tributaries that feed the Amery Ice Shelf, modified from (Fricker et al., 2002). Suture zones occur at the boundary where two tributaries merged upstream. Right Panel: MISR image acquired on Dec. 27, 2005 path 128. Approximate location of the western margin of the Fisher flow band has been overlaid. Easternt margin of the Fisher flow band coincides with rift L2.

3.5.2 Comparison with Other Rifts

In a parallel research effort, the University of Chicago (led by D.R. MacAyeal) has been monitoring a rift on the Ross Ice Shelf. Their deployment consisted of a single broadband seismometer close to the ice-front. The rift that they monitored, colloquially known as the "Nascent" rift, has also propagated into a suture zone. To compare seismicity between these two rifts we ran their waveform data through our detection algorithm. The results are shown in Figure 3.16. Qualitatively, we see about one swarm of seismicity on day 45 and a low rate of background seismicity (compare with Figure 3.4). A more detailed comparison of seismicity is complicated because we used our full network to discriminate against non-rift related events. There is a qualitative similarity between T2 in 2005-06 and the Nascent in 2004-05 that needs to be explored in future field seasons.

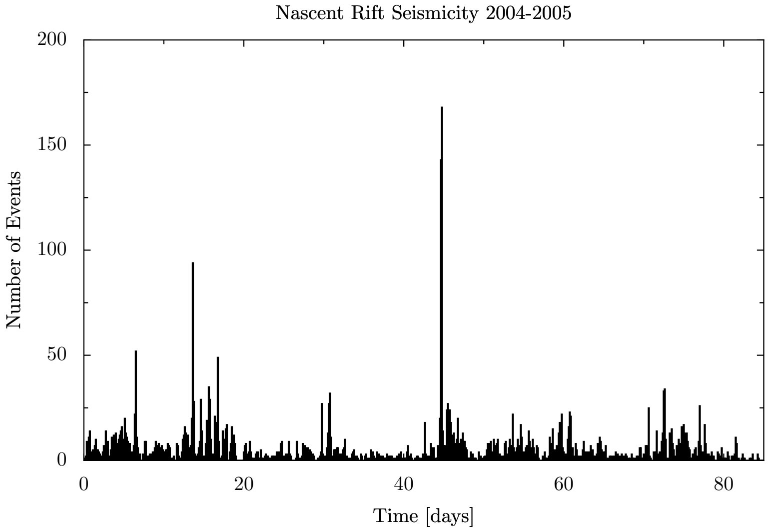

Figure 3.16: Histogram showing the number of events (bin size = 3-hr) detected near the Nascent rift on the Ross Ice Shelf using the broadband instruments deployed by the University of Chicago. The Nascent rift has also propagated into a suture zone (D.R. MacAyeal, personal communication, 2006).

3.5.3 Subcritical Rift Propagation

Given the distribution of seismic events along the rift axis, it is clear that seismicity is related to the rift propagation process. But it is not yet clear what causes the seismicity. While one likely source of icequakes is ice blocks falling into the rift from the walls, this cannot account for the seismicity near and slightly ahead of the rift tip. Another possible explanation for the episodic bursts of propagation is that the rift propagates forward by the formation of a series of micro and meso-scale cracks that extend ahead of the rift tip. As more and more of these cracks form and propagate they eventually coalesce together extending the length of the rift (Figure 3.17). Conceptually, this explains the background seismicity and swarms that we see as well as the slow (over the course of several hours) rift widening that we observe with our GPS receivers. It also follows a qualitative pattern that is quite similar to that observed in sub-critical crack growth in laboratory experiments (Atkinson and Meredith, 1987) and postulated for lithospheric rift propagation (Floyd et al., 2002). In experiments, acoustic

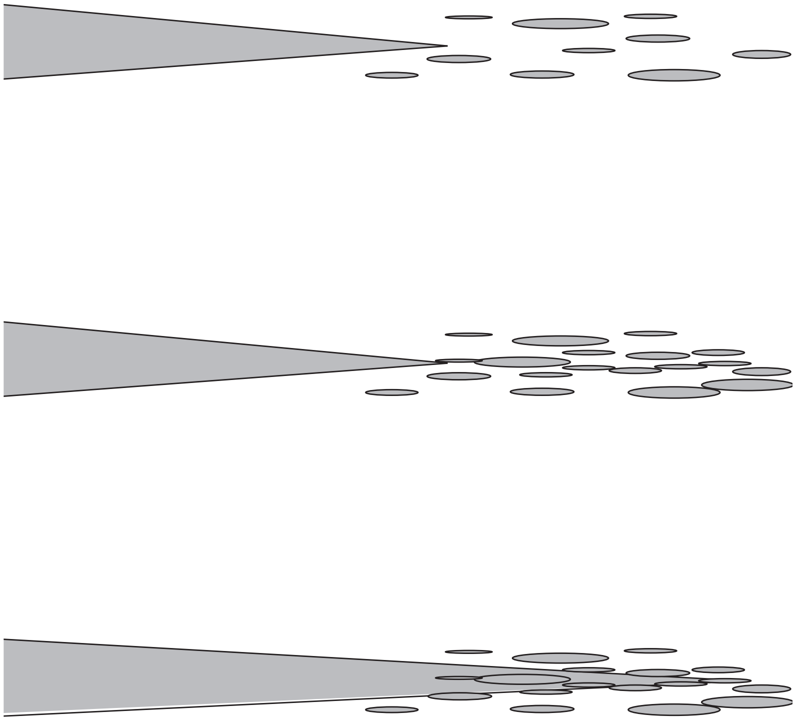

Figure 3.17: Sketch of rift propagation by micro and meso-scale crack initiation. In the first stage, a series of small and medium-sized cracks initiate around the rift tip. When the density of these cracks approaches a critical value, these smaller cracks begin to merge and create new rift surface, leading to the seismic swarms that we identified.

emissions caused by the initiation of small micro-cracks are observed to initiate over a wide region. At the beginning of the process, single isolated micro-cracks form. These micro-cracks grow and multiply resulting in an increase in the density of cracks per unit volume. Eventually, a critical crack density is reached and the micro-cracks begin to coalesce into a single main fracture. Empirical studies show that at stresses below those required to propagate a fracture critically, the velocity of crack propagation is related to the stress intensity at the crack tip by the relation

(Atkinson and Meredith, 1987):

$$\frac{dL}{dt} = CK^m \tag{3.3}$$

where C and m are positive constants, K is the stress intensity (see e.g. Lawn (1993)) and L is the crack length. Scholz (2002) combined this relationship with the stress intensity factor for a straight crack under uniform load (σ_∞):

$$K = \frac{1}{2\pi}\sqrt{L}\sigma_\infty \tag{3.4}$$

to derive a differential equation for crack length L as a function of time:

$$\frac{dL}{dt} = BL^{\frac{m}{2}} \tag{3.5}$$

where B is a separate constant that includes the rate of loading, loading geometry and proportionality in equation 3.3. If m is constant then equation 3.5 can be integrated from an initial length L_0 to give:

$$L = \left[L_0^{(2-m)/2} - (m-2)Bt/2\right]^{2/(2-p)} \tag{3.6}$$

There is an explosive singularity when the term in brackets equals zero for p greater than or equal to 2. Scholz (2002) assumed that the singularity represented the onset of rupture, and the time prior to the singularity was sub-critical crack growth. One of the predictions in Scholz (2002) is that there should be a period of accelerating rift propagation prior to major rupture events. If we consider the long-term rift propagation of rifts T1 and T2 as shown in Figure 3.13, then there may be an acceleration of T1. In contrast, T2 appears to be decelerating. This suggests that the simple model of subcritical crack growth suggested by Scholz (2002) does not apply to ice shelf rift propagation over longer periods of time. We do see some evidence of accelerating seismicity prior to the onset of swarms (Figure 3.4, upper panel). This has also been observed prior to some (but not all) earthquakes (Saleur et al., 1996) and has spawned a cottage industry devoted to explaining the origin of this signal as evidence that the state of the crust approached a critical point of a phase transition. The conceptual basis of all of these theories is very straightforward, crack-propagation is related to the interaction of many cracks of various sizes. It is necessary to consider the interaction amongst all of the cracks rather than a sole crack in isolation. This makes the problem a “many-body” problem. For a large number of interacting cracks, the appropriate methodology can be found in statistical physics. Unfortunately, little theoretical progress has been made in determining the scaling relationships for the behavior of populations of cracks from fundamental statistical properties of the populations. This is a difficult problem because analytic solutions for crack interactions only exist for a handful of situations (e.g. Broberg, 1999).

3.5.4 Statistical Models of Seismicity: Comparison with earthquakes

While detailed modeling of rift propagation from fundamental physical processes may be very difficult, an alternative prevalent in the seismological literature exists. Crack propagation is often thought of (and modeled) as a stochastic point process, rather than a deterministic process. One of the most ubiquitous features of earthquake seismicity is the power-law size-frequency distribution of earthquake magnitudes. The frequency of events with magnitudes not less than M can generally be fit with a relationship of the form:

$$\log_{10} \dot{N}(M) = A - bM \tag{3.7}$$

where A and b are constants (b is typically around 1) and M is the earthquake magnitude; $N(M)$ is the frequency of events not less than M. Qualitatively, we see many more small events than large events, consistent with equation 3.7. To analyze the distribution more quantitatively we calculated the size-frequency distribution for both season one and two separately, and then together. This is shown in Figure 3.18. We find b is relatively constant between field seasons ranging between 1.2 to 1.5, similar to the b values for earthquakes that are typically of the order of 1 (Scholz, 2002). Over the small time periods of our surveys, we do not have a large enough number of events to conclusively determine whether this distribution

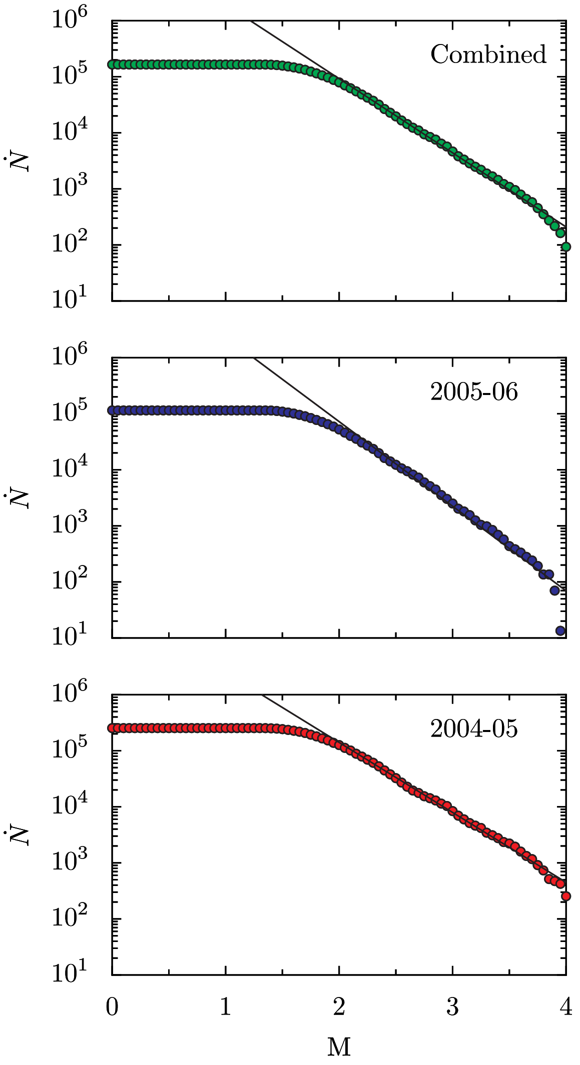

Figure 3.18: Size-frequency distribution for icequakes. M is log_{10} of the relative magnitudes of events. N is the number of events with magnitude not less than M. Upper panel shows the results when both field seasons are combined. Bottom two panels show the results for season 2 and season 1, respectively.

of events remains a power-law over a broader distribution of magnitude. Many distributions are approximately power-law over a span of a few orders of magnitude. Our results are consistent with a power-law distribution over the 2.5 orders of magnitude of event sizes that we detected. This also shows that there is not a characteristic sized event and suggests that ice shelf rift propagation may be more similar to earthquake rupture than previously thought. Another aspect of earthquakes frequently exploited is that the number of events before a "main" shock tend to increase up until the main shock (foreshocks) and then the number of events tend to decay after the main shock. The decay of aftershocks with time is often fitted with the modified Omori formula:

$$N(t) = D(t + c)^{-p} \tag{3.8}$$

Here $N(t)$ is the number of aftershocks, D, c and p are constant. Inspection of Figure 3.4 shows that events of all sizes occur during each swarm and are not accompanied by "tails" of smaller events. We also see large magnitude events that do not occur during swarms. This suggests that unlike earthquakes we do not see a classical aftershock distribution from rift related icequakes.

3.6 Conclusions

In this chapter we have confirmed our discovery in the the previous chapter that rift propagation is episodic. We see a substantial decrease in the rate of seismicity detected over the three year period that may be indicating that rift T2 is slowing down. The dense seismic network also enabled us to locate thousands of seismic events originating from the rift, providing the first detailed map of rift related seismicity. This has shown that while events cluster around the rift axis, there is also a tail of events of increasing magnitude up-rift, possibly caused by ice blocks falling into the rift from the sides. Events near the rift tip tend to be smaller in magnitude and have a higher frequency content, indicative of individual rupture events. Relative magnitudes are distributed similar to the Gutenberg-Richter law, not unlike earthquakes. The temporal behavior of the icequakes is quite different. We do not have aftershock sequences. Instead, swarms consist of a series of events of different sizes. We suggest that rift propagation occurs as a series of micro-scale and meso-scale cracks ahead of the rift tip. The swarms are the result of coalescence of these smaller cracks once a critical density is reached. An important question remains: *What causes the episodic bursts of propagation?*

It is this fundamental question that we address in Chapter 4.

Chapter 4

Forces that Drive Rift Propagation

> Facts are stubborn things; and whatever may be our wishes, our inclinations, or the dictates of our passion, they cannot alter the state of facts and evidence
>
> – John Adams

Abstract

Over the course of our three field seasons of observations, we detected seven rift propagation events with our GPS and seismometers. To determine whether the seven rift propagation events we detected were triggered by short-term environmental variables (e.g. tides, winds, ocean swell and sea-ice concentration), we compared their timing with ancillary data such as wind speeds and with tidal models. We show that neither winds nor tides are directly responsible for instantaneously triggering rift propagation. In addition, because our deployment during the 2004-05 field season coincided with the December 26th, 2004 Sumatra earthquake, we were able to evaluate the influence of both the earthquake and the associated tsunami on ice shelf rifting. We found that, although one propagation event did follow the arrival of the tsunami by several days, neither the Sumatra

Earthquake nor its tsunami instantaneously triggered rift propagation. The absence of a modulating effects from environmental variables leads us to conclude that ice shelf rift propagation is, at least on the Amery Ice Shelf, primarily driven by the internal glaciological stress of the ice shelf. To examine why environmental variables do not have a more pronounced effect on rift propagation we estimated the stress that each of each of these variables can transmit to the rift. Our calculations suggest that initially the rift is insensitive to these variables, but as the rift system matures and iceberg detachment approaches, environmental stresses may become more important in controlling rift propagation. This explains the discrepancy between our observations, that show that rift propagation is insensitive to environmental variables, and other observations, that indicate that breakup of icebergs is affected by some environmental variables.

4.1 Introduction

In the previous two chapters we demonstrated that ice shelf rift propagation is episodic. The key question left unanswered is what causes these bursts of propagation? Since rifts are exposed to both the atmosphere above and ocean below, there is a range of internal and external forces that could potentially drive rift propagation. A few of the possible variables that might influence rift propagation are sketched in Figure 4.1 and are described below.

- **Air Stress**: Katabatic winds blowing northwards along the ice shelf combined with large Antarctic storm systems can produce high wind speeds. As the winds blow across the shelf, they exert a frictional drag which, when integrated over a large enough area, could result in a substantial stress applied to the ice shelf surface. Wind induced stress is significant in some environments and is known to affect the drift tracks of icebergs and sea-ice (Wadhams, 2000).

- **Water Stress:** Sub-ice-shelf water currents, similar to atmospheric winds,

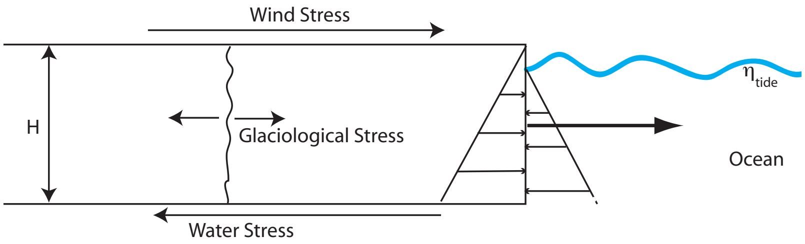

Figure 4.1: Sketch illustrating some of the forces that may drive rift propagation. Frictional drag from ocean currents and wind stress may drive rift propagation. In addition, internal glaciological stress caused by gravitational spreading of the ice shelf may also drive propagation. Tides may also contribute to rift propagation by bending the ice shelf.

can exert a drag force on the base of the ice. If there are large ridges underneath the shelf, these could act like keels, magnifying the effect of ocean currents.

- **Ocean tides:** Ocean tides can cause the ice to flex, leading to bending stresses that might cause fracture. These “tide cracks” have been observed on a variety of glaciers but they primarily exist near regions where the ice is transitioning from grounded to floating (e.g. Debenham, 1965).
- **Ocean Swell and Sea Ice:** Storm surges and ocean swell could induce flexural-gravity waves - a type of vibration that has been observed in sea ice hundreds of kilometers within the pack-ice (Wadhams, 2000). Some theories have postulated that flexural-gravity waves may trigger iceberg calving events (Holdsworth and Glynn, 1981).
- **Internal Stress:** The internal stress within the ice shelf, caused by gravity, is responsible for ice shelf spreading and may provide the stress necessary to drive rift propagation (Bassis et al., 2005; Joughin et al., 2004b).

Given the number of forces that may be involved, a crucial first step in improving our knowledge of iceberg calving is identifying those forces that are not directly responsible for driving rift propagation. In this chapter we combine our observations of rift propagation events with automatic weather stations (AWS), tide gauges operated by the Australian Antarctic Division and tidal models to identify the role of environmental stresses in driving rift propagation. Serendipitously, our instruments were deployed several weeks prior to the Great Sumatra Earthquake that occurred on December 26th, 2004. We recorded waveforms from the earthquake with our seismometers as well as signals from the tsunami the earthquake generated with our GPS.

To complicate the situation, rifts are always filled with an inhomogeneous mixture of ice and snow debris containing ice blocks that have fallen in from rift walls, sea ice, marine ice and accumulated snow. It has been speculated that this debris (often termed mélange) is mechanically competent and may glue the rift walls, providing a resistive stress that prevents propagation (MacAyeal et al., 1998; Hulbe et al., 1998; Rignot and MacAyeal, 1998). In an alternative model, it has been suggested that "wedging" forces, caused by ice blocks falling into the rift, could drive propagation (Bassis et al., 2005, Chapter 2).

We use the term "iceberg detachment" to indicate the process whereby multiple rifts intersect to isolate an iceberg. We do not use iceberg detachment in the sense of a discrete instance in time because it is unclear how to define, and more importantly measure, the exact moment in time when an iceberg ceases to be attached to its parent ice shelf. Instead, in our terminology iceberg detachment occurs over a finite interval of time. Our definition of iceberg detachment differs from how we use rift propagation in that, in our terminology, rift propagation refers to the propagation of a single rift while iceberg detachment refers to a rift system. We also continue the convention adopted in the previous chapter of referring to the 2002-03 field season as "season 1", the 2004-05 field season as "season 2" and the 2005-06 field season as "season 3", and continue the convention whereby swarms are numbered 1 through 7.

4.2 Results

To decide whether environmental variables are important in triggering rift propagation events we compared the timing of the seven episodic propagation events with:

- Wind speeds (measured with a nearby AWS)
- Tidal amplitudes (computed using the CATS tidal model (Padman et al., 2002))
- Sea-ice concentration and extent (determined while we were in the field and with satellite images)
- Arrival of the Sumatra earthquake and tsunami that followed (detected with our seismometer, GPS and tide gauges from nearby Antarctic bases)

The effect of each of these variables is discussed separately below.

4.2.1 Winds Speeds and Tidal Amplitudes

Figures 4.2 through 4.4 show the seismicity, wind speeds and tidal amplitudes for seasons 1, 2 and 3, respectively. Inspection of Figure 4.2 shows that two of the propagation events (swarms 2 and 3) of season 1 were preceded by periods of severe winds. However, this trend does not continue in subsequent field seasons. In particular, during season 2 none of the swarms were preceded by severe winds suggesting that the connection between wind speeds and propagation events may be coincidental. It is also apparent from Figures 4.2 through 4.4 that rift propagation events do not occur exclusively during periods when the tidal amplitudes are at their highest or lowest values. For instance, swarm 4, during season 2 (2004-05), occurs at a time when the tidal amplitude is close to zero. Rift propagation events occur at a variety of tidal phases, tidal amplitudes and wind speeds, indicating that neither of these variables are solely responsible for triggering rift propagation.

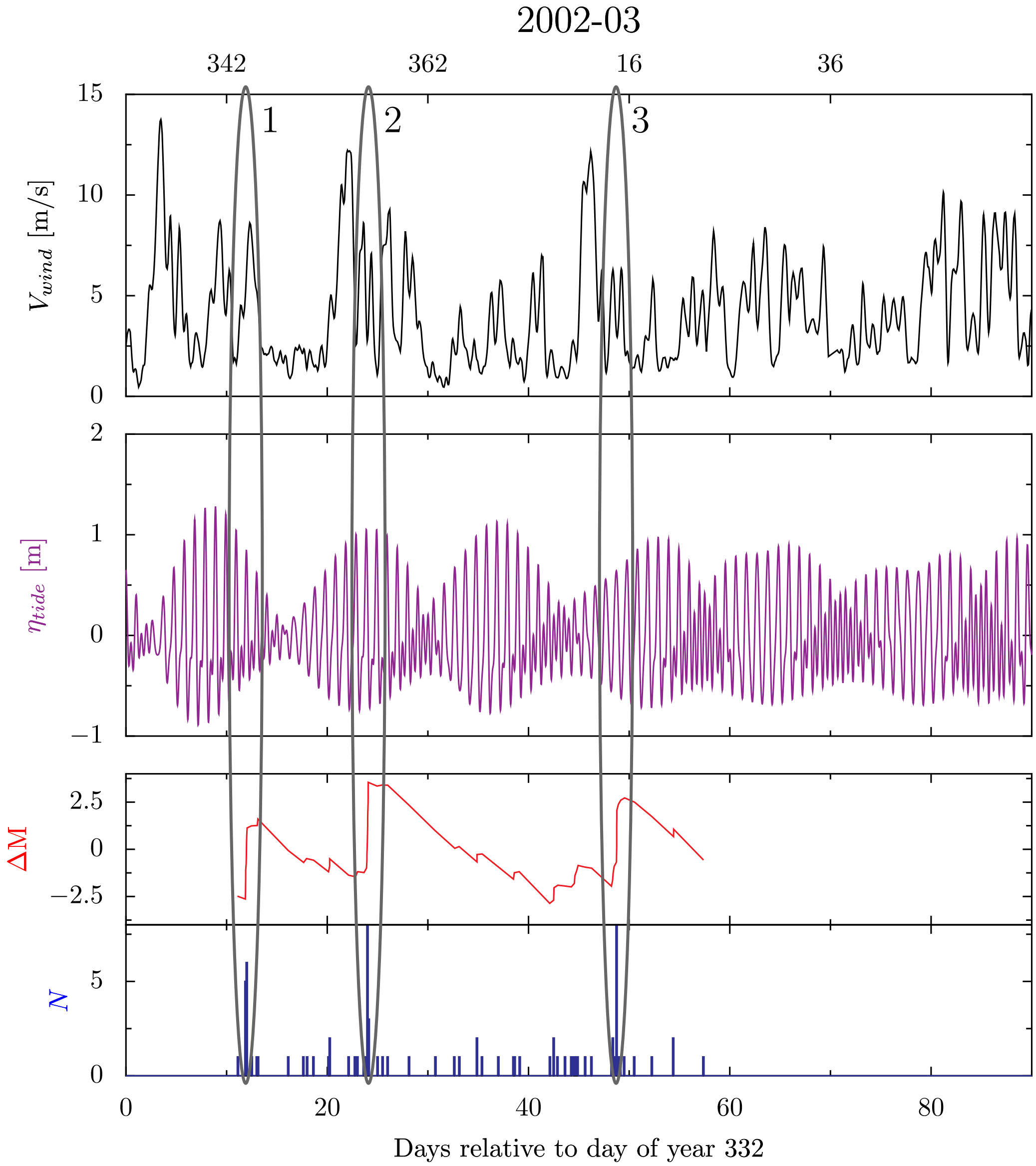

Figure 4.2: Comparison of amplitudes of winds and tides with the timing of seismic swarms for the 2002-03 field season. Upper panel: Wind speeds measured at AWS stations on the Amery Ice Shelf. Middle panel: Tidal amplitudes computed from the CATS tidal model (Padman et al., 2002). Lower two panels: De-trended cumulative seismicity, ΔM shown with a histogram of the seismicity (bin size = 3 hours) N is the number of events per bin. Time is relative to day of year 332.

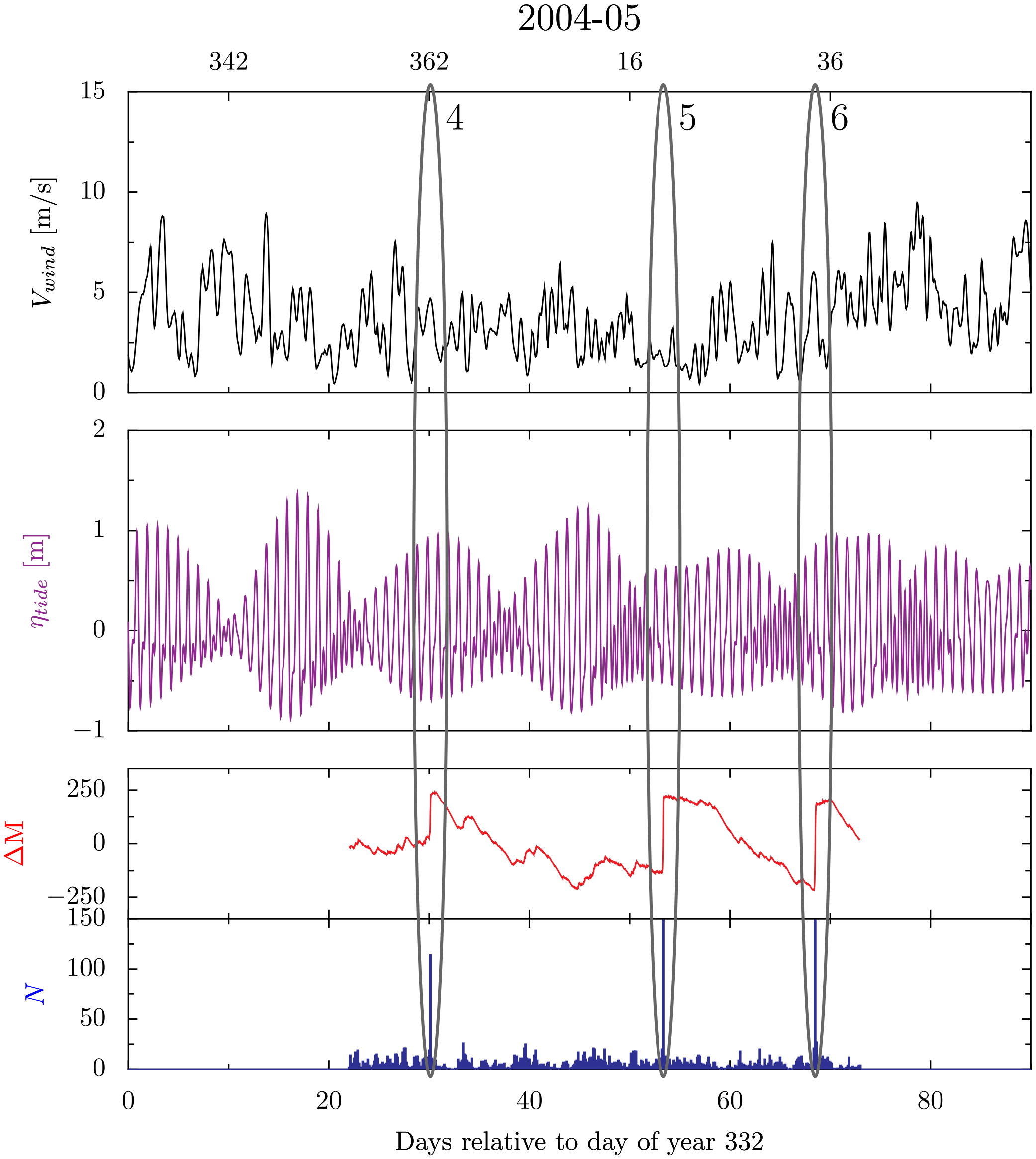

Figure 4.3: Comparison of amplitudes of winds and tides with the timing of seismic swarms for the 2004-05 field season. Upper panel: Wind speeds measured at AWS stations on the Amery Ice Shelf. Middle panel: Tidal amplitudes computed from the CATS tidal model (Padman et al., 2002). Lower two panels: De-trended cumulative seismicity, ΔM shown with a histogram of the seismicity (bin size = 3 hours) N is the number of events per bin. Time is relative to day of year 332.

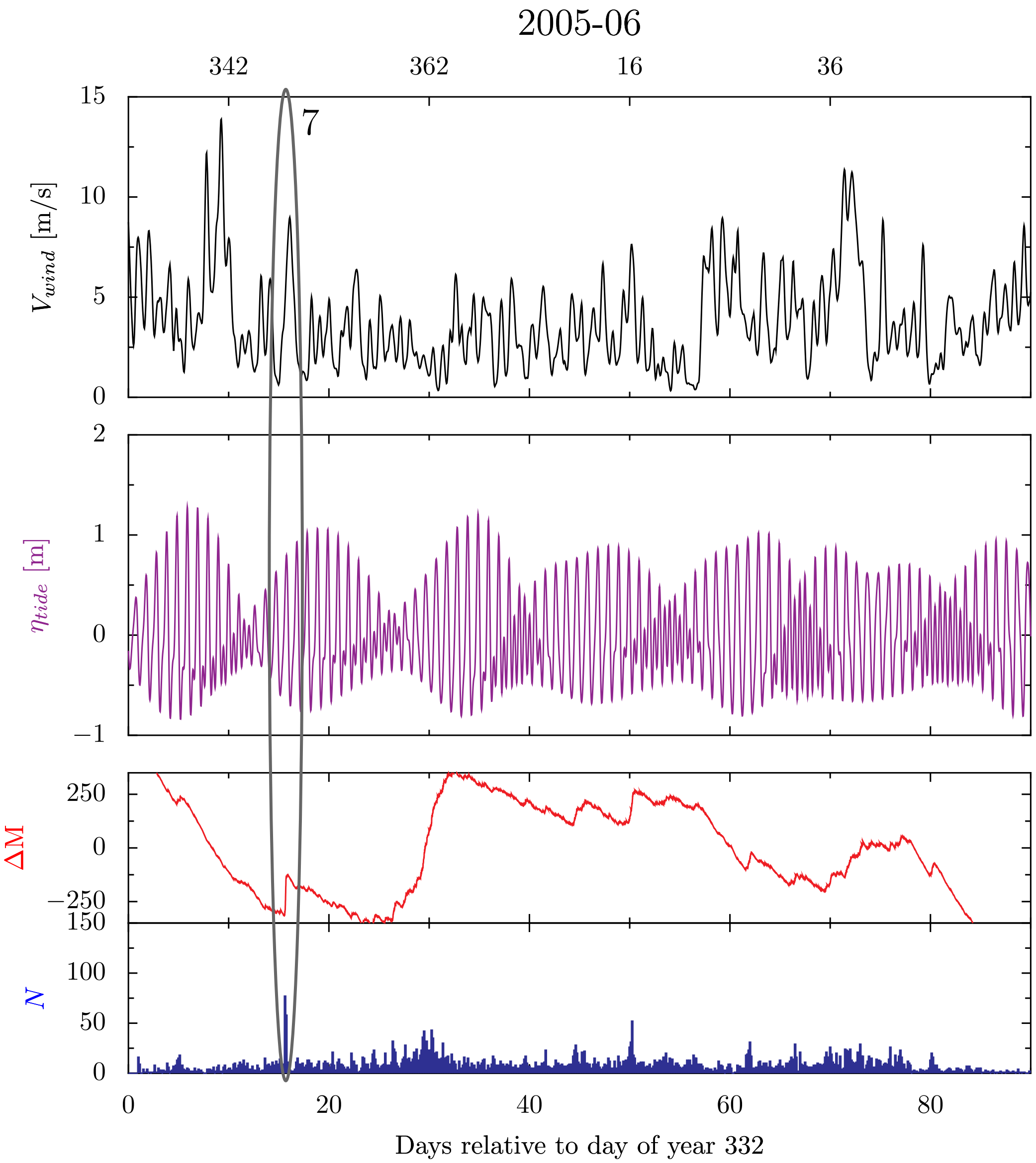

Figure 4.4: Comparison of amplitudes of winds and tides with the timing of seismic swarms for the 2005-06 field season. Upper panel: Wind speeds measured at AWS stations on the Amery Ice Shelf. Middle panel: Tidal amplitudes computed from the CATS tidal model (Padman et al., 2002). Lower two panels: De-trended cumulative seismicity, ΔM shown with a histogram of the seismicity (bin size = 3 hours) N is the number of events per bin. Time is relative to day of year 332.

It is also possible that a combination of severe winds and high tidal amplitudes is necessary to trigger propagation. To investigate this possibility we looked at the combination of tides and wind speeds during each swarm. Wind speeds and tidal amplitudes were determined using the median value over a three-hour period surrounding the onset of each swarm. Using either shorter or longer intervals did not produce significantly different results. We also tried using the mean and maximum value of the wind speed. These changes only altered the magnitude, but not the general pattern of relative wind speeds. Because the tidal amplitudes are such smoothly varying functions of time, changing the averaging interval had even less effect on the values determined.

Figure 4.5 shows tidal amplitudes (upper left panel), wind speeds (upper right panel) and both wind speeds and tidal amplitudes (lower panel) determined for each swarm during seasons 1 through 3. Similar to what we determined before, there is no trend in either wind speed or tidal amplitude that would indicate either of these variables are involved in triggering rift propagation events. Looking at the combination of tidal amplitudes and wind speeds (Figure 4.5, lower panel), we would expect that if elevated tides and severe winds are necessary to trigger propagation events, points would cluster along the upper right-hand side of the plot. Instead, events are scattered with little pattern throughout the plot area. This indicates that even the combined effect of tides and winds is not sufficient to trigger rift propagation. A further possibility is that wind speeds need to be integrated over some characteristic time period. We tried integrating wind speeds over periods of 1, 2 and 5 days but still found no connection between integrated wind speeds and propagation events. It is possible that the swarms are triggered by high tides and/or winds but only in a stochastic sense. If this were the case, increased winds should be associated with an increase in probability of a rupture event. This would imply that, on average, rift propagation rates should be faster during the winter, when wind speeds are greatest. However, analysis of rift lengths using satellite imagery shows that this is opposite to what is observed (Fricker et al.,

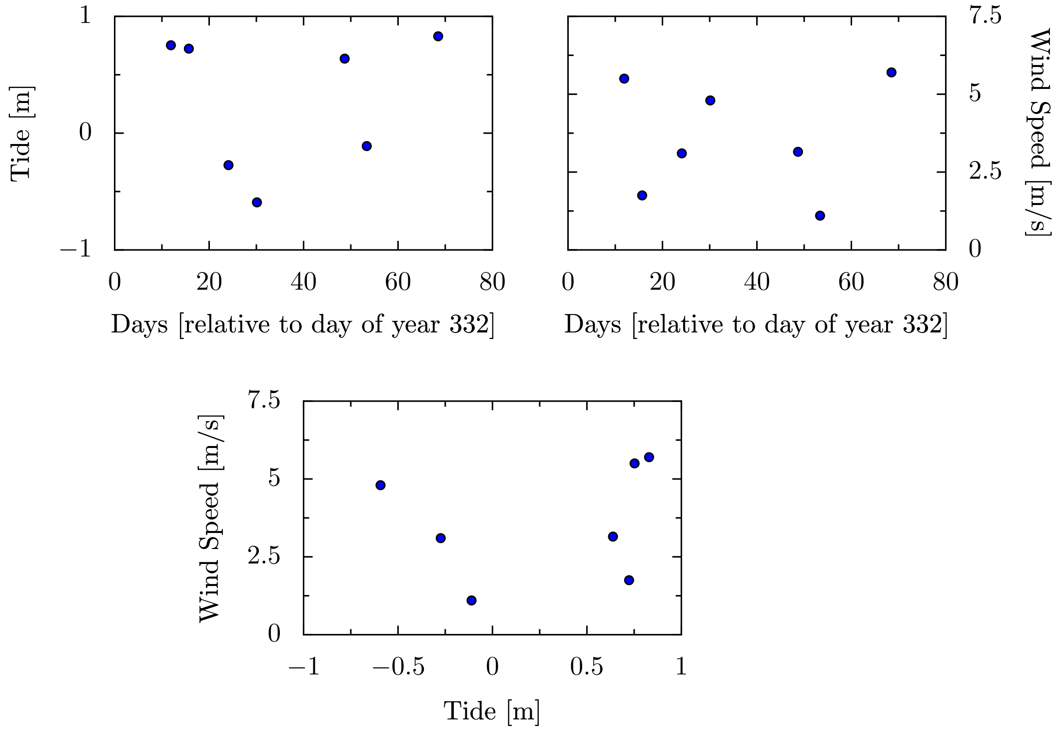

Figure 4.5: Figure illustrating the possible triggers for rift propagation for all three field seasons. Upper left: tidal amplitude determined from the CATS model (Padman et al., 2002) for each propagation event. Upper right: Wind speed determined from AWS site G3 for each propagation event. Lower panel: Wind speed versus tidal amplitude for all seven propagation events. Both wind speed and tidal amplitude were obtained from 3-hour average over the duration of the swarm.

2005b). These authors determined that the rift actually propagates faster in the summer, when wind speeds are at their lowest. This makes it unlikely that either winds or tides are the primary variables driving rift propagation.

4.2.2 Ocean Swell and Sea Ice

We have no direct measurements or models of ocean swell. Radar altimetry does provide estimates of significant-wave-heights in the Southern Ocean but the long time between successive measurements (weeks) makes it impossible to directly determine whether each propagation event coincided with a large swell event. For this reason, it is more difficult to compare the timing of rupture events with the timing of ocean swell events. It has been suspected for some time that ice-ocean coupled flexural-gravity waves might cause icebergs to disintegrate (Goodman et al., 1980; MacAyeal et al., 2006). While no large storms occurred during any of our field measurements, MacAyeal et al. (2006) have shown that swell generated in the North Atlantic can cause significant micro-seisms within the ice shelf, detectable with broadband seismometers. Unlike the broadband seismometer used by MacAyeal et al. (2006), our high-frequency instruments were not able to measure ocean swell. Nevertheless, because the presence of sea-ice in front of the ice shelf will attenuate the amplitude of swell that penetrates to the ice shelf, the presence of sea-ice in front of the ice shelf may be an appropriate proxy to gauge how important swell is in triggering rift propagation. This is consistent with the trend in ocean swell-induced micro-seisms detected by MacAyeal et al. (2006). These authors observed a substantial increase in the power of swell induced oscillations after the sea-ice broke out in front of the Ross Ice Shelf. This observation suggests that a simple test of whether large ocean swell is triggering rift propagation is to see whether the rift propagates faster during periods when there is little sea-ice cover in front of the Amery Ice Shelf. Satellite imagery does show that the rift propagates faster during the Austral summer than over the winter season (Fricker et al., 2005b), but these authors also found that propagation rates start to increase between September and October. Analysis of MODIS images of the region shows that the front of the Amery Ice Shelf is rarely sea-ice free before December, implying that propagation rates actually increase during a period when there is substantial sea-ice cover. This analysis suggests that swell induced vibrations and bending are not the primary drivers of rift propagation, consistent with our field data. We found that 4 of the 6 swarms (swarms 1, 2, 4 and 7) occurred while there was still sea-ice in front of the ice shelf. As a final test we ran the seismic data from the single seismometer operated by MacAyeal et al. (2006) near the “Nascent” rift on the Ross Ice Shelf through our event detection algorithm (Chapter 3). We found no swarms during periods when they observed large ocean swell on the ice shelf. While large storms and their associated swell may occasionally trigger pre-existing rifts very close to the ice front to propagate, it does not appear likely that ocean swell is the primary factor that drives ice shelf rift propagation.

4.2.3 The Sumatra Earthquake and Tsunami

Figure 4.6 shows the tide gauge record from Davis station along with the seismicity we detected. The arrival of the tsunami (marked with an arrow) is clearly seen in the tide gauge data. We did not notice an increase in the frequency of icequakes following the arrival of the earthquake, or any of its aftershocks, implying that vibrations from the earthquake did not affect rift propagation. Small amplitude, high-frequency vibrations, not surprisingly, do not appear to trigger rift propagation. We also looked to see whether the tsunami that the earthquake generated might have triggered a rift propagation event. Figure 4.6 shows that swarm 4 occurred about one day after the arrival of the tsunami. In addition, it is evident that the combination of high tide and oscillations from tsunami also did not immediately trigger a rift propagation events. The connection between the rift propagation event and the tsunami is intriguing, but it is not clear that there is a causal relation between the two events. Given the lack of influence between either tides and winds and propagation events we think it is unlikely that tsunami triggered the propagation event. Instead, it is more probable that the conjunction between the two is coincidental.

4.3 Discussion

4.3.1 Implications

Our analysis suggests that episodic bursts of rifts propagation are not directly related to tidal amplitude, tidal phase, wind speed or ocean swell, suggesting that rift propagation is insensitive to a broad range of loading rates (summarized

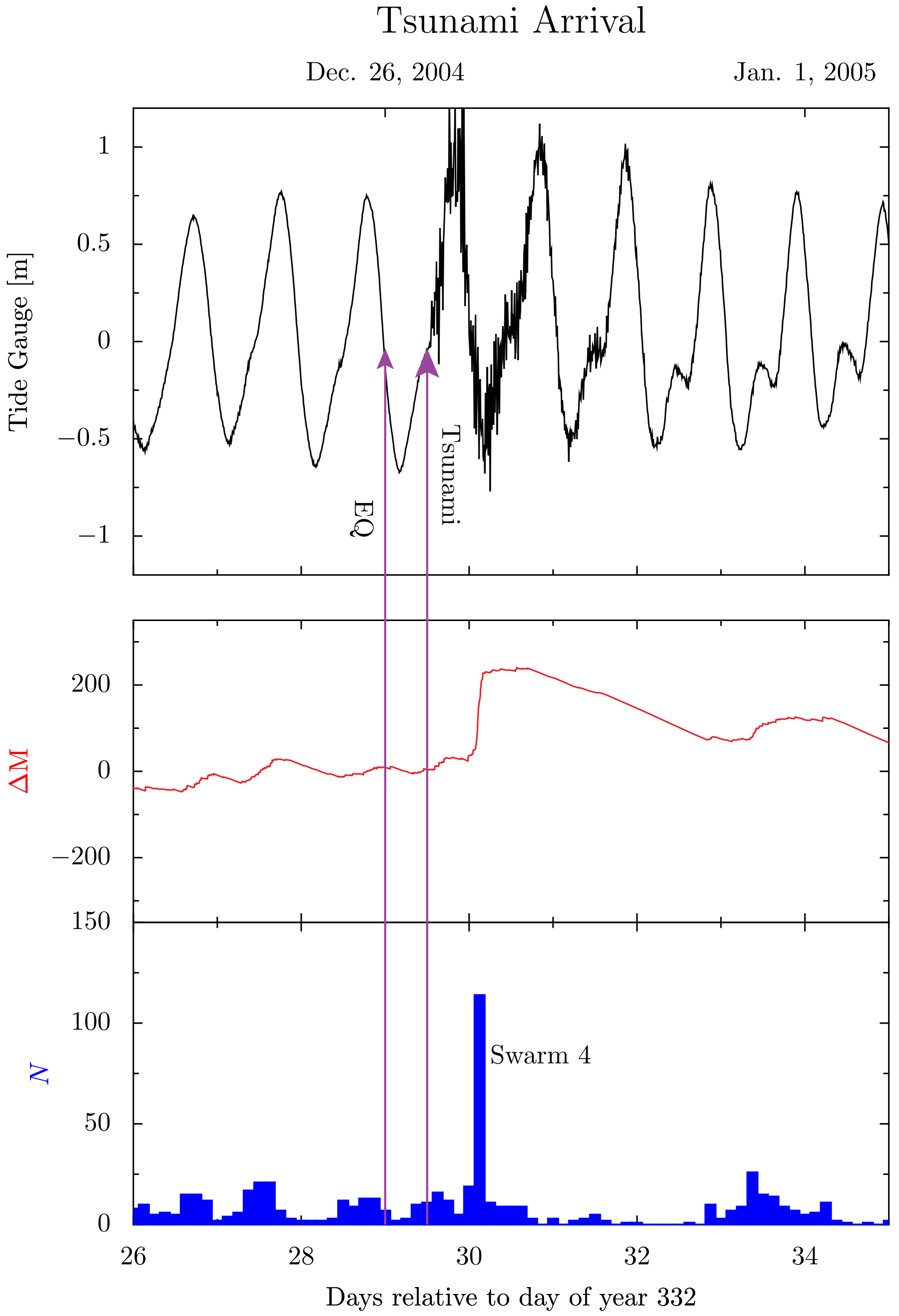

Figure 4.6: Upper panel: Tide gauge from Davis station showing the arrival of the tsunami, shown with an arrow. Lower two panels: Histogram showing the number of events in three hour bins (N) and detrended cumulative magnitude of the seismicity (ΔM). The arrival of the Sumatra Earthquake (EQ) is also indicated with an arrow.

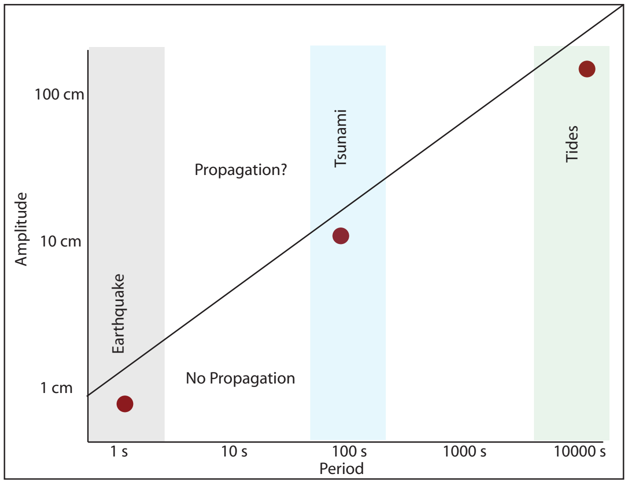

Figure 4.7: Range in loading rates observed for the Amery Ice Shelf. At typical amplitudes, none of the environmental variables considered have been sufficient to trigger propagation on their own. The black line separates the state space into two regions. In the lower region, our observations have demonstrated that these amplitudes and periods do not trigger rift propagation. The region above the black line is the part of the state space where we do not know if environmental variables with those amplitudes and periods will be sufficient to trigger rift propagation.

in Figure 4.7). While our observations do not conclusively say what does drive rift propagation, we do see that rift propagation appears to be insensitive to periods ranging from one second with sub-centimeter amplitude (the earthquake) to periods longer than ten thousand seconds with amplitudes on the order of one meter (tides). The lack of a tidally driven signal is surprising given recent studies that implicate tides in triggering stick-slip motion of the ice hundreds of kilometers upstream from the grounding zone (Bindschadler et al., 2003). Moreover, iceberg drift is known to be controlled by wind stress and water stress (as well as Coriolis forces) (Wadhams, 2000). It is surprising that these forces are significant for iceberg drift but unimportant in driving rift propagation. One possibility is that at an early stage of development, rift propagation is dominated by the internal stress of the ice shelf. At a later stage, as the rift system matures and the proto-berg approaches complete detachment, it becomes less and less coupled to the main ice shelf and environmental variables become increasingly important.

4.3.2 Force Balance

To examine why environmental factors do not have a significant effect on rift propagation we consider the relative magnitude of all of the forces acting on the ice shelf. Performing a force balance on a unit area of the ice shelf we find (see e.g. Wadhams, 2000):

$$\rho_i a = \tau_a + \tau_w + \tau_c + \tau_i + \tau_{bend} \tag{4.1}$$

τ_a is the air stress exerted on the ice shelf by the winds; τ_w is the water stress caused by ocean currents on the bottom of the ice shelf; τ_c is the Coriolis Force; τ_i is the internal glaciological stress of the ice and τ_{bend} is the bending stress of the ice caused by tides and ocean swell; ρ_i is the density of ice and a is the acceleration. Once the iceberg completely detaches and drifts freely, inertial terms may be significant. However, our interest is in the period prior to detachment when inertial terms can be neglected because of the small velocity of ice. To estimate the contribution of each of these terms to the driving stress, we need to calculate the magnitude of each of the terms in equation 4.1. For comparison the internal glaciological stress, inferred from the strain rates we measured, is on the order of 200-400 kPa.

Coriolis Force

The Coriolis force arises due to the rotation of the Earth. Therefore, measurements made relative to the surface of the Earth are not in an inertial reference frame. Although the Coriolis force is important in determining trajectories for sea ice and iceberg drift (Wadhams, 2000), typical ice shelf velocities are small ($\sim 10^{-5}$ m/s) and therefore the Coriolis force is also usually quite small. Quantitatively, the Coriolis force is given by (Wadhams, 2000):

$$\tau_c = \rho_i H_i U f \tag{4.2}$$

Where H_i is the ice thickness; U is the velocity of ice and f is the Coriolis parameter:

$$f = 2\Omega \sin \phi. \tag{4.3}$$

In equation 4.3, Ω is the rate of angular rotation of the Earth and ϕ is the latitude. For an ice flow velocity of 4 m/day ($\sim 5 \times 10^{-5}$ m/s), H_i 400 m, ice density of 920 kg/m^3 and f on the order 10^{-5} s^{-1}. This results in τ_c on the order of 10^{-3} kPa. This is small compared to the glaciological stress (of the order of several hundred kPa) suggesting that until the iceberg actually starts to drift, the Coriolis force is a negligible term in the force-balance.

Sea Surface Tilt

Sea surface tilt arises because the sea surface does not exactly correspond to an equipotential surface. The difference between the two surfaces induces a pressure gradient in the water column. For sea ice, it is found that the sea surface tilt is important over long periods of time (weeks to months), but is insignificant over shorter periods of time (days) (Wadhams, 2000). The sea surface tilt is given by the expression:

$$\tau_t = -\rho_i g H_i \nabla \eta_{sea} \tag{4.4}$$

For typical sea surface slopes of $10^{-3} - 10^{-4}$ this results in a sea surface tilt stress of $\tau_t = 0.1 - 1$ kPa. Again, this is small compared to the glaciological stress of ice and not likely to be important in driving rift propagation.

Air Stress

Observations show that the wind exerts a frictional force on the surface of the ice that is proportional to the square of the wind speed (Wadhams, 2000)

$$\tau_a = C_a \rho_a U_a^2 \tag{4.5}$$

where ρ_a is the density of air ($\sim 1\ kg/m^3$), U_a is the wind speed ($\sim$50 m/s) and C_a is the drag factor. The drag coefficient is an empirical constant that depends on the roughness of the ice. It is occasionally separated into a “form” drag that depends on larger scale topography and roughness of the ice and a “skin” drag that is approximately constant. For most applications the drag (combination of form and skin) can range in value from $10^{-2} - 10^{-3}$, where the upper values of the order of 10^{-2} would involve considerable large scale roughness. Typical magnitudes of wind speeds deduced from an AWS near the Amery Ice Shelf are in the range of several meters per second to tens of meters per second, resulting in a typical stress of $\tau_a \sim 1 - 20 \times 10^{-3}$ kPa. This stress is relatively small, but if integrated over a large surface area could become significant. Wind stress far upstream of the rift is unlikely to have any effect on the rift propagation. Therefore, a reasonable estimate for the maximum stress that the wind can apply to the rift system is to integrate the wind stress over the area of the proto-berg (A_{berg}) enclosed by the rift system:

$$F_a = C_a \rho_a U_a^2 A_{berg} \tag{4.6}$$

We then assume that the stress is concentrated along the strip of length L and ice thickness H that connects the berg to the rest of the ice shelf:

$$\tau_a^{max} = \frac{C_a \rho_a U_a^2 A_{berg}}{H_i L} \tag{4.7}$$

Equation 4.7 implies that larger icebergs may be more sensitive to wind stress than smaller bergs and that as the proto-berg continues to detach and L decreases, the effect of wind stress will become increasingly important. For the Loose-Tooth, the area of the rift system is about 900 km^2 and the length of the strip of material that connects T2 with L2 is still several kilometers long. Assuming L 4 km and ice thickness, H_i of 400 m. This results in a maximum wind stress on the order of 10-20 kPa. This is still relatively small compared to the glaciological stress but is getting closer. For example, if the length L were to decrease to 1 km then τ_a would be about 60 kPa, which is comparable in magnitude to the internal glaciological stress of the ice shelf. We expect winds to have an increasingly large effect as the Loose Tooth approaches complete detachment. Our calculations suggest that air stress may be more important for mature rift systems and for icebergs with a larger surface area.

Water Stress

The effect of water stress is similar to that of wind stress, with a quadratic dependency on water current speed (Wadhams, 2000):

$$\tau_w = C_w \rho_w U_w^2 \tag{4.8}$$

We denote the drag coefficient for water by C_w; ρ_w is the density of water and U_w is the current speed. Typical values for the drag coefficient for water are again of the order of $10^{-2} - 10^{-1}$. Ocean current speeds are on the order of 1-10 cm/s and the density of water is approximately 1000 kg/m^3. This implies that water stress is about one order of magnitude smaller than air stress (typically 1-2 kPa). Because of the sub-surface topography of the rift, the form drag may be substantially higher than normally observed. With an increase in drag coefficient of one order of magnitude, water stresses could potentially have the same magnitude as wind stress. Again, if we assume that water drag is integrated over the proto-berg area and that force is concentrated along the band of material that connects the proto-berg to its parent ice shelf, this force can become significant. Qualitatively, we find the same result that we found for wind stress: water stress will affect larger bergs more and the effect will become more pronounced as the iceberg approaches detachment. Unless there is a significant form drag caused by subsurface topography, we expect that wind stress will be more important than water stress.

Tidal Bending

In addition to sub-shelf currents, tides also induce vertical motion of the ice. Because the time scale of tidal variations is relatively short, we can approximate the deformation of ice as a quasi-static elastic response. To estimate the magnitude of bending stresses, we assume the ice can be treated quasi-statically using the elastic flexural wave equation (Turcotte and Schubert, 2002):

$$D\frac{d^4w}{dx^4} + \rho_w g(w - \eta_{tide}) = 0 \tag{4.9}$$

where w is the displacement of the beam, η_{tide} is the tidal amplitude. D is the flexural rigidity of ice given by:

$$D = \frac{EH_i^3}{12(1-\nu^2)} \tag{4.10}$$

E and ν are Young's modulus and Poisson's ratio for ice, respectively. For convenience we also introduce the length scale:

$$\alpha = \left(\frac{4D}{\rho_w g}\right)^{\frac{1}{4}} \tag{4.11}$$

Where α is often called the flexural wavelength. To calculate the bending stress from the tides, we assume a quasi-static sinusoidal tidal displacement with wavelength $\lambda = \frac{2\pi}{k}$:

$$\eta_{tide} = A_0 e^{ikx} \tag{4.12}$$

We can find a solution to equation 4.9 by assuming a solution of the form:

$$w = w_0 e^{ikx} \tag{4.13}$$

Substituting equation 4.13 and equation 4.12 into equation 4.9 we find the solution for the displacement:

$$w = \frac{A_0}{(1+\alpha^4 k^4)} e^{ikx} \tag{4.14}$$

Equation 4.14 implies that wavelengths large compared to the flexural wavelength are locally isostatically compensated while those that are small compared to the flexural wavelength induce no bending. The stress induced by flexure is related to the displacement by (Turcotte and Schubert, 2002):

$$\tau_{bend} = -\frac{EH_i}{2(1-\nu^2)} \frac{d^2 w}{dx^2} \tag{4.15}$$

The maximum bending stress occurs either at the top or bottom of the ice shelf (depending on the sign of the tide). Substituting equation 4.14 into equation 4.15 we find:

$$\tau_{bend}^{max} = \frac{EH_i}{2(1-\nu^2)} \frac{A_0 k^2}{(1+\alpha^4 k^4)} \tag{4.16}$$

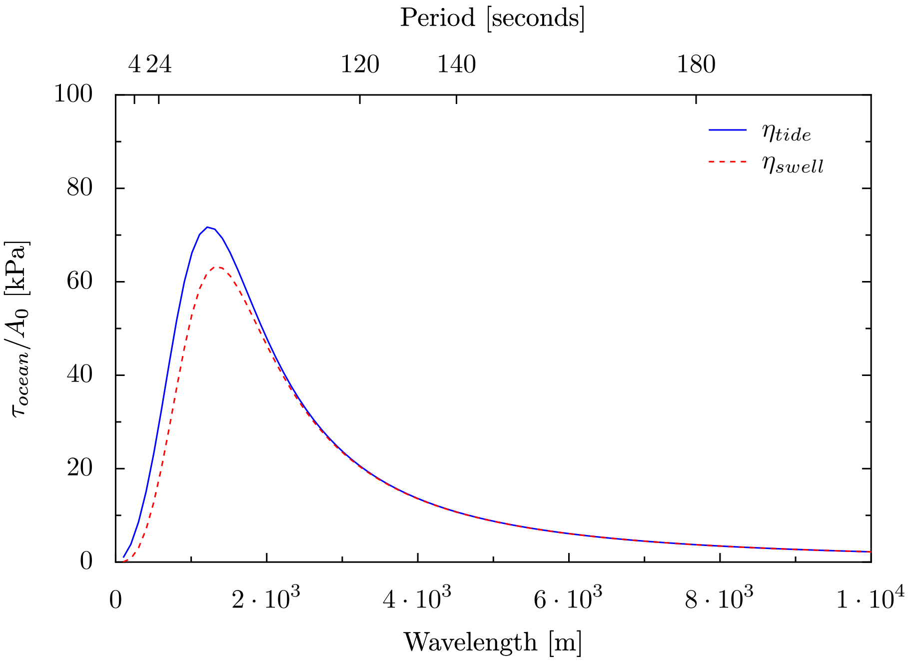

Figure 4.8: Maximum bending stress as a function of fraction of flexural wavelength for tides (blue line) and swell (dashed red line). Values have been normalized per unit amplitude. Tides typically have a wavelength of 50-100 km, which is 80 times the flexural wavelength of ice. This results in negligible bending stress. The associated period of the flexural gravity waves is shown along the top. Flexural bending stresses can be significant, especially for large amplitude swell. However, the amplitude will attenuate exponentially with distance into the ice shelf.

where we have omitted the $\exp(ikx)$ modulation of the magnitude. Figure 4.8 (blue line) shows the bending stress normalized by unit tidal amplitude. Tides typically have wavelengths of 50-100 km, approximately 80 times the flexural wavelength of ice. This yields a bending stress of about 0.05-0.1 kPa. The mismatch between the flexural wavelength and the tidal wavelength results in a very low bending stress. We see that for wavelengths comparable to the flexural wavelength (i.e. on the order of 1 km) bending can induce a significant stress within the ice. While the wavelengths of tides are too long, ocean swell does have wavelengths within this range.

Ocean Swell

In contrast to ocean tides where the wavelength was found to be very much larger than the flexural wavelength, ocean swell does have wavelengths that are more comparable to the flexural wavelength of ice. This raises the question of whether ocean swell alone is sufficient to trigger rift propagation. Calculating the stress due to ocean swell is more complicated than for tides. The problem has received considerable attention in the sea-ice community in order to understand the impact of ocean swell on breakup of ice in the marginal zone (Goodman et al., 1980; Wadhams, 1986; Squire et al., 1995; Meylan et al., 1997). Following Wadhams (1986) we assume that an incoming plane wave of amplitude A, wavenumber k and period $T = \frac{2\pi}{\omega}$ is directly incident on the ice front. Including the frequency dependence, the flexural equation then becomes:

$$D\frac{d^4}{dx^4}w + (\rho_w g - \rho_i H_i \omega^2)w = A\rho_w g e^{ikx} \tag{4.17}$$

See (Goodman et al., 1980) or (Wadhams, 1986) for a complete derivation of equation 4.17. The only difference between the quasi-static approach used in modeling the effects of the tides is a frequency dependent term $\rho_i H\omega^2$. In the limit that ω approaches zero (infinite period), we recover equation 4.9. The amplitude A of the wave is the amplitude of particle motion at the bottom of the ice shelf, not at the sea surface. Because this decreases exponentially with depth, the amplitude of the wave on the bottom of the ice shelf will be related to surface amplitude by:

$$A = A_0 \exp^{(-kH_i\rho_i/\rho_w)} \tag{4.18}$$

Swell will have an increasingly small effect on ice shelves of large thickness compared with those that are thinner. Detailed numerical solutions can be found for equation 4.17 using a variety of numerical methods. Since we are only interested in estimating the order of magnitude of bending stresses induced by swell we adopt a simpler approach that sidesteps most of the complications. In addition to the flexural wavelength, we introduce another length scale related to the frequency of the swell and the ice thickness:

$$\beta = \left(\frac{4D}{\rho_i H_i \omega^2}\right)^4 \tag{4.19}$$

Similar to our approach for tides, we substitute a solution of the form:

$$w = w_0 e^{ikx} \tag{4.20}$$

into equation 4.17. This leads to the solution:

$$w = A\frac{\rho_w g}{k^4 + (\frac{1}{\alpha^4} - \frac{1}{\beta^4})} e^{ikx} \tag{4.21}$$

The more elaborate solutions of Goodman et al. (1980) and Wadhams (1986) have the same amplitude as we have derived but a different functional form due to the finite size of the ice floe they assumed and different boundary conditions they applied. Using equation 4.15 we find that the amplitude of the maximum bending stress is:

$$\tau_{swell} = \frac{EH_i}{2(1-\nu^2)} \frac{Ak^2}{\left(\alpha^4 k^4 + 1 - \frac{\alpha^4}{\beta^4}\right)} \tag{4.22}$$

where we have omitted the e^{ikx} modulation of the bending stress. The final equation we need to close the system is the dispersion relation between the wavenumber, k, and frequency, ω of the incoming wave. The dispersion relation for flexural-gravity waves is given by (Wadhams, 2000):

$$Dk^5 + (\rho_w g - \rho_i H_i \omega^2)k - \rho_w \omega^2 = 0 \tag{4.23}$$

Equation 4.23 has five roots for k as a function of ω. The real root is a conservative wave. In addition there are two complex conjugate pairs that represent evanescent waves. Figure 4.8 shows the maximum bending stress for swell of a range of periods, determined from the real root of equation 4.23 normalized per unit wave amplitude for a 400 m thick ice shelf.

It is apparent from Figure 4.8 that ocean swell can cause significant stress within the ice shelf. Although it is highly unusual to observe swell with periods greater than 18 seconds, even moderate ocean swell of period 12-18 seconds with amplitudes of 10-20 meters would result in bending stresses comparable to the glaciological stress. Storms that produce long period swell with amplitudes of tens of meters are rare but not unheard of. The amplitude of the swell will attenuate exponentially with distance into the ice shelf. Therefore, swell will only be important for those rifts that are quite close to the ice front. This may explain why the presence of sea ice does not significantly affect propagation of the rift on the Amery Ice Shelf. Rift T2 is located about 30 km from the front, and swell may be substantially attenuated at these distances. In contrast, MacAyeal et al. (2006) have argued that ocean swell can lead to the breakup of large tabular icebergs and have speculated that increased storminess could contribute to increased calving rates. Our calculations indicate that the effect of increased ocean swell is likely to be minimal, affecting only those rifts that are already close to the ice front.

4.3.3 Internal Glaciological Stress

Our analysis indicates that the glaciological stress is the largest term in the force balance and is therefore the most likely driving stress for rift propagation. However, this does not explain why rift propagation is episodic, because the internal stress within the ice is relatively constant. One possibility is that the episodic propagation events are related to the crystal structure of ice. There is evidence for this in fracture experiments of ice (Rist et al., 2002). This behavior, misleadingly called “stick-slip”, occurs over a very small spatial scale (typically tens of centimeters), and is usually ascribed to the crystal structure of ice or brine pockets within the ice. Over the larger length scales of rift propagation (hundreds to thousands of meters), these microscopic effects will become less and less important. Furthermore, episodic propagation appears to be a feature of crack propagation in a variety of materials over a variety of spatio-temporal scales. For example, the episodic nature of earthquakes is well known, but episodic propagation also occurs over the smaller laboratory scale measurements of many rocks (Reches and Lockner, 1994) and has been invoked to explain lithospheric rift propagation (Floyd et al., 2002). Episodic propagation is clearly not a property unique to ice.

Another hypothesis is that rift propagation occurs over a sequence of steps involving the initiation of smaller micro and meso-scale cracks ahead of the rift tip (detailed in Chapter 3). As the density of these cracks increases, they eventually coalesce into a single crack extending the length of the rift. This process has been observed in fracture mechanics experiments of rocks (Reches and Lockner, 1994). The implication is that ice shelf rift propagation may be similar in nature to brittle failure of rocks and that episodic rupture events may be a general feature of fracture as opposed to a specific property of an individual material.

4.4 Conclusions

Our observations show that the timing of rift propagation events do not coincide with periods of high winds or tidal amplitudes. This demonstrates that neither of these variables, by themselves or in combination, triggered a rift propagation event. Similarly, we find that a significant impulse input such as the tsunami generated by the December 26th, 2004 Sumatra earthquake also did not trigger a rift propagation event, although we did observe one event several days after the tsunami arrived. This strongly suggests that these variables are not the primary drivers of rift propagation. If environmental variables do not drive rift propagation, we conclude that the glaciological stress within the ice must be the primary driver. Furthermore, order-of-magnitude calculations suggest that these environmental variables may become increasingly important as the rift system becomes more mature and iceberg detachment becomes more imminent. These calculations explain why the stresses that are known to be important in iceberg drift and evolution appear to be unimportant in driving rift propagation. It also suggests that, over the next several years as the Loose Tooth comes closer to detachment, environmental stresses will begin to have a larger impact on rift propagation.

Chapter 5

Vertical Deformation and Flexure Associated with Ice Shelf Rifting

> Research is what I'm doing when I don't know what I'm doing
>
> – Wernher von Braun

Abstract

During our initial field campaign in 2002-03, we noticed that the northern (i.e. seaward) side of rift T2 was uplifted relative to the southern side. To investigate this trend, we deployed a line of GPS receivers in a transect normal to the rift axis. Vertical velocities, derived from our GPS data, show a differential velocity across the rift where the northern side of the rift was moving upwards relative to the southern side. The magnitude of the differential velocities was greatest near the rift axis and decreased with distance away from the rift. This pattern of uplift was confirmed by elevation profiles obtained by the Geoscience Laser Altimeter System (GLAS) on board the Ice, Cloud and land Elevation Satellite (ICESat). ICESat profiles show that the northern side of the rift has a sharp upward jut while the southern side slopes slightly downwards. These profiles also reveal that the magnitude of uplift varies with distance from the rift tip, and that the southern side is occasionally uplifted higher than the northern side. We interpret this

pattern of deformation as evidence of normal faulting during the rift formation process. We present analytic solutions for one dimensional elastic beam bending and show that the wavelength of deformation is too short to be an elastic effect. This suggests that the pattern of deformation may be better explained as viscous deformation. We compare our GPS derived velocities with an analytic solution for viscous beam bending first derived for lithospheric subduction zones. The analytic solution matches the data well and predicts modest rift wall deviations from a vertical of 1 to 3 degrees, similar to the rift wall slopes determined by King (1994) for a rift on the Ronne Ice Shelf.

5.1 Introduction

In chapters 2 and 3 we primarily considered horizontal deformation associated with rift propagation and neglected the vertical component of this deformation. The vertical signal also provides important information about the nature of rift propagation. This is especially true in the near field (i.e. within several ice thicknesses of the rift tip) where the stress (and strain) fields are fully three-dimensional (e.g. Broberg, 1999).

The focus of this chapter is on explaining a persistent feature observed in the field. The north (seaward) rift wall was offset upward by approximately 1 meter relative to the southern wall (Figure 5.1). The amplitude of the uplift decreased from a maximum of one meter at a distance of approximately 3 km from the rift tip to zero at the rift tip. We wondered whether the process causing the offset might also be important in driving rift propagation. For example, the ice may be tearing along a thickness discontinuity, perhaps related to marine ice formation. Alternatively, the uplift may be related to the rifting process itself, in which case understanding the cause of the offset may be crucial to understanding and modeling rift propagation.

To investigate the cause of the offset observed in the field, we installed a line of GPS receivers normal to the rift, close to the rift tip (Figure 5.2). The GPS

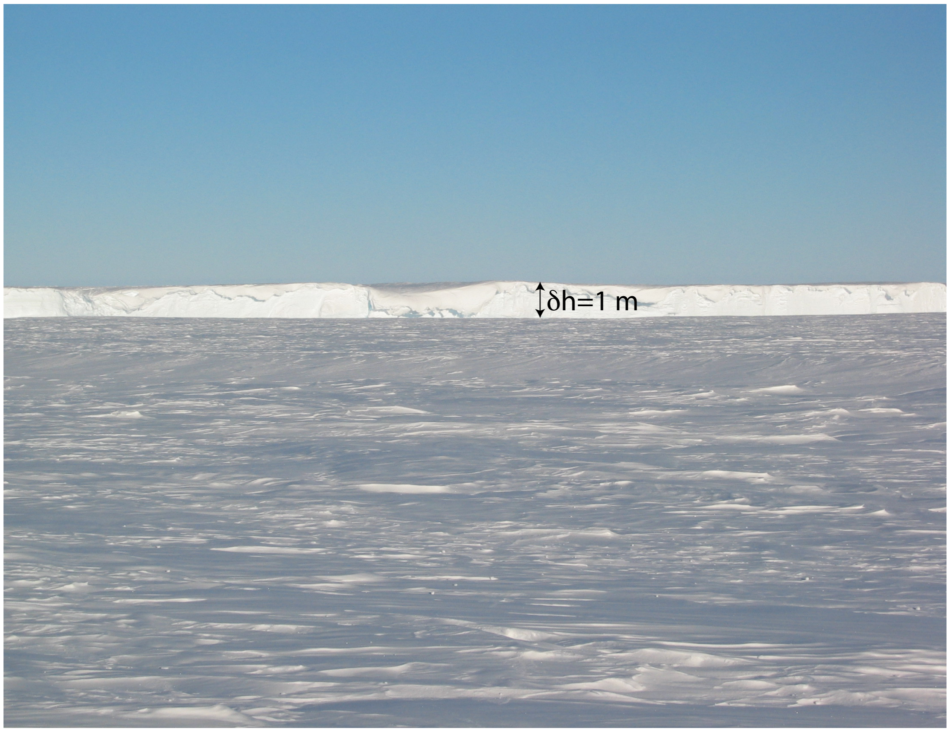

Figure 5.1: Photograph taken from the south side of the rift looking north, illustrating the uplift of the northern side. Although difficult to tell from the image, the magnitude of the uplift is about 1 meter and tapers off towards the rift tip (to the right in the photograph). Photograph by R. Coleman.

were placed so that we could determine whether there was a pattern to the vertical velocities with respect to the rift axis. The two stations furthest away from the rift axis (a and f) were placed 1.5 km away from the rift to provide an estimate of the far-field deformation. In addition, we used elevation profiles that crossed the rift obtained by the Geoscience Laser Altimeter System (GLAS) onboard the Ice, Cloud and land Elevation Satellite (ICESat). These elevation profiles provide the larger scale topography across the rift. The primary objective of this study was to determine the cause of the uplift. A further objective of the study was to determine whether relative kinematic GPS positioning would be able to provide sufficient resolution to resolve the small vertical signal that might be generated by plastic deformation near the rift tip (e.g. Broberg, 1999).

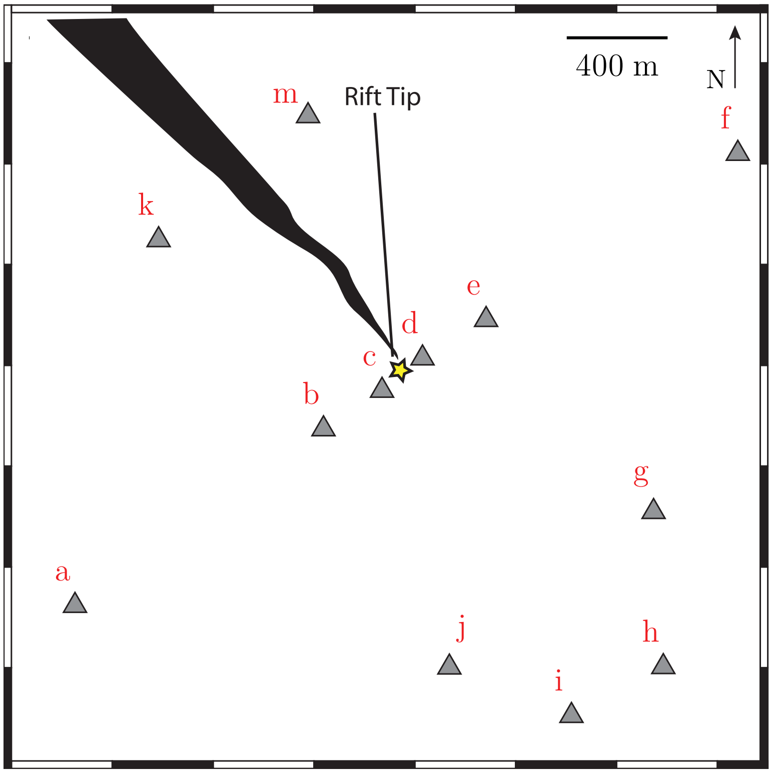

Figure 5.2: Map showing the placement of GPS stations in relationship to the rift. The yellow star indicates the rift tip at the beginning of the survey during the 2005-06 field season.

5.2 GPS Processing and Results

We processed the six GPS sites that make up a profile normal to the rift axis (sites a-f) kinematically as described in Chapter 3, section 3.4.1, for the 2005-06 field season. We did not use the data from 2004-05 season because the poles fell over. We then calculated the vertical velocity from the slope of the least-squares fit to the time series of vertical displacements. We chose a reference frame relative to the mean velocity at the two stations furthest from the rift tip (a and f). Using this convention, the relative velocities for each site are shown in Figure 5.3. We estimated the error bars using a "bootstrap" method whereby we repeatedly computed the slope using a subset of 10% of the data, chosen at random with replacement. The error in the velocity was then computed from the standard deviation from the set of realizations of the velocity. Inspection of figure 5.3 shows

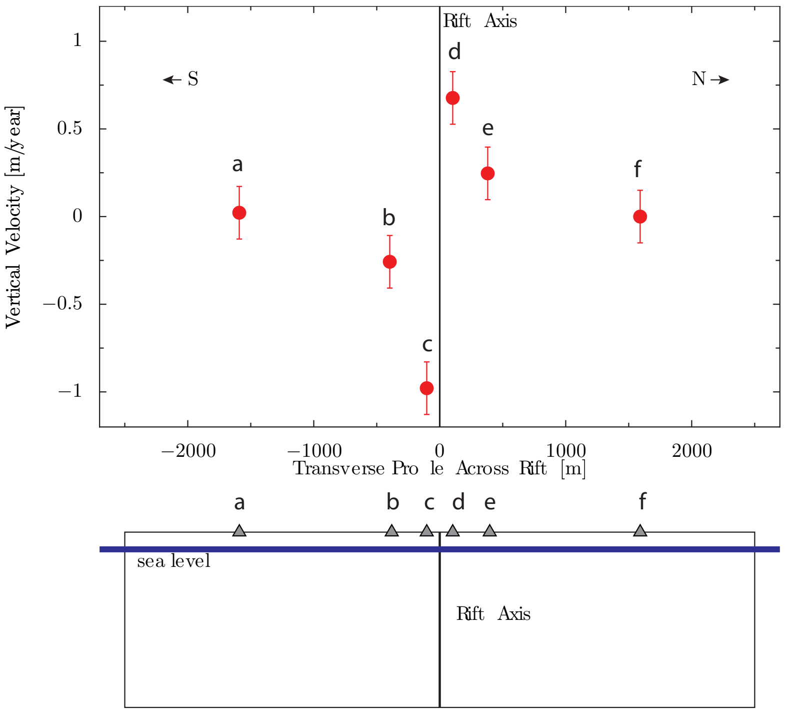

Figure 5.3: Upper figure shows the vertical velocity determined from our GPS for a cross-section across the rift. The lower panel illustrates the placement of the receivers with respect to the rift axis (for a map view of the GPS sites see Figure 5.2)

that the northern side of the rift is moving upwards while the southern side of the rift is moving downwards. The magnitude of the velocity decreases away from the rift, approaching zero at the two stations furthest away from the rift (a and f). The pattern of uplift is consistent with what we observed in the field. If we assume steady-state then, with a maximum velocity of uplift of approximately 1 m/year, we estimate it would take approximately 1-2 years to form the 1-2 meter offset observed. We also noticed that the differential velocities approach zero in the far-field (i.e. sites a and f), further indicating that the deformation is rift-related.

5.3 ICESat Processing and Results

GPS provides relative velocities at discrete points along the rift. To determine topography across the rift, we also analyzed elevation profiles from the

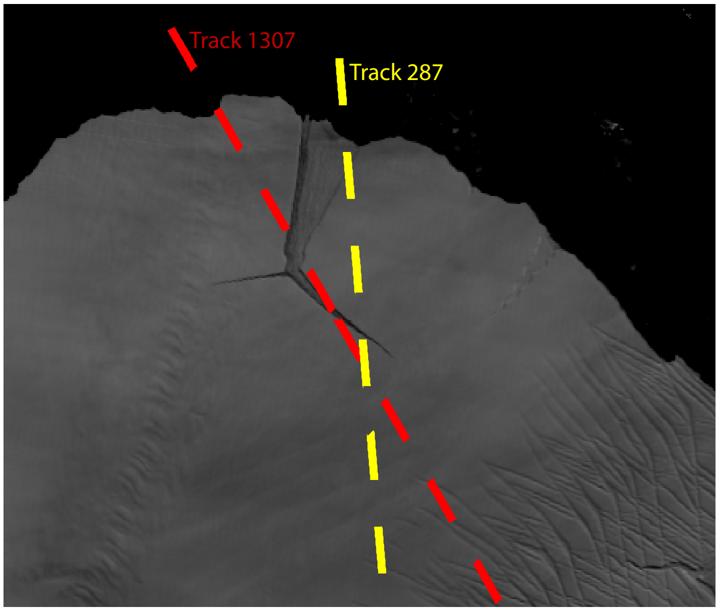

Figure 5.4: MODIS image acquired on January 14th, 2006 showing the orientation of ascending (red) and descending tracks (yellow).

Geoscience Laser Altimeter System (GLAS) on the Ice, Cloud and land Elevation Satellite (ICESat). The small footprint and high along-track resolution of GLAS (∼65 m footprint and ∼172 m spacing) is capable of resolving small-scale features that are obscured by the larger footprints of other altimeters (Fricker et al., 2005a). Rift T2 is a "target of opportunity" for ICESat, whereby the spacecraft is pointed off-nadir so as to hit the same geographical location when its planned ground-track falls within 50 km. Furthermore, because the ice is continually advecting north-east, each ICESat track hits a different location on the rift. Therefore each ICESat track provides an elevation profile across the rift at a different time and location. In addition, because of rift propagation, subsequent tracks also intersect with the rift at increasing distances from the rift tip.

The data and processing procedures used are described in Fricker et al. (2005a). We used ICESat data from the 91-day repeat phases: Laser 2a (Release 21); Laser 2b, (Release 18); Laser 2c (Release 17); Laser 3a (Release 18); Laser 3b (Release 19); Laser 3c (Release 22); Laser 3d (Release 26); Laser 3e (Release 26) and Laser 3f (Release 28).

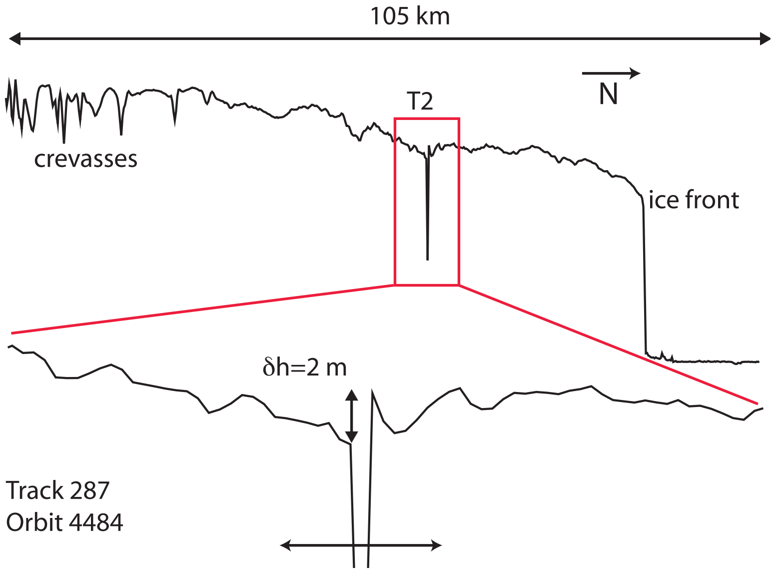

Figure 5.5: ICESat profile across T2 acquired on the 18th of October 2003. Upper profile: Larger scale track segment extending up stream of T2 and crossing the ice front. Lower profile: zoom around T2.

The orientation, relative to the rift of both ascending and descending tracks are shown in Figure 5.4. Figure 5.5 shows a descending profile that crosses the Amery Ice Shelf and intersects with rift T2. The ice cliff at the ice shelf front is apparent as is a band of crevasses/rifts that occur upstream of T2. Rift T2 occurs in a slight topographic dip, but the topographic signature associated with rifting is not significantly larger than other, non-rift related topography seen upstream from the rift. It is possible that the dip is related to plastic deformation generated by the high concentration of stress ahead of the rift tip, but it may also be related to post-rifting ice shelf flow or to non-rift related processes. A zoom around rift T2 (shown beneath the main profile) shows about 2 meters of uplift on the northern side of the rift relative to the southern side. Additionally, the southern side has a slight downward slope.

Figures 5.6 and 5.7 show the ascending and descending elevation profiles acquired over rift T2. Both ascending and descending profiles show that the northern side of the rift juts upward while the southern side has a gentler downward

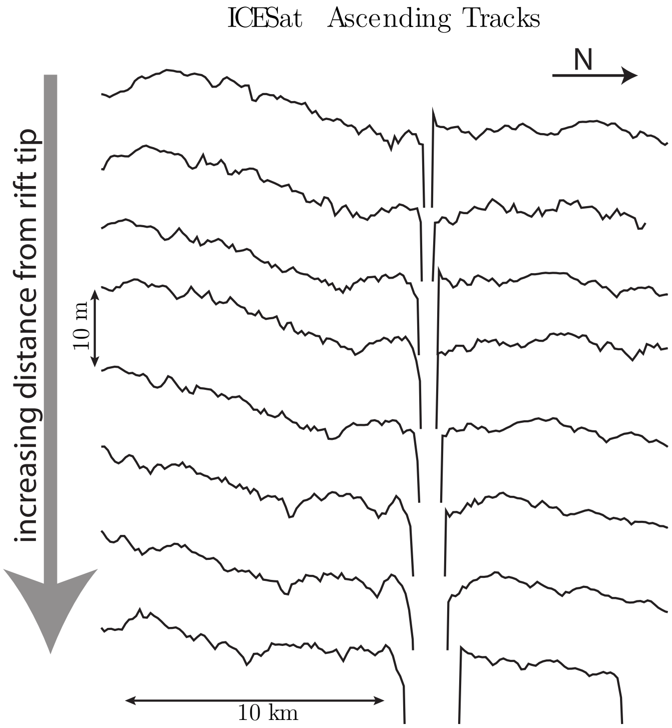

Figure 5.6: Ascending GLAS elevations profiles across T2. Track and orbit numbers for each profile, from top to bottom are: Track 1307, Orbit 04150; Track 1307, Orbit 05995, Track 72, Orbit 07468; Track 191, Orbit 07587; Track 191, Orbit 09655; Track 72 Orbit 11589; Track 72, Orbit 12943; Track 72, Orbit 15234.

slope into the rift. The magnitude of the offset closest to the tip has a magnitude of about 2 meters but appears to decrease with distance away from the rift tip, and even appears to change sign in some profiles (see e.g. second profile in Figure 5.6). On the northern side of the rift, the slope of the ice is much smaller. In some profiles, both sides of the rift are uplifted while in other profiles only one side of the rift is uplifted.

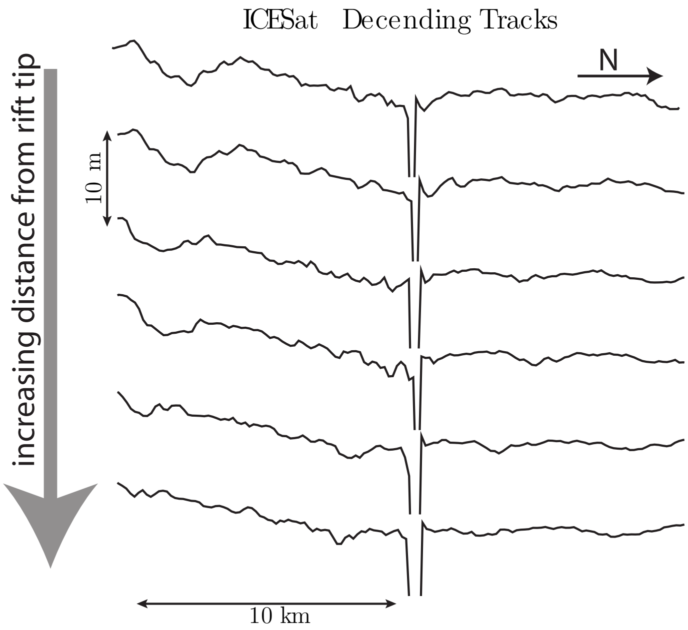

Figure 5.7: Descending GLAS elevation profiles over rift T2. Track and orbit number for each profile, top to bottom are: track 1269, orbit 04112; track 287 orbit 04484, track 168, orbit 09632; track 287, orbit 09751; track 287, orbit 13158; track 287, orbit 15449.

5.4 Explanations for the Rift Offset

We have considered four possible hypotheses for the observed offset: (1) under plating by marine ice, (2) rift wall melting, (3) moment induced bending and (4) asymmetric rift walls caused by normal faulting. Each hypothesis is discussed separately below.

5.4.1 Hypothesis 1: Under Plating by Marine Ice

The first hypothesis we considered is that the ice is thicker on the northern side of the rift than the southern side. If the ice is in hydrostatic equilibrium, then the added thickness will cause the thicker side to float higher in the water (Figure 5.8). For ice density ρ_i, water density ρ_w, and offset δh, the increased thickness on

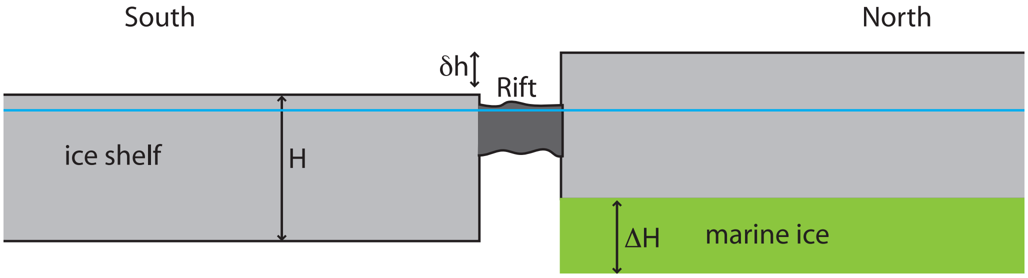

Figure 5.8: Schematic diagram illustrating the effect of a thicker ice shelf on the northern side caused by increased marine ice accumulation underneath.

the northern side of the rift necessary to produce the observed amount of uplift is:

$$\Delta H = \frac{\delta h}{\left(1 - \frac{\rho_i}{\rho_w}\right)} \tag{5.1}$$

For typical values of ice and water density (ρ_w=1020 kg/m^3, ρ_i=920 kg/m^3) and offset Δh=1 m, this would necessitate an ice thickness difference ΔH of about 10 meters. Re-freezing of marine ice at the base of the ice shelf could produce a thickness discontinuity of 10 meters or more. If such a thickness gradient were present (either pre or post-rifting) the differential "tearing force" caused by the buoyancy difference could be important in driving rift propagation. If the thickness discontinuity were present prior to rifting, it is possible that the rift is rupturing along a pre-defined path defined by the discontinuity. If true, this would suggest that we need to better understand how these small scale discontinuities are formed at the base of the ice shelf by melting and freezing. On the other hand, if rift propagation precedes the thickness discontinuity, then it indicates that there is an important and poorly understood interaction between rifting and local ocean circulation that needs to be explored. Examining the ICESat profiles and our GPS derived velocities, we think it is unlikely that under plating is causing the uplift because, whether marine under plating was responsible for the uplift, we would expect that the magnitude of uplift would be greatest away from the rift, not at the rift axis. Our GPS derived velocities and ICESat derived elevation profiles show just the opposite; uplift is greatest along the rift axis. It is possible that there is

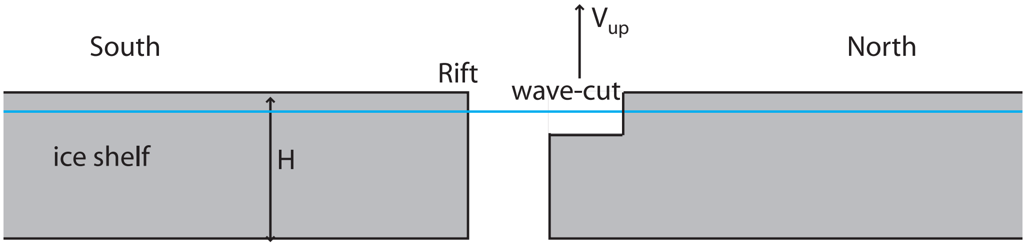

Figure 5.9: Diagram illustrating the force that a subsurface wave-cut (as proposed by Scambos et al. (2005)) would generate on the rift wall. If the wavecut only forms on the northern side, then it could produce the signal that we see. The question is why would the wavecut only form on the northern side of the rift?

some mechanism that may produce larger amounts of marine ice near one rift wall leading to greater uplift closest to the wall, but this has never been observed and we therefore reject this hypothesis.

Hypothesis 2: Rift Wall Melting

The second hypothesis is that instead of large-scale marine ice formation causing a thickness differential across the rift, small-scale melting along the rift walls causes a ”wavecut” (Figure 5.9). This mechanism was invoked by Scambos et al. (2005) to explain uplift that they observed along the walls of drifting icebergs. Scambos et al. (2005) detected about 1 m of uplift, comparable to what we have observed. However, we do not think that the melting mechanism proposed by Scambos et al. (2005) can cause the offset that we see. The only way that rift wall melting could produce an offset between the two rift walls is if melt occurs more rapidly (or exclusively) on the northern side of the rift than the southern side of the rift. There are no obvious mechanisms that would favor melting on one side of the rift. Furthermore, in contrast to the icebergs studied by Scambos et al. (2005), the rift is filled with ice debris (mélange) making it unlikely that a warmer surface layer of water could form near the surface, as postulated by Scambos et al. (2005). We therefore reject this model as unrealistic.

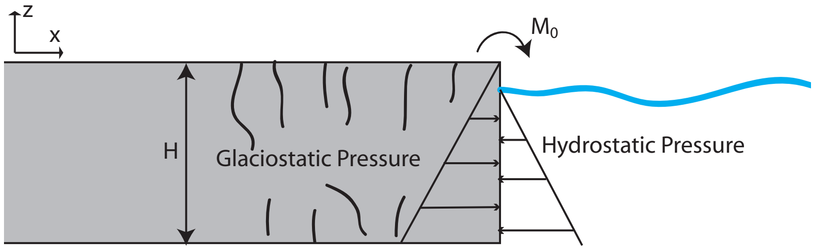

Figure 5.10: Diagram illustrating the moment applied to the rift wall due to the imbalance between hydrostatic and glaciostatic pressures along with the coordinate system used for the remainder of the calculations in this chapter.

Hypothesis 3: Moment Induced Bending

The difference between the glaciostatic pressure of the ice and the hydrostatic pressure of the sea-water mélange combination filling the rift could exert a moment on the rift wall. This effect was explored in early calving studies that focused on the bending stresses caused by this imbalance between glaciostatic pressure and hydrostatic pressure at the glacier front (Reeh, 1968; Fastook and Schmidt, 1983; Hughes, 1992). The imbalance between glaciostatic pressure and hydrostatic pressure results in a net, outwardly-directed tensile stress (Figure 5.10), and a bending moment (M_0):

$$M_0 = \int_0^H (P_i - P_w) z \left(z - \frac{H}{2} \right) dz \tag{5.2}$$

Here P_i is the glaciostatic pressure of ice and P_w is the hydrostatic pressure of water; we have used the Euler beam bending hypothesis that the moment at the center of the beam is zero. Carrying out the integration with column averaged densities we find:

$$M_0 = \frac{1}{12} \rho_i g H^3 \left(1 + 3\frac{\rho_i}{\rho_w} - 4\frac{\rho_i^2}{\rho_w^2} \right) \tag{5.3}$$

In equation 5.3 ρ_i is the density of ice, ρ_w is the density of water, g is the acceleration due to gravity and, as before, H is the ice thickness. Reeh (1968) included higher order terms that arise because, as the ice shelf bends, the moment changes. For simplicity we neglect these terms. Larour et al. (2004b) recognized that this situation is identical to that of a mélange-free rift cavity and used a finite element model to simulate viscous flexure of a rift on the Ronne Ice Shelf. These authors found that their numerical solution predicted qualitatively the pattern of uplift they observed, but the actual uplift was larger in magnitude than predicted. In addition, this type of mechanism cannot generate an asymmetrical offset unless different moments are applied to each rift wall. No mechanism to explain why a different moment would be applied to each rift wall has been proposed. Furthermore, because the rift is filled with mélange, the moment applied to the rift walls would actually be less than that derived by Larour et al. (2004b). We are forced to reject this hypothesis as well.

Hypothesis 4: Asymmetric Rift Walls Caused by Normal Faulting

The final hypothesis that we considered is that the rift walls are asymmetric. We did not notice any slope to the rift walls in the field. It is possible that at depths beyond where we can see, the rift walls are not perfectly straight or that the tilt of the rift walls is modest enough not to be obvious by inspection. There is some evidence for this in rifts in other ice shelves. King (1994), perhaps unwittingly, performed a seismic survey across the top of a rift on the Ronne Ice Shelf and found an asymmetry in the shape of the rift walls. This pattern of uplift, where one side of the rift is uplifted relative to the other, is reminiscent of lithospheric rifting. While Bullard (1936) originally proposed that compressional forces caused the uplift, the modern view is just the opposite; extensional forces result in normal faulting of the lithosphere (Figure 5.11) and patterns of uplift where one side of the rift is elevated relative to the other (Vening Meinesz, 1950). This tantalizing coincidence suggests that the same processes responsible for lithospheric rift wall uplift may also be responsible for ice shelf rift wall uplift. If true, this is an intriguing hypothesis because then ice shelf rifting might provide a window through which processes that occur during lithospheric rifting can be directly observed (over much shorter time-scales), albeit in a colder climate than

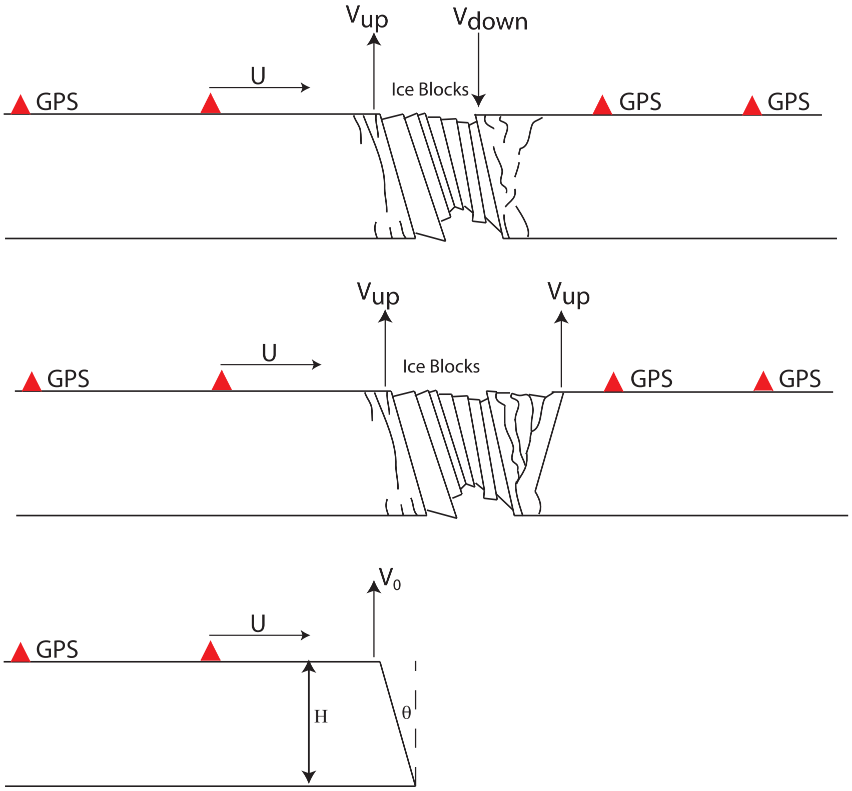

Figure 5.11: Diagram illustrating "normal faulting" of an ice shelf. In this model rift formation occurs via the generation of a sequence of ice blocks that fall into the rift. As the rift widens a series of smaller blocks of ice are "calved" into the rift center. Relative to the rift wall, fixed GPS sites advect towards the rift wall at velocity U. The lower panel shows the geometry used in calculating the flexural profiles in the remainder of this chapter. This resembles qualitatively what we observed in the field.

many geologists and geophysicists are used to.

The classic model for rift wall uplift of lithospheric rifts is that fractures occur as a series of normal faults, fracturing at an angle θ (Figure 5.11, lower panel). Buoyancy results in an upward force on one side of the rift and a downward force on the other. As a first approximation, we can apply the buoyancy force directly to the rift wall. The magnitude of this force as a function of the angle, θ, is then (Watts, 2001) is

$$V_0 = \frac{H^2}{2}\tan\theta(1-\frac{\rho_i}{\rho_w})\frac{\rho_i^2}{\rho_w}g \tag{5.4}$$

Where H and θ are defined in Figure 5.11. For generality, we also allow for a moment M_0 to be applied to the rift wall. Assuming an elastic response, the displacement (w) can be modeled using the elastic flexure equation (Turcotte and Schubert, 2002):

$$D\frac{d^4w}{dx^4} + \rho_w g w = 0 \tag{5.5}$$

The solution to equation 5.5 for a semi-infinite beam with bending moment M_0 and line force V_0 applied to the end can easily be found (e.g. Turcotte and Schubert, 2002):

$$w = \frac{\alpha^2}{2D}e^{-x/\alpha}\left[-M_0 \sin\frac{x}{\alpha} + (M_0 + V_0\alpha)cos\frac{x}{\alpha}\right] \tag{5.6}$$

where we have introduced the flexural wavelength:

$$\alpha = \left[\frac{4D}{\rho_w g}\right]^{1/4} \tag{5.7}$$

By assuming flexure can be modeled as an elastic beam, we are neglecting three dimensional and time-dependent effects. Close to the rift tip, there will also be a pattern to the uplift that depends on a variety of three-dimensional variables such as the distance from the tip, whether the rift penetrates the entire ice thickness. Neglecting these factors will result in an over-estimate of the magnitude of the uplift that we compute.

Figure 5.12 (upper panel) shows the elastic displacement profiles for deviations from vertical rift walls of 5,10 and 20°. The photograph shown in Figure 5.1 was taken at a distance of approximately 500 m from the rift wall. Figure 5.12 shows that the displacement has a smooth shape that decreases with distance away from the rift axis, similar to what we have observed in the field, with our GPS and with ICESat. Obtaining 1 m of uplift is easy for fairly small values of θ. We examined the effect of varying the slope of the rift walls on the maximum uplift achievable (lower panel in Figure 5.12). Achieving a 1 m uplift is possible with deviations from a vertical rift wall as small as 5°-10°. This indicates that normal faulting is a feasible mechanism for generating the observed uplift. This hypothesis best explains the pattern of uplift that we observe.

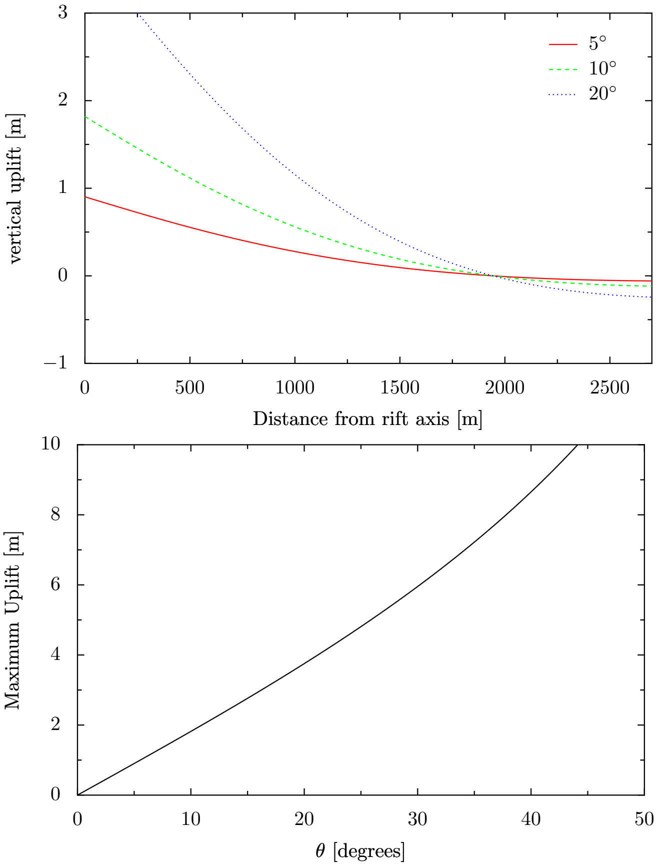

Figure 5.12: Upper panel: Three flexural profiles for an elastic ice shelf with vertical shear force determined from equation 5.4 and walls sloping at angles ranging from 5°-20°. Lower panel: The maximum uplift for an elastic ice shelf as a function of θ. θ represents the deviation from a vertical rift wall.

5.5 Mechanical Models of Rift Uplift

In the previous section we showed that the most promising explanation for the rift wall uplift is normal faulting. This hypothesis is intriguing because of the close analogy to lithospheric rifting, but we immediately encounter a problem with the simple elastic model proposed in the previous section. Our GPS results indicate that there is a vertical (GPS-derived) velocity between sites, a result that is incompatible with the classic quasi-static elastic response. The elastic response would be very fast (seconds) leading us to expect a constant topographic profile with zero differential vertical velocity between sites. A simple alternative is to assume that the ice is responding elastically to a slowly changing moment or line force along the rift wall. We can approximate this by taking the time derivative of equation 5.6:

$$\frac{dw}{dt} = \frac{\alpha^2}{2D} e^{-x/\alpha} \left[-\frac{dM_0}{dt} \sin\frac{x}{\alpha} + (\frac{dM_0}{dt} + \frac{dV_0}{dt}\alpha) cos\frac{x}{\alpha} \right] \tag{5.8}$$

We attempted to fit equation 5.8 to our GPS data, but we found that the elastic wavelength predicted is much larger than our data will permit. This suggests that the response is not purely elastic. Expecting the ice to behave as an elastic body over the 20-day time-scales of our observations is unrealistic. Instead, the full non-linear rheology of ice should be used in computing the flexural response of the ice. Time-dependent solutions for non-Newtonian beam flexure can only be found numerically. Rather than developing a numerical model, we adopt a simplified approach. Because the qualitative nature of flexure is remarkably robust under different rheologies, we fit the elastic solution (equation 5.5) to the velocities determined from our GPS, assuming that that the instantaneous velocity is given by equation 5.8 with an effective thickness H_{eff}. In general, H_{eff} may vary with time.

Figure 5.13 shows the best fit of equation 5.5 to the GPS data with H_{eff}=100 m. Other solutions with H_{eff} varying from 50-200 m were also performed but yielded a greater misfit with the data. The derived deviations from a shear vertical rift wall for H_{eff}=100 are small, on the order of 1-3 degrees for each wall. While obscuring some of the underlying physics of the deformation, this approach has some benefits. The initial response of the ice will be elastic, and, therefore, if the time dependence of the deformation can be determined, then we should see that H_{eff} decreases with time as viscous deformation begins to dominate elastic deformation. If the loading is known, this could be used to test parametric models of ice rheology. The large difference between the actual thickness of the ice and the effective thickness suggests that the signal we are seeing is not an elastic response of the ice shelf, but it is not clear how this relates to the actual rheology of ice. Previous studies have used complicated numerical models to determine

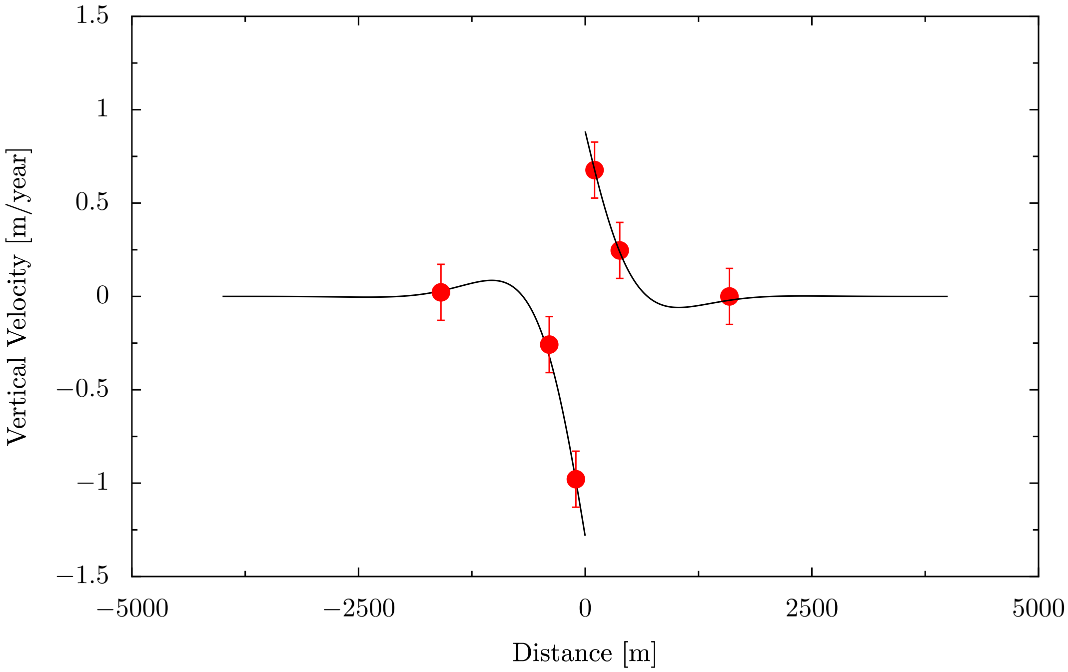

Figure 5.13: Best fitting model for an elastic ice shelf with effective thickness $H_{eff} = 100m$. We assume that the velocity is determined by an equation analogous to 5.5 with a different thickness. Red circles are GPS derived velocities. Error bars were determined from bootstrapping.

flexural profiles with a range of rheologies for ice (Reeh, 1968; Larour et al., 2004b; Scambos et al., 2005). In the next section, we propose an alternative approach that exploits the analytic viscous solution derived by De Bremaecker (1977) to describe subduction zones.

5.5.1 Viscous Model - Advection Dominated:

The model that we propose is illustrated in Figure 5.11. In this model, rift propagation occurs as sequence of normal faults where blocks of ice slide into the rift. In the reference frame of a GPS on one side of the rift, the GPS site is moving towards the rift edge at constant velocity U. Distances between different GPS sites remain approximately constant. We thus neglect the constant spreading of the ice shelf in this calculation. In the field, we saw that the rift was filled with large blocks of ice that detached from the rift walls, qualitatively similar to what is sketched in Figure 5.11.

Starting with the flexural equation for a viscous plate (see e.g. Nadai, 1950):

$$L\frac{d^4}{dx^4}\frac{dw}{dt} + \rho_w g w = 0 \tag{5.9}$$

L plays the same role as the flexural rigidity (D) did for the elastic beam. For an incompressible Newtonian viscous fluid of viscosity, η, L is defined as:

$$L = \frac{\eta H^3}{9} \tag{5.10}$$

$\frac{dw}{dt}$ contains both the derivative of the displacement with time and an advective term:

$$\frac{dw}{dt} = \frac{\partial w}{\partial t} + U\frac{dw}{dx} \tag{5.11}$$

Because rift uplift is persistent from season to season, we make the assumption that the uplift is in steady state and set $\frac{\partial w}{\partial t}$ to zero, leaving only the advective term (the validity of this assumption is discussed in section 5.5.2. Equation 5.9 then becomes a fifth order differential equation:

$$UL\frac{dw^5}{dx^5} + \rho_w g w = 0 \tag{5.12}$$

This equation is identical to that for an elastic plate with UL replaced by D, with the exception that there is an extra spatial derivative for w in the first term. Fifth-order equations are uncommon in mathematical physics so there is some uncertainty about how best to enforce the five boundary conditions. We follow the approach of De Bremaecker (1977) and assume a semi-infinite beam. The general solution then has five terms, three of which are singular for large values of x. We discard these unphysical solutions leaving us with a general solution with two undetermined coefficients(De Bremaecker, 1977):

$$w = e^{-x/a}\left(P\sin x/p + Q\cos x/p\right) \tag{5.13}$$

with

$$a = \left(\frac{\rho_w g}{LU}\right)^{-1/5}\cos(\pi/5) \tag{5.14}$$

$$p = \left(\frac{\rho_w g}{LU}\right)^{-1/5}\sin(\pi/5) \tag{5.15}$$

The characteristic wavelength is given by p. Using appropriate values for ice shelf ice, $\eta = 10^{12}$ Pa s, H=400 m, ρ_w=1020 kg m^{-3},g=9.8 m/s^2 and U=0.1 m/s, we find $\lambda \sim 800$ m, in reasonable agreement with the GPS data shown in Figure 5.3. The vertical velocity is obtained by differentiating equation 5.11. The coefficients P and Q can be related to the shear force and bending moment at the end by using the boundary conditions. Similar to case for an elastic beam, the boundary conditions that we apply are to the moment at the end M_0 and a line force at the end V_0. These two boundary conditions translate to two conditions on $w(x)$:

$$-LU\frac{d^3w}{dx^3} = M_0 \tag{5.16}$$

$$-LU\frac{d^4w}{dx^4} = V_0 \tag{5.17}$$

Solving for P and Q we find the (horrendous) equations:

$$P = \frac{p^4M_0 + \left(-3\,aV_0 - 6\,a^2M_0\right)p^2 + a^3\left(aM_0 + V_0\right)}{LUp\left(a^6 + 3\,a^4p^2 + 3\,a^2p^4 + p^6\right)} \tag{5.18}$$

$$Q = \frac{4\,M_0a^3 + 3\,V_0a^2 - 4\,p^2M_0a - 1\,p^2V_0}{LU\left(a^6 + 3\,a^4p^2 + 3\,a^2p^4 + p^6\right)} \tag{5.19}$$

We performed a least-squares fit to the GPS data using equation 5.13 with M_0 set to zero. The best fit is shown in Figure 5.14. There are not enough data points to make the problem substantially overdetermined. Nonetheless, we can get reasonable agreement between the data and our analytic solution. The best fitting deviations from a vertical rift wall that we find are, similar to the elastic case, close to vertical with deviations on the order of a few degrees.

Our viscous bending model predicts two things. The first is that there is some asymmetry in the rift walls that results in buoyancy forces. One way to test this model is to perform a seismic reflection survey in a profile across rift T2 in conjunction with our GPS to determine the actual shape of the rift walls. This would validate or disprove the model. The second feature that our model predicts is that the uplift and downward bending of the rift walls are related to the production and formation of mélange within the rift (this results in the advection term into the rift). This means that we should not see a vertical velocity for relic rifts (i.e. ones

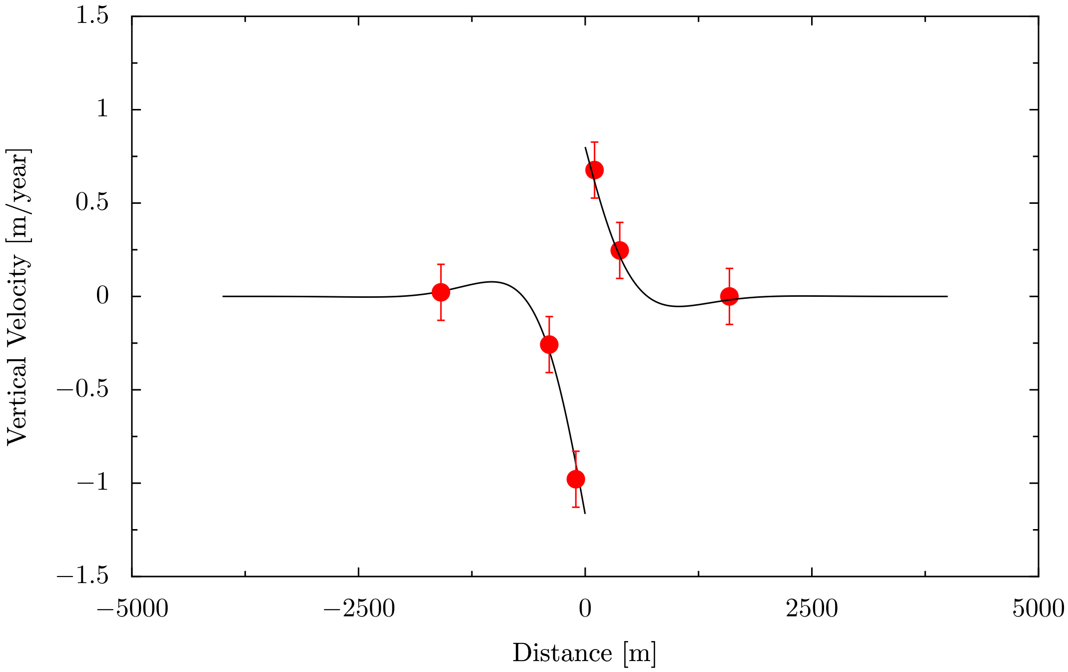

Figure 5.14: Best fitting viscous model of bending. The parameters used were H=400 m, η=10^{14}, U=0.01 m/s. The product of velocity (U) and viscous rigidity (L) determines the wavelength. Red circles are the GPS derived velocities

that are no longer propagating). These rifts should maintain relatively constant widths and mélange thickness. This may also be true further away from the rift towards the triple junction where mélange thickness remains relatively constant and only a small number of ice blocks fall into the rift. There is some evidence in the ICESat elevation profiles across the rift that the magnitude of the uplift decreases away from the rift tip. There does not appear to be any physical reason for the northern side to be favored. Instead our model predicts that either side could be uplifted relative to the other and this is what we see in the ICESat elevation profiles. A key question that needs to be answered is whether the uplift is always greatest on the northern side or occasionally switches sides.

5.5.2 Transient Effects

While the viscous model fits the limited data reasonably well, it is useful to estimate how accurate this approximation is. The general time dependent solution to the viscous bending problem cannot be determined in closed form, but we can estimate the approximate time scale for transient effects by introducing the Laplace-Fourier transformed solution:

$$w = w_0 exp(ikx - t/\tau_{visc}) \tag{5.20}$$

The magnitude of τ_{visc} determines how quickly transient effects either grow or are damped. Substituting equation 5.20 into equation 5.9 we can solve for the growth rate factor q:

$$\tau_{visc} = \frac{Lk^4}{\rho_w g} = \frac{L}{\rho_w g \lambda} \tag{5.21}$$

For a wavelength of λ=1000 m (typical of what we observe with our GPS) and η ranging from 10^{11}-10^{14} we find that τ_{visc} ranges between several hours to several days. This provides some confirmation that our steady state approximation is reasonable and that there is a relatively rapid adjustment to steady-state over periods as short as several days.

5.6 Conclusions and Future Work

In this chapter we have explored four hypotheses put forward to explain the elevation offset across the rift (observed in the field, with our GPS and with GLAS data). Of the four explanations (under plating by marine ice, rift wall melting, moment induced bending, asymmetric rift walls) we have determined that the most likely explanation is asymmetric rift walls caused by normal faulting. We have modeled the deformation as the viscous flexural response of the ice shelf to rift walls that deviate from perfectly vertical. Our model is simple but has the key ingredients necessary to match the data. One of the things that our study illustrates is that it is easy to make a model that matches the pattern of uplift and down-lift that we have observed with *in-situ* and satellite data with very different error sources.

One of our objectives in future field seasons is to obtain more detailed profiles of vertical deformation across the rift over longer time scales to better differentiate which models are appropriate. This will help substantially in formulating more realistic hypotheses about the processes that lead to flexure. Although our modeling efforts have been primitive, our qualitative conclusions are robust. The most reasonable way to produce asymmetric rift uplift and downwards bending is if there are buoyancy forces acting on the rift walls. One possible source of the buoyancy force is if the rift walls are not completely vertical. A mechanism that would produce slanting rift walls is normal faulting. If normal faulting is an important component of ice shelf rifting, then ice shelves may prove to be ideal places to learn about the lithospheric processes that have such long time scales that direct observation is impossible.

Our measurements are the first *in situ* measurements of viscous flexure of ice shelves and demonstrate that GPS can provide sufficient accuracy to study the time dependence of flexure. This is encouraging because it shows that a large detailed network of GPS deployed around rift tips will be able to resolve the small vertical signals expected from plastic deformation. ICESat profiles near the tip of T2 also suggest that there may be some element of plastic deformation in the region near the rift tip, but the temporal and spatial spacing of tracks is too coarse to determine the extent of this deformation. A denser GPS network would, however, be able to directly resolve these small strain rates.

Chapter 6

A Dynamic Stability Criterion for Calving Glaciers and Ice Shelves

> Hypotheses are what we lack the least.
>
> – Jules H. Poincare

Abstract

Motivated by the complexity of the short-time scale behavior of ice fracture, we seek a dynamic stability criterion that predicts the onset of retreat of calving glaciers. In this approach, rather than attempting to model the initiation and propagation of individual fractures, we look for a non-dimensional number that describes the overall glacier stability. Our analysis predicts that calving glaciers will retreat when a non-dimensional number, that we call the "terminus stability number", decreases below a critical value. We show that this criterion is valid for calving glaciers in Alaska, for two glaciers around Greenland as well as for three Antarctic ice shelves (Ross, Amery and Larsen B). The empirical stability criterion presented in this chapter has much in common with classic hydrodynamic stability theory, where the onset of instability is related to non-dimensional numbers that are largely independent of geometry or other situation specific variables.

6.1 Introduction

Up to this point in the dissertation we have focused on improving our knowledge of the iceberg calving process by studying how different external and internal variables influence ice shelf rift propagation. Calving is an important process in all glaciers that terminate in bodies of water, not just ice shelves. While it is common to make distinctions between calving glaciers based on whether they have floating termini (e.g. ice shelves and glacier tongues) or grounded termini (e.g. tidewater and lacustrine glaciers), this obscures the physical similarities and differences in the processes that lead to iceberg detachment in these environments. This results in a wide variety of (occasionally contradictory) calving laws valid only for specific environments (see e.g. Robin, 1979; Hughes and Nakagawa, 1989; Van der Veen, 1996; Scambos et al., 2003). Iceberg calving is a complicated process that occurs over a large range of spatial and temporal scales. Integration the full range of temporal and spatial scales into a a self-consistent mathematical mode presents a formidable challenge. This raises the question of whether it is necessary to understand the details of rift and crevasse propagation to be able to assess the overall health and stability of ice shelves and calving glaciers. Instead, it may be more useful to pursue a "mean-field" theory that seeks a general criterion that predicts whether calving glaciers will retreat.

Some studies have suggested conceptual models of calving (e.g. Van der Veen, 2002). Yet to date a unified criterion for unstable retreat by calving of ice shelves or calving glaciers does not exist. Given the variety of individual environmental and glaciological variables in effect (see e.g. Chapter 4), a unified calving theory may be difficult, or even impossible, to formulate. Regardless of individual differences in glaciological regimes, iceberg calving is a mechanical process that involves the initiation and propagation of fractures. It is therefore likely that the underlying mechanical processes that result in iceberg calving may be similar, regardless of individual differences in glaciologic regimes.

In this chapter we present an alternative approach to those proposed in the literature. Our approach seeks non-dimensional groups that determine whether calving glaciers or ice shelves are stable or will retreat by iceberg calving. We introduce one such group which we call the "terminus stability number" and show that tidewater glaciers and ice shelves tend to retreat when this number decreases below a value of about 5. Glaciers that are close to steady-state or slowly advancing have terminus stability numbers that are larger than 5 while those that are retreating have terminus stability numbers less than 5. This approach has much in common with (and was inspired by), the study of hydrodynamic instabilities (e.g. Chandrasekhar, 1961). These instabilities arise in a variety of complicated phenomena such as the onset of turbulence (Drazin, 2002), the breakup of liquid jets (Chandrasekhar, 1961) and the development of folding and boudinage in rocks (Smith, 1977), all of which involve bifurcations when certain non-dimensional groups exceed a critical value.

There are some variations in terminology when discussing ice shelves versus tidewater glaciers. Throughout this chapter we use the terms "ice front", "calving front" and "terminus" interchangeably, meaning *position of the ice-water cliff*. We also adopt the term "calving glacier" very loosely to encompass the full range of ice bodies that terminate in water, whether floating or not, and independent of whether the glacier terminates in fresh water or the ocean.

6.2 Previous Calving Laws

Most attempts at predicting calving rates from ice shelves and calving glaciers have focused primarily on determining empirical calving laws. For the most part tidewater glaciers and ice shelves have been treated separately, leading to differences in the calving laws proposed. In the next section we review some of the different calving laws proposed for tidewater glaciers and ice shelves.

6.2.1 Tidewater Glaciers

In the case of tidewater glaciers researchers have concentrated on finding correlations between the calving rate and an assortment of variables measured near the terminus. The calving rate, denoted by V_c, is defined as the difference between the flow speed of the glacier at the terminus (V_{term}) and the rate of terminus advance (dL/dt), given as:

$$V_c = V_{term} - \frac{dL}{dt} \tag{6.1}$$

The calving rate is really a combination of both melt and calving processes averaged over the terminus, but for many glaciers mass lost by iceberg calving at the front dominates any melting that may occur. It is this situation that is the focus of our study.

Brown et al. (1982), in a pioneering study, used measurements from 12 tidewater glaciers in Alaska and showed that the variables that best correlated with calving rate are water depth and ice thickness near the terminus. While this correlation has been challenged as either an artifact of too few measurements or a spurious a-causal correlation (Van der Veen, 1996), continued measurements on a variety of glaciers that both terminate in fresh water and the ocean do show a strong correlation between calving rates and water depth (Van der Veen, 2002). Although a correlation exists for both, fresh water calving rates are significantly lower than calving rates from glaciers that terminate in the ocean. The water-depth relationship also holds for glaciers that are both slowly advancing or slowly retreating, but appears to fail for rapidly retreating glaciers such as the Columbia Glacier (Van der Veen, 1996). Thus it may be more diagnostic for glaciers close to steady state than a useful prognostic relationship.

The simple empirical relationship relating calving rate to water depth postulated by Brown et al. (1982) has generated considerable controversy. The problem arises because many of the variables measured by Brown et al. (1982) are not independent. In addition to good correlations between calving rates and both ice thickness and water-depth, there is also a good correlation between terminus velocity and calving rate and there is even a reasonable correlation between ice thickness and water depth . Any meaningful regression would therefore need to statistically “control” for the inter-dependency between all of these variables.

Hughes and Nakagawa (1989) derived an expression for the calving rates from glaciers assuming that the bending moment caused by the difference in hydrostatic and glaciostatic pressure near the terminus was responsible for calving. Unfortunately, the expression they derived was only applicable to glaciers that did not approach floating. Furthermore, the calving rates derived by Hughes and Nakagawa (1989) depended on an known parameter, they called the calving ratio that could only be determined empirically and varied between different glaciers. This makes it difficult to generalize to different glaciers and impossible to apply to ice shelves.

Alternatively Van der Veen (1996) argued that because (by hypothesis) the terminus of temperate glaciers cannot support buoyancy forces, calving is the reaction of the glacier to a change in conditions where the terminus becomes floating. Van der Veen (2002) proposed a height-above-buoyancy criterion in which there is a critical thickness, denoted by H_c:

$$H_c = \frac{\rho_w}{\rho_{ice}}(1 + \frac{H_o}{D}) \tag{6.2}$$

where ρ_i, ρ_w, are the densities of ice and water; D is the depth of the water and H_o is a constant that may vary depending on the glacier but with a value of $\sim$50 m. Thinning of the glacier caused by long-term environmental changes can cause a retreat to a position where the glacier terminus is again grounded. In the view of Van der Veen (2002) it is thinning and local geometry at the bed that determines a stable terminus position. Calving is a response to an unstable terminus position that is controlled by other factors (e.g. climate related thinning) rather than the main factor that causes retreat. This difference is subtle but important because it implies that prolonged climatic changes that lead to thinning are responsible for retreat rather than an advance into deeper water. Van der Veen (2002) presented a compelling argument that showed that retreat of many of the glaciers with documented water-depth relations was preceded by long term mass-deficits.

6.2.2 Ice Shelves

In contrast to tidewater glaciers, significant calving episodes for ice shelves have such long intervening time periods that calving rates are less meaningful. Instead, calving laws for ice shelves have focused on either limitations to their extent due to the geometry of the embayment (e.g. Robin, 1979, Doake et al., 1998) or on thermal limits to their viability (e.g. Mercer, 1978, Doake and Vaughan, 1991, Scambos et al., 2003). For example, Robin (1979) postulated that the position of the ice front was related to lateral stretching transverse to flow. In modeling studies, the most common calving law adopted assumes that ice thickness less than a critical thickness (~ 250 m) is unstable and detaches (Paterson, 1994). While the Larsen B Ice Shelf was subject to strong basal erosion prior to disintegration (Shepherd et al., 2003), there is little theoretical basis for an "ice-thickness" model and little empirical evidence to support it. All of the large icebergs that detached from the Ross and Filchner-Ronne ice shelves in 2000 had thicknesses greater than 350 m (Lazzara et al., 1999).

Doake et al. (1998) used a finite element model to study the stress and strain field of the Larsen B shelf and noted that the ice front was currently near a stable position and should it retreat much more the geometry of the transverse stress field would become tensile rather than compressive (i.e. the "compressive arch") and unstable collapse would ensue. Indeed, several months after their study was published the compressive arch was breached and the ice shelf began to lose mass rapidly (Rott et al., 1996; Scambos et al., 2003). Failure of the compressive arch is a criterion that is related to the isotropic points of the tensor stress field. The isotropic points, regions where the stress field is equal in all directions, are determined by ice thickness and ice shelf geometry. But this theory does not explain why the compressive arch was breached in the first place.

Scambos et al. (2003) presented detailed satellite imagery leading up to the disintegration and argued that surface melt-water enabled extensive fracturing throughout the shelf. They proposed it was this extensive fracturing that precipitated the retreat and proposed a -1.5°C mean summer temperature limit to the viability of ice shelves. In contrast to the assumption of Van der Veen (2002), they argued that the interior of the ice shelf was cold and rejected the possibility that breakup was related to the warmth of the ice. However, not all ice shelves with pronounced surface melting have disintegrated. The Amery Ice Shelf has substantial summer melt seasons with a mean summer temperature that is close to the -1.5°C limit. Melt on the Amery tends to occur upstream where there is still considerable confining stresses preventing the through-penetration of crevasses (Phillips, 1998). Furthermore, there are several ice shelves and floating glaciers that are retreating but either do not have extensive summer melt seasons or have not exceeded the thermal limit (e.g. George VI shelf (Reynolds and Smith, 1981), Amery Ice Shelf (Fricker et al. (2002)). This suggests that while melt water-related processes are important, and provide a compelling explanation for the speed of retreat, but they cannot be the sole factor involved in ice shelf retreat.

6.2.3 Towards a Unified Stability Criterion

While each of the specific calving laws and stability criterion proposed (e.g. height-above-buoyancy, ice thickness, water-depth, meltwater fracturing, geometry of the ice shelf embayment) have had some success in explaining individual retreat events in specific environments, no unifying stability criterion has been put forward. Studies have often focus on geometric or environmental variables rather than on internal glaciological variables. The inception of calving and unstable retreat may be related to environmental "triggers" such as increased melting. Moreover, since fracture of ice is a mechanical process, the state of stress within the ice should play a prominent role in determining when retreat by calving occurs. Although the environments and geometries vary, there are similarities between different calving regimes. For example, Columbia Glacier, Jakobshavn Isbrae and the Larsen B Ice Shelf all thinned prior to the onset of retreat (Van der Veen, 1996; Shepherd et al., 2003; Thomas et al., 2003). They also all displayed increases in terminus velocity either prior to or during retreat (Joughin et al., 2004a; Van der Veen, 1996). This indicates that similar processes may lead to disintegration and rapid retreat. The fundamental challenge of identifying these processes remains.

6.3 Dimensional Analysis

Dimensional analysis is a useful technique for dealing with problems where a mathematical model is not known or is too complicated to obtain analytic insight (Price, 2003; Bohren, 2004). For example, scattering law for small particles, varying as the inverse fourth power of wavelength, was initially derived by Lord Rayleigh using dimensional arguments alone (Strutt, 1871). One approach that we could take is to attempt to formulate a parametric form for the calving rate. In this case, we could write that the calving rate is a function of one or more independent, dimensionless variables (θ_i):

$$V_c = f(\theta_1, \theta_2, ...) \tag{6.3}$$

This equation is identical to the one introduced by Brown et al. (1982) except that we require the arguments of the function to be non-dimensional. The assumption underlying equation 6.3 is that there is an underlying mathematical model that, at least approximately relates calving rates to a set of measurable parameters. If we expand equation 6.3 about a basic state where the terminus position is stable using a standard Taylor series expansion, we find:

$$V_c = V_{term} + \frac{\partial f}{\partial \theta_i}\delta\theta_i \tag{6.4}$$

In steady state the rate of terminus advance must be equal to the calving rate, hence V_{term} is the first term on the right hand side of equation 6.4 in the expansion. Calving rate is rarely measured directly; instead it is almost always calculated using the difference between the terminus velocity and the rate of change of glacier length (equation 6.5). It is therefore convenient to rewrite equation 6.4 in terms of the observed variable, rate of terminus advance.

$$\frac{dL}{dt} = V_{term} - V_c \tag{6.5}$$

and substituting equation 6.5 into equation 6.4 we find:

$$\frac{dL}{dt} = -\frac{\partial f}{\partial \theta_i}\delta\theta_i \tag{6.6}$$

Again, the assumption is that changes in terminus position are related primarily to iceberg calving, not melting. As discussed in section 6.2.1, calving glaciers and ice shelves tend to exhibit two types of behavior, either semi-stable/slowly advancing or rapid retreat. Because of this sharp contrast in behavior, we postulate that there exists a critical value of a dimensionless number that determines a threshold of stability between glaciers that are in steady state or slowly advancing and those that are retreating. This type of bifurcation in behavior is common in hydrodynamic stability analysis with dimensionless numbers like the Reynolds number playing prominent roles in the onset of turbulence (e.g Drazin and Reid (2004)).

Figure 6.1 shows a schematic of a typical geometry for fully grounded calving glaciers. Relevant parameters that might influence calving along with units are shown in Table 6.1. For ice shelves, the terminus would float freely. To take this into account we define the effective water depth (D) as the distance from the base of the ice to surface of the water. For the case of a freely floating terminus, D and H are related by buoyancy:

$$\frac{D}{H} = \frac{\rho_i}{\rho_w} \tag{6.7}$$

where ρ_i and ρ_w are the densities of ice and water respectively. For grounded termini (in section 6.2.1), D is the actual water depth. This definition is adopted to compactly describe the full transition from grounded to floating.

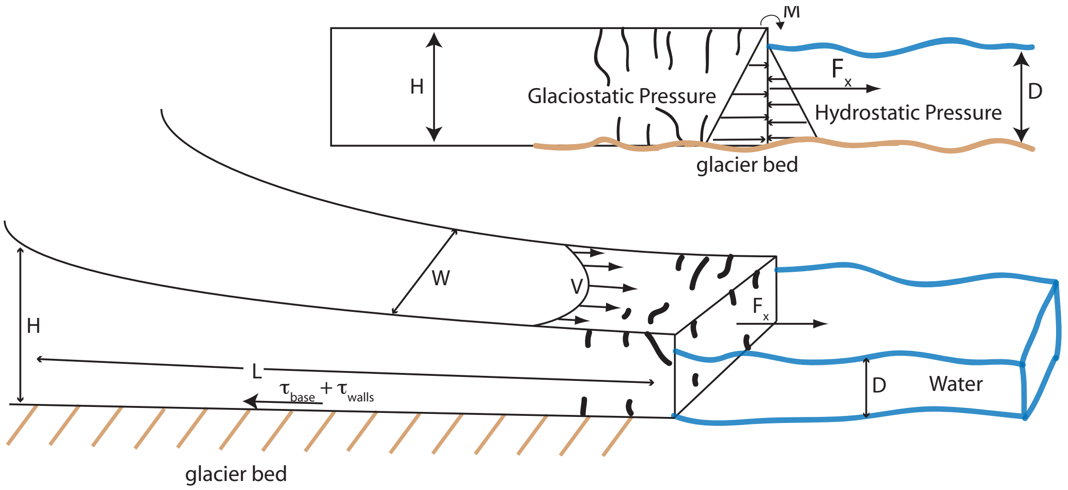

Figure 6.1: Schematic diagram of glacial geometry showing a velocity profile along the width of a characteristic glacier and with relevant spatial scales. Upper frame shows cartoon of longitudinal cross-section of glacier illustrating the force balance at the terminus. The difference in pressure between the ice and water in front of the ice cliff creates a net tensile stress directed outward and a bending moment directed outward. The lower frame shows a sketch of the typical 3D geometry of glaciers. The shape is idealized as most glaciers have parabolic cross-sections and the basal topography is also generally gently sloped.

Table 6.1: Dimensional variables may be relevant to calving and retreat of both calving glaciers and ice shelves. We have re-used L in this table both as the length of the glacier to be consistent with earlier equations and as the unit of length.

D,H,L,W	L	Length
ρ_{ice},ρ_w	ML^3	Density
η	$ML^{-1}T^{-1}$	Viscosity
g	LT^{-2}	Acceleration
U	LT^{-1}	Speed

The geometric parameters of importance are the glacier length (L), width (W) and the ice thickness (H). Important material parameters to consider are the densities of ice and water (ρ_{ice}, ρ_w), the effective viscosity of ice η, assumed to be temperature dependent, and the acceleration due to gravity (g). Finally, the flow speed of the glacier (U) is also likely to be important.

The choice of variables is not unique but, provided all significant variables have been identified (a necessary hypothesis), it provides an orthogonal basis set of non-dimensional groups (Price, 2003). For instance, instead of using velocity as a fundamental parameter, we could have used strain rate which, when combined with a length scale, provides a velocity scale. In this case we chose velocity and width because these are the variables that are directly measured and are available for a larger range of glaciers and ice shelves (the choice of glaciers and ice shelves is discussed in section 6.4). Instead of the strain rate, the second strain rate invariant may be a more appropriate parameter because it is independent of the underlying coordinate system. Unfortunately, there is rarely enough information available to calculate the second strain invariant from available data.

A non-dimensional basis set could be derived from the null-space of the dimension matrix using the formal approach of Price (2003). Instead we exploit two observations: i) thinning has preceded retreat in several cases and ii) terminus velocity generally increases during retreat. This leads us to postulate that a larger ice thickness will increase stability while a faster flow speed will decrease stability. A potential stability parameter that has these two properties is the Argand number (England, 1982):

$$Ar = \frac{\rho_{ice} g H}{\eta(U/L)} \tag{6.8}$$

The Argand number is not an arbitrary choice. It plays a critical role in controlling the occurrence of boudinage (sausage like deformation patterns often seen in rock), folding and modes of rifting in the lithosphere (e.g. Smith, 1977). Again, U/L is a characteristic strain rate. However, Ar does not involve the water depth. We propose a better choice would be the ratio of depth-averaged glaciostatic driving stress at the terminus to the viscous resistive stresses:

$$S = \frac{\rho_{ice} g H \left(1 - \frac{\rho_w}{\rho_{ice}} \left(\frac{D}{H}\right)^2\right)}{\eta \left(\frac{U}{L}\right)} \tag{6.9}$$

Equation 6.9 can be derived by depth-integrating the difference between glaciostatic and hydrostatic pressure at the ice front (see e.g. Van der Veen, 1996). For glaciers with freely floating termini, equation 6.9 reduces to the case of a buoyant slab of ice (substituting equation 6.7 into equation 6.9). A convenient velocity scale is the center-line terminus velocity, V_{term}, although the width-averaged velocity could also be used. We have three choices for length scale, the ice thickness (H), the width (W) or the length of the glacier (L), where we have re-used L to indicate glacier length in additional to a generic length scale. The ratio of terminus velocity to ice thickness would be appropriate for glaciers that are frozen to their beds. Most calving glaciers flow much more rapidly over weak, lubricated beds (Hook, 2005). The length of the glacier is a possibility but for very long glaciers, the terminus is likely to have little influence far upstream and likewise the head of the glacier is unlikely to substantially influence the terminus. The most reasonable length is the width of the glacier. The transverse strain is also often the largest component of strain near the terminus because the velocity is close to zero at the walls and reaches a maximum along the centerline. The width is also related to the maximum iceberg size and seems like a good proxy for reflecting the scale of calving processes. Replacing U with V_{term} and L with W we obtain:

$$S = \frac{\rho_{ice} g H \left(1 - \frac{\rho_w}{\rho_{ice}} \left(\frac{D}{H}\right)^2\right)}{\eta \left(\frac{V_{term}}{W}\right)} \tag{6.10}$$

With the exception of viscosity and ice thickness, all of these variables can be obtained relatively easily for many existing ice shelves and glaciers by using published data. Traditionally, ice is modeled using a power-law stress-strain relationship with a temperature dependence (section 1.4). We are doubtful that such a constitutive relation will continue to hold for highly fractured ice as is prevalent near the terminus. For simplicity, we adopt a linear Newtonian viscosity which we view as the “pre-fracture” viscosity. For temperate tidewater glaciers, we adopt a viscosity of 12.5×10^{12} Pa s. For polar tidewater glaciers, we adopt a viscosity of 13×10^{12} Pa s and for cold ice shelves we use a viscosity of 13.5×10^{12} Pa s. All of these values were calculated using representative values of the strain rate and rate constants from Paterson (1994). The variation of viscosity over several orders of magnitude is the largest uncertainty in the computation of S, although in many regions the ice thickness is also poorly know.

6.4 Data

Our analysis focuses primarily on the Columbia Glacier, Alaska, because it is one of the best studied glaciers in the world. Photogrammetric data have been collected regularly by USGS since 1974, extending up to the year 2000 (Fountain, 1982; Meier, 1985; Krimmel, 2001), along with detailed bathymetry (Rasmussen and Meier, 1982, 1985). This data-set covers periods both prior to and during rapid retreat. We use a weighted nearest neighbor algorithm with a radius of 500 meters to interpolate the velocity, surface elevation and water depth to the terminus (O'Neel et al., 2005). Data were then smoothed using a 2-year median filter. Decreasing the length of the filter below 1-year resulted in a large increase in scatter that obscured the trend. This primarily shows that iceberg calving is a sporadic process and that extracting meaningful trends requires looking at longer term "mean field" averages. We also used the data published by Brown et al. (1982) for 12 Alaskan glaciers (including Columbia Glacier in 1980, prior to retreat). For Greenland, we use data from Howat et al. (2005) for Helheim Glacier and Joughin et al. (2004a) for Jakobshavn Isbrae. We also use our own GPS measurements (see Chapter 2) for the Amery Ice Shelf. Ross data are from Keys et al. (1998). Data for the Larsen B was compiled from Skvarca et al. (2002) and from Scambos et al. (2000).

6.5 Results

To determine whether the terminus stability number is related to glacier retreat, we computed S using the data available for the Columbia Glacier (section 6.4). Figure 6.2 shows the variation of the length of Columbia Glacier over time (upper panel) along with the variation in terminus stability number (lower panel).

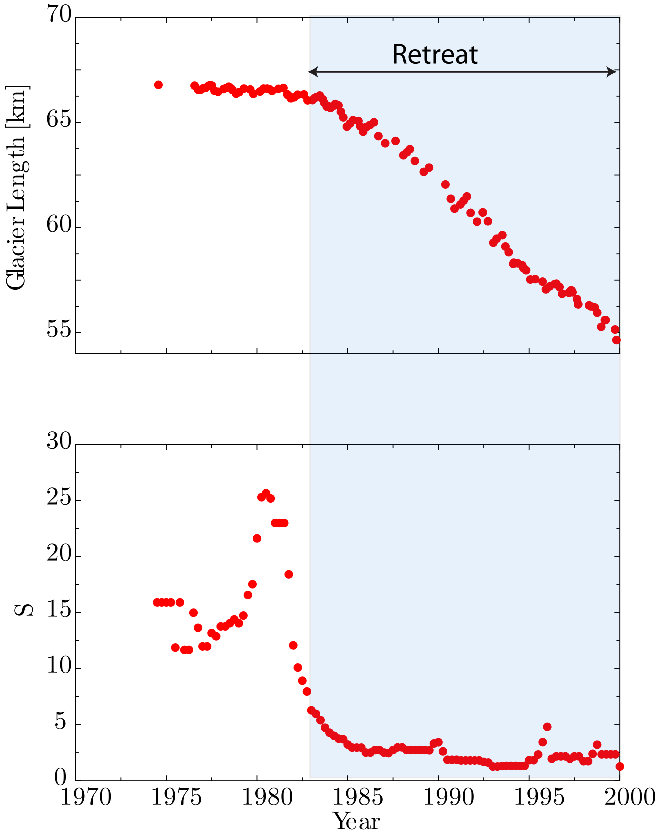

Figure 6.2: Upper panel: Center line length of the Columbia Glacier determined from repeat photogrammetry for the period from 1970 to 2000 (Krimmel, 2001). Lower panel: Terminus stability number over the same period. The interval of retreat is highlighted with a grey box. The onset of retreat corresponds with the time at which the terminus stability number began to drop.

Retreat of the glacier is evident beginning around 1983 (shaded area). We also see that the terminus stability number ranged from 10-25 prior to retreat and then decreased to less than 5 during retreat. This suggests a connection between retreat and our terminus stability number

To examine this connection further, we next looked at the relationship between the terminus stability number and the rate of terminus advance (positive means the glacier is advancing), displayed in Figure 6.3 In addition to the Columbia Glacier (red circles) , we also computed S for the the 12 Alaskan glaciers studied by Brown et al. (1982) (blue squares) , Jakobshaven and Helheim glaciers (green diamonds) and the Ross, Amery and Larsen B ice shelves (purple diamonds). The rate of terminus advance for the Amery, Ross and Larsen ice shelves was set to zero (i.e. we assumed the terminus position was stable). Parameters used for computing the terminus stability number for the two Greenland glaciers and the three Antarctic Ice Shelves are shown in Table 6.2. In addition to the trend with Despite the different environments and geometries there is a consistent pattern evident. Glaciers that are in steady-state or slowly advancing have terminus stability numbers greater than 5. In contrast, all of the glaciers that are retreating have terminus stability numbers that are less than 5. This is strong evidence for a "critical" terminus stability number that marks the transition between stable and unstable behavior.

Not all glaciers with low terminus stabilities are retreating. This may partly reflect uncertainty in our calculation of S (primarily viscosity and ice thickness). Alternatively, it may indicate that glaciers close to steady-state have ice fronts that oscillate between stable and unstable. Prolonged values of small terminus stability numbers may be necessary for sustained retreat. It may also indicate that the terminus stability number decreases prior to retreat. This is supported by subsequent observations of some several of the glaciers observed by Brown et al. (1982). McCarty, was not retreating during the observation period of Brown et al. (1982) but has since started to retreat. Tyndall, perched slightly above the stability limit, began retreating shortly after the measurements of Brown et al. (1982) (Muskett et al., 2003). Meares has also begun retreating while Johns Hopkins was retreating during the measurement period of Brown et al. (1982), but has subsequently started to advance (Sturm et al., 1992). Margerie, Grand Pacific and Harvard all have large terminus stability numbers are also among the rare glaciers that are advancing (Clarke and Holdsworth, 1993). In addition, South Sawyer, Muir and Yale have continued to retreat (Clarke and Holdsworth, 1993). Brown et al. (1982) observed Columbia Glacier prior to retreat (1980) and the value of S

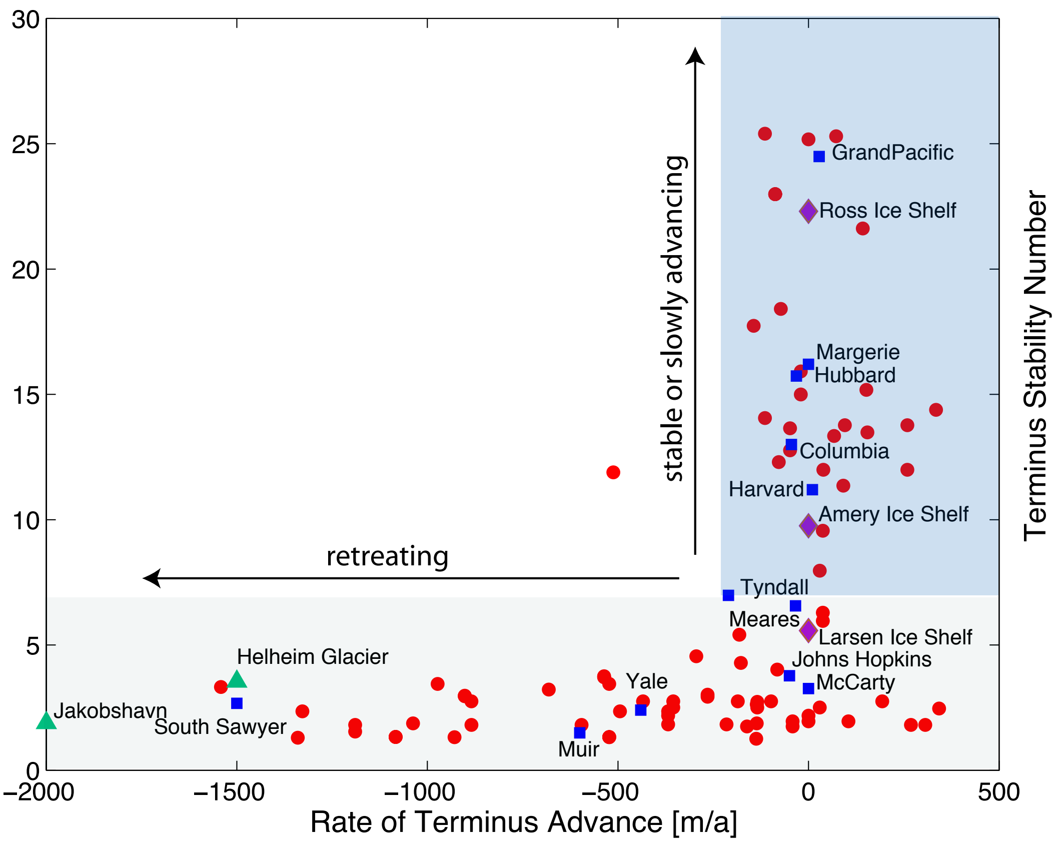

Figure 6.3: Relation between the non-dimensional terminus stability,S, number that we derived and the rate of terminus advance. Upper left and right show the terminus stability number against the glacier length and year for the Columbia Glacier. Lower panel shows the terminus stability number against rate of terminus advance. Red dots are two year median values for the Columbia Glacier. Blue squares show the 12 Alaskan glaciers studied by Brown et al. (1982). Green triangles show Greenland tidewater glaciers. Brown diamonds represent Ross, Amery Ice Shelf and Larsen B ice shelves. Data sources are described in section 6.4

derived from his measurements is consistent with those that we have derived and show that Columbia Glacier was stable at the time.

These additional glaciers, further confirm that there is a critical transition between steady state/slowly advancing to retreat. For glaciers with S larger than about 5, the termini are either stable or slowly advancing. Below 5, all of the rapidly retreating glaciers are confined to the lower region of the curve. The

Table 6.2: Parameters used to compute the terminus stability number for the Amery, Ross and Larsen ice shelves and Helheim Glacier and Jakobshavn Isbrae.

Location	Terminus Velocity (km a^{-1})	Thickness (m)	Width (km)	S
Jakobshavn	10	1000	3	1.9
Helheim	9	625	6	3.5
Larsen B Ice Shelf	1	200	50	5.6
Amery Ice Shelf	1.5	350	75	9.8
Ross Ice Shelf	1	400	100	22.3

Ross Ice Shelf appears to be relatively stable, the Amery Ice Shelf is approaching the critical limit but is still stable, while the Larsen B Ice Shelf had approached the stability limit prior to disintegration. The difference in stability number for the ice shelves is primarily related to the ice thickness for each ice shelf. The Ross Ice Shelf has the greatest ice thickness (450 m) while the Larsen B Ice Shelf (prior to collapse) has the smallest ice thickness (200 m). The Amery Ice Shelf is intermediate (ice thickness is approximately 350 m at the ice front).

6.6 Discussion

6.6.1 Implications

Comparison between tidewater glaciers, ice shelves and temperate tidewater glaciers is difficult because of the varied temperature-dependent viscosities used in these calculations. The terminus stability number for Helheim and Jakobshavn is small (less than 5) for the entire range of viscosities used in these calculations. The only effect of changing the viscosity is to determine how small the terminus stability number becomes. Comparing the Antarctic Ice Shelves to the Greenland and Alaskan tidewater glaciers is more difficult because the value of the terminus stability number depends sensitively on the viscosity. Nonetheless, there is an overall trend, where the Ross Ice Shelf has the highest terminus stability number (most stable), followed by the Amery Ice Shelf and then finally, the Larsen B Ice

Shelf. The terminus stability number of these ice shelves will shift up or down depending on the relative viscosities used, but the overall trend will persist. It is interesting that the Amery Ice Shelf is intermediate to the Ross Ice Shelf and Larsen Ice Shelf. This trend is primarily due to the decreased ice thickness of the Larsen B ice shelf ($\sim$ 200 m) relative to the Amery (350 m) and the Ross (450 m) indicating that enhanced basal or surface melt may push the Amery Ice Shelf much closer to limit of stability (i.e. by decreasing the ice thickness). The Larsen B Ice Shelf had approached the stability limit prior to disintegration. Part of this may be due to decrease in thickness due to enhanced basal melt experienced prior to collapse (Shepherd et al., 2003).

The implication of equation 6.10 is that an increase in ice thickness results in greater stability, while a decrease in ice thickness results in decreased stability. This is consistent with what we know about advancing glaciers. A positive mass balance causes glaciers to thicken and advance. Although the calving rate may increase with ice thickness, this does not necessarily mean that advancing glaciers are more prone to retreat. In a similar way, increasing flow speed at the terminus decreases the stability.

The stability threshold is determined by a non-dimensional number that we call the terminus stability number. The number depends not only on ice thickness and water depth but on the geometry of the glacier. This provides a simple criterion with which the stability of glaciers can be evaluated. If a small retreat or advance of the terminus results in a decrease in S, the retreat will be amplified and lead to catastrophic disintegration. If a small change in terminus position results in an increase in S, then the terminus position will stabilize. Thus, we have:

$$\frac{dS}{dL} > 0 \quad Stable \tag{6.11}$$

$$\frac{dS}{dL} < 0 \quad Unstable \tag{6.12}$$

It also seems possible for terminus advance to be stable and for retreat to be unstable (or vice versa), since retreat tends to increase the stability and since advance may decrease it.

Unlike most stability numbers, where large values indicate greater instability, in this case, as is typically the case with Argand numbers (Smith, 1977), the inverse is true. There are several additional fracture-related parameters that could also be important such as the critical fracture intensity K_c yield strength τ_{yield}, etc. We did not find any non-dimensional numbers that include these parameters that show any interesting trends in behavior.

6.6.2 Force Balance

We have considered several other non-dimensionalizations but none that include both geometrical variables (e.g. glacier width) and glaciological variables (e.g. ice thickness, terminus velocity) show such dramatic behavior as that displayed in Figure 6.3. To investigate the meaning of equation 6.10 further we examined the physical interpretation of each of the terms in equation 6.10. The numerator is, to within a factor of 2, the depth averaged horizontal force (F_x) acting on the ice wall (see Figure 6.1):

$$F_x = \frac{1}{H}\int_0^H \rho_{ice} g z dz - \int_0^D \rho_w g z dz = \rho_{ice} g H \left[1 - \frac{\rho_w}{\rho_{ice}}\left(\frac{D}{H}\right)^2\right] \tag{6.13}$$

The denominator is a measure of the viscous resistive stresses within the ice. The driving stress (F_x) will be partly balanced by basal resistance to flow from friction along the base (τ_{base}) and by lateral shear along the margins of the embayment or fjord (τ_{walls}). Consider a force balance on a horizontal slab of ice, then integrate from the ice front ($x = 0$) up glacier a distance x_f :

$$\tau_{visc} = F_x - (\int_0^{x_f} \tau_{base} dx + \int_0^{x_f} \tau_{walls} dx) \tag{6.14}$$

For glaciers that are frozen to their bed, the driving stress will be almost entirely balanced by resistance at the bed, leading to very low calving rates and making it unlikely that these glaciers can undergo rapid retreat. On the other hand, for glaciers that are sliding over a weak, lubricated bed, the resistance at the base will be low and sensitive to the pore pressure (P_{pore}) in underlying till. A common parameterization of the sliding law (Iken and Bindschadler, 1986) is:

$$\tau_{base} = \beta V^{m} \left(\rho_{ice} g H - P_{pore}\right)^{q} \tag{6.15}$$

where m and q are exponents usually chosen between 1 and 3, β is a constant and V is the velocity at the base. Close to the terminus the pore pressure will be close to hydrostatic:

$$P_{pore} = \rho_w g D \tag{6.16}$$

An increasing water depth (D) will lead to a reduction in basal resistance and to a decrease in S. If the terminus approaches floatation the basal resistance (τ_{base}) approaches zero. More of the driving stress will then by accommodated by an increase in τ_{visc}. This in turn would result in an increase in the terminus velocity and increased calving instability.

6.6.3 To Float or Not to Float

For ice shelves the basal resistance will be negligible. In this case, the driving force will be entirely balance by viscous resistive stresses and shear stresses along the margins. For an unconfined ice shelf (or iceberg) the force balance will be entirely between the driving force (buoyancy) and viscous resistive stresses. This implies that unconfined ice shelves are not stable, a result in agreement with the absence of unconfined ice shelves. Further interpreting this result we can also deduce that as an ice shelf protrudes beyond its embayment, lateral shear from the margins will decrease, resulting in a decrease in the terminus stability number. The ice shelf also thins as it advances, further decreasing the stability. Eventually, the terminus stability number will decrease beyond the critical terminus stability number and one or several icebergs will detach returning the ice shelf front to a stable position.

The terminus stability number may also explain why there are no temperate tidewater glaciers. It is normally assumed that temperate ice cannot support buoyancy forces (Van der Veen, 1996). The reduction in basal resistance as the calving front becomes buoyant increases the calving instability. Temperate tidewater glaciers rarely, if ever, have floating termini. This has led some to suggest that a floating terminus is unstable for these glaciers. Temperature alone is insufficient to explain the existence of floating termini because there are fully floating termini and grounded calving glaciers in both Antarctica and Greenland. Our results suggest that a combination of ice thickness, back-pressure from pinning points and lateral shear from the walls (all of which increase S) are necessary to enable a calving glacier to become buoyant.

6.6.4 What Causes the Onset of the Instability?

Unlike other calving “laws” that relate the discharge of icebergs to parameters such as the ice thickness or water depth, our criterion does not provide a rate of iceberg production and calving rates could be relatively high without development of an instability. Instead, what we predict is the onset of retreat. This raises the question: what physically controls the onset of the instability? It could be that a decrease in S is merely diagnostic that retreat is occurring, which makes it useful for assessing the health of glaciers but less useful in modeling studies. Figure 6.2 shows that S decreased prior to the onset of rapid retreat of Columbia Glacier. One explanation for this might be that the glacier had thinned. This would suggest that climate may be one of the driving factors, as suggested by Van der Veen (2002). Two other parameters that might have decreased are basal resistance or shear from the margins, thus promoting the instability. Of course, the trend may be linked to a combination of all three. Once retreat begins, the stability is also related to the bed geometry (this affects D) and may determine whether retreat is unstable or stable. For example, if the glacier retreats (perhaps randomly) into deeper water, this would result in a decrease in S that would promote further retreat. On the other hand, if the glacier retreated into shallower water S would increase and this might stabilize the terminus position.

6.6.5 Comparison with Other Calving Laws and Stability Criteria

It is informative to compare our criterion to the other proposed calving laws proposed.

Water depth model

The water-depth model has much in common with our terminus stability number. Both calving laws were determined empirically. The major difference between the two is that our terminus stability number also takes into account a number of other variables, such as ice thickness and glacier width. Moreover, our criterion can also be applied to glaciers with floating termini. When applied to tidewater glaciers, both models yield qualitatively similar results. In the water-depth model a retreat of the terminus into deeper water, results in an increased calving rate. The increased calving rate results in an increased rate of retreat. The stability of tidewater glaciers is thus determined by bed geometry. In our approach, a retreat into deeper water will also decrease the terminus stability number by increasing D in equation 6.10. There is an additional major difference between the two approaches. Our terminus stability number also predicts that other also influence retreat. Like the water-depth model, a retreat of the terminus into deeper water can lead to rapid retreat. Unlike the water-depth model there are other mitigating factors. For example, a retreat into a narrower channel might increase lateral resistance from the margins preventing further retreat.

Height-above-buoyancy

For grounded termini, our criterion results in a qualitatively similar behavior to of the height-above-buoyancy model. The stability parameter will decrease as buoyancy is approached - perhaps explaining the rarity of floating termini for temperate glaciers. In our theory the terminus can become freely floating with an appropriate combination of geometry and ice thickness (6.6.3).

Embayment geometry

Both Robin (1979) and Sanderson (1979) postulated that lateral stretching transverse to flow may be the primary cause of iceberg calving. If the ice is required to maintain contact with the embayment walls then a critical divergence angle (denoted by ψ_{max} for the margins can be derived (Paterson, 1994):

$$tan(\psi_{max}) = \frac{1}{9}\frac{W}{V_{term}}\left(\frac{\rho_{ice} g H(1-\frac{\rho_{ice}}{\rho_w})}{2\bar{B}}\right)^3 \tag{6.17}$$

Where $\bar{B}$ is the depth-averaged rate constant in the power-law rheology for ice (section 1.4) and all other terms are defined as before. Like the terminus stability number, this number is non-dimensional. This theory predicts that ice shelves that are thin and have a high terminus velocity will be more stable. For some ice shelves this may be a useful criterion, especially if the ice is frozen to margins that diverge rapidly enough that the ice is pulled apart by lateral strain. It is less successful at explaining calving from fast flowing glaciers that exist in narrow fjords. In contrast, our analysis predicts that glaciers that are thinner and have faster flow speeds will be more unstable. This is in better agreement with observations of Jakobshavn and Columbia glaciers. Both sped up substantially prior to and during retreat (Joughin et al., 2004a; Van der Veen, 1996).

Bending Moment Induced Calving

The expression Hughes and Nakagawa (1989) derived for the calving rate:

$$U_c = \frac{3\rho_{ice} g H^4 \theta}{\eta C^2}\left(1 - \frac{\rho_w}{\rho_{ice}}\left(\frac{D}{H}\right)^2\right) \tag{6.18}$$

can be re-arrange into a form similar to equation 6.10:

$$\frac{C^2}{H^2} = \frac{3\rho_{ice} g H \theta}{\eta \frac{U_c}{H}} \tag{6.19}$$

The calving ratio is non-dimensional. Absorbing all of the constants into a single term, K and denoting the non-dimensional calving ratio by Π we find:

$$\Pi = K\frac{\rho_{ice} g H \theta}{\eta \frac{U_c}{H}}\left(1 - \frac{\rho_w}{\rho_{ice}}\left(\frac{D}{H}\right)^2\right) \tag{6.20}$$

Although Hughes and Nakagawa (1989) intended to solve for the calving rate, comparing equation 6.10 with equation 6.20 we find the two approaches yield expressions that are similar. The difference between the two is the strain rate in the denominator. In our terminus stability number we use the ratio of the terminus velocity to the width. In contrast, we see that equation 6.20 uses the ratio of the calving rate to the ice thickness. We have already argued that the calving rate is comparable in magnitude to the terminus velocity (section 6.2.1). The primary difference is that we used the width of the glacier while Hughes and Nakagawa (1989) used the ice thickness as the length scale. Equation 6.20 was derived for glaciers frozen to their beds, in which case, vertical shear would be the dominant mode of deformation. We considered the case of glaciers that were close to buoyant and had little traction along the bed. The two approaches are therefore quite similar and ultimately yield similar results.

Meltwater Related Fracturing

Large quantities of surface meltwater facilitate intense hydro-fracturing of the ice shelf, a factor known to be important in the disintegration of the Larsen B Ice Shelf. This led Scambos et al. (2003) to proposed a -1.5 °C thermal limit to the viability of ice shelves. The thermal limit, however, is only related to atmospheric temperature. In contrast, our terminus stability number is relates solely to internal variables such as ice thickness and geometrical variables. These variables are important in determining the state of stress within the ice shelf, but are only indirectly related to climate (i.e. melting could decrease ice thickness, which would decrease the stability). Furthermore, the meltwater controlled disintegration proposed by Scambos et al. (2003) cannot be easily applied to temperate tidewater glaciers, where the atmospheric temperature often exceeds the -1.5 °C thermal limit. There are additional problems in applying the thermal limit of Scambos et al. (2003) to other ice shelves. There are also ice shelves with significant melt during the summer that have not disintegrated and have not developed the intensive rifting seen on sections of the Larsen prior to collapse. For example, the Amery Ice Shelf, experiences large quantities of surface melt during the summer. In contrast to the Larsen B Ice Shelf, melt on the Amery Ice Shelf occurs hundreds of kilometers upstream where considerable confining stresses prevent the through-penetration of crevasses. Conversely, retreat also can occur for ice shelves that do not experience substantial surface melting. Rapidly changing areas like Thwaites and Pine Island glaciers in the Amundsen Sea sector of Antarctica have undergone substantial basal melt (Shepherd et al., 2001) along with moderate retreat of their terminus positions unaccompanied by increased surface melt. This implies that although meltwater-related processes are important, they are not the only factor involved in ice shelf retreat and that a more consistent criteria needs to incorporate glaciological variables as well, a point noted by Scambos et al. (2003). At the same time, our terminus stability number does not include the effect of meltwater at all. We propose that these two processes are complementary. Meltwater enables rapid retreat in regions that have low terminus stability numbers. These regions are, in a sense, primed for disintegration. This suggests that meltwater is not the cause of retreat, but instead the ingredient that enables rapid disintegration. The availability of meltwater may then be the rate limiting factor rather than the cause of retreat.

6.6.6 The Role of Meltwater - a rate limiting factor?

Meltwater is clearly an important factor in the disintegration of both glaciers and ice shelves (Scambos et al., 2003). Meltwater affects mainly calving through two processes: (i) Meltwater percolates to the base of the glacier and lubricates the base, leading to a reduction in basal resistance and increased velocities; (ii) Surface melt enables fractures to penetrate more deeply into the ice. Although the formation of melt ponds may be a necessary condition for ice shelf retreat, it is not sufficient. We suggest that meltwater provides the necessary ingredients for rapid disintegration, but that disintegration is preceded by a prolonged reduction in the terminus stability number below the critical value. Although speculative, if correct, the melting and thinning that occurred prior to disintegration of Larsen B (Shepherd et al., 2003) would be just as important as the surface melting. Abundance of surface melt on these ice shelves enabled much more rapid retreat than otherwise possible. Disintegration could be one end of a spectrum of scenarios in which slow decay dominated by basal melting lies at one end of the spectrum and rapid retreat by meltwater related fracture at the other end of the spectrum. This situation is particularly relevant because the Ross and Filchner-Ronne Ice Shelves lie in embayments sufficiently far south where atmospheric temperatures are not likely to rise sufficiently to enable pervasive surface melt. Therefore retreat and disintegration of these ice shelves is not likely to be caused by surface-melt related processes. Likewise, the rate of retreat of the Columbia Glacier could also be partially related to meltwater. In addition to enabling fractures to penetrate more deeply, surface melt that penetrates to the base of the glacier lubricates the bed and enabling higher flow speeds.

6.6.7 Heinrich Events

Our empirical terminus stability numbers provides a potential explanation for some well known paradoxes. For example, a glaciological explanation for Heinrich events (the sudden discharge of massive armadas of icebergs from the Laurentide Ice Sheet into the North Atlantic), remains a formidable glaciological problem (Hulbe et al., 2004). One explanation for these events is that they are caused by a surging instability in the Laurentide Ice Sheet (MacAyeal, 1993). Clarke et al. (1999) attempted to develop a numerical model of Heinrich events. They assumed that calving rates from the ice margins are proportional to both ice thickness and water depth (e.g (Clarke et al., 1999)):

$$V_c = kDH \tag{6.21}$$

A larger constant of proportionality (k) results in higher calving rates (a so-called "strong" calving law) while a lower constant of proportionality results in lower calving rates (a "weak" calving law). They showed that low calving rates are necessary to enable the ice sheet to "grow" rapidly enough to match reconstruction estimates (Clarke et al., 1999). The weak calving law could not reproduce the volume of icebergs necessary to match the sedimentary record. They therefore concluded that a weak calving law was necessary for the early stages of ice sheet formation but they also needed an abrupt transition to a more vigorous calving law to generate enough icebergs. The were not able to identify a mechanism that enabled a switch from a weak to a strong calving law except by a "Hand-of-God" approach (Clarke et al., 1999). Our terminus stability parameter provides the criterion for just such a switch. This remains speculative but our terminus stability number provides an objective criterion that determines when to switch between weak and strong calving laws in numerical models.

6.7 Conclusions

We have demonstrated that an empirical stability threshold valid for temperate and polar tidewater glaciers as well as for Antarctic ice shelves. A non-dimensional number, S that is related to the ice thickness, water depth, terminus velocity, glacier width as well as densities of ice and water, defines whether the terminus is stable. For large values of S, the terminus is stable and the glacier may even advance. When S decreases below a critical value retreat ensues. Like other hydrodynamic instabilities, S controls the transition between a stable ice front to that of an unstable retreat. This relationship appears to hold for a dozen tidewater glaciers in Alaska, as well as for Helheim glacier in Greenland and Jakobshavn Isbrae in Greenland. Application to ice shelves is promising, showing a similar trend, with the Ross Ice Shelf quite stable, the Amery Ice Shelf less stable but still above the critical transition and the Larsen B Ice Shelf (several years prior to retreat) having approached critical stability.

While a well posed and general mathematical model for calving remains elusive, the empirical analysis that we have presented provides a simple method which can be used to predict when unstable retreat will occur. Our analysis does not predict a rate of iceberg production as some other calving laws have attempted to do. Instead we suspect that there are additional rate limiting mechanisms such as the availability of meltwater that determine iceberg production. We believe that results show that this analysis is promising but there is a clear need to demonstrate that it works on a larger variety of glaciers and ice shelves than the ones we have presented in this chapter.

Although we have considered a single stability parameter, the state space of stable calving glacier configurations may depend on more than one parameter, possibly including the atmospheric temperature and basal temperature. As atmospheric and oceanic warming trends continue, it is likely that hypotheses of ice shelf stability will be put to the test. For example, the Amery Ice Shelf sits much further north than the colder Ross and Filchner ice shelves with summer melt comparable to that of the Larsen Ice Shelf prior to collapse.

Satellite and airborne remote sensing facilitate measurements of terminus position, glacial geometry and ice thickness. One of the strengths of the stability analysis presented here is that the current stability of glaciers can be assessed with a calculation so simple that it can be done very easily.

Chapter 7

Conclusions and Future Work

> In all science, error precedes the truth, and it is better it should go first than last.
>
> – Hugh Walpole

7.1 Overview

The primary aim of this dissertation was to improve our knowledge of the processes and mechanisms involved in iceberg calving. Our contribution can be divided into five different areas:

i. We have demonstrated that the combination of GPS and seismometers deployed in a densely spaced network provides valuable information about rift propagation. While this type of methodology has been routinely applied to earthquake studies, we showed that it was also useful for ice shelf rift propagation and enabled us to detect fast-time scale transients associated with rift propagation.

ii. Using this methodology, we have found that rift propagation is episodic, suggesting that an analogy with earthquake mechanics may be appropriate. This leads us to propose that, in addition to using observational methodologies typically applied to earthquake studies, the rich literature of theoretical earthquake studies also provides a conceptual framework from which models of ice shelf rifting can be constructed.

iii. In a similar vein, we have shown that ice shelf rifting is a three-dimensional process, with uplift on the northern rift wall and downward bending of the southern rift wall. We have interpreted these patterns as evidence of normal faulting, similar to what is observed in lithospheric rifting.

iv. We have shown that short-term environmental variables such as tides and winds have very little effect on ice shelf rift propagation, indicating that the primary driver of ice shelf rift propagation is the internal glaciological stress within the ice shelf. While it has been suspected that rift propagation is driven by glaciological stress, our contribution is demonstrating that is also insensitive to a range of short-term environmental variables.

v. We have devised an empirical stability criterion and shows that it is valid not only ice shelves but for all calving glaciers that terminate in bodies of water. This approach is novel in that, rather than consider the details of individual fracture initiation and propagation in different glaciological environments; we looked for unifying principles that are common to all calving bodies of ice.

7.2 Summary

Chapter 2

In Chapter 2 we demonstrated that rift propagation episodic. This survey presented the first *in situ* measurements of ice shelf rift propagation along with verification that rift propagation is seismic. These measurements reveal that propagation occurs in episodic bursts, which were identified based on swarms of seismicity accompanied by rapid rift widening. The bursts last approximately 4 hours and are separated by 10-24 days.

Chapter 3

Chapter 3 presented results from two follow up field seasons (2004-05 and 2005-06). We detected four swarms and confirmed that rift propagation is episodic in nature. The detailed seismic network deployed also enables us to map the seismicity that originated from the rift tip. The spatial trends showed a strong clustering along the rift axis extending far behind the rift tip. This showed that the seismicity associated with rifting was diffuse and scattered along several kilometers up the axis. We also showed that the relative magnitudes of events have a power-law distribution similar to what is observed for earthquakes. Comparison between different field seasons showed a decrease in the number of episodic bursts observed. We interpreted the decrease to indicate that rift propagation is slowing down but a prolonged time series is necessary to determine if the variations we see aren't due to natural variability that our short sampling campaigns do not capture.

Chapter 4

In Chapter 4 we used the combined results from three years of field work to re-address the question of whether environmental variables influence rift propagation. Using our data in combination with automatic weather station data we showed that the timing of rift propagation events does not correspond to high winds or tides. Because the arrival of the tsunami generated by the December 26th Sumatra earthquake coincided with our observation period we were also able to show that the tsunami also did not trigger rift propagation. We used the absence of evidence for environmental influences to conclude that the most likely driving force was the internal gravitational stress within the ice shelf. Estimates of the magnitudes of the environmental stresses, however, indicated that environmental variables will become increasingly important as the point of iceberg detachment approaches.

Chapter 5

Chapter 5 is the final chapter devoted to the field measurements made. In this chapter we showed that the northern side of the rift is uplifting relative to the southern side. Because the character of the uplift is reminiscent of flexure associated with normal faulting, we modeled the deformation as viscous beam bending. We compared the analytic solution first derived for lithospheric subduction and found good quantitative agreement.

Chapter 6

While Chapters 2-5 provided the first measurements of rift propagation, it was not possible to relate these measurements to the effect of climate on iceberg calving. In Chapter 6 we took a markedly different approach and used dimensional analysis to determine a non-dimensional group that determines whether an ice shelf or calving glacier is stable. Using data from several Alaskan tidewater glaciers, two Greenland glaciers and three Antarctic ice shelves we demonstrated that when this non-dimensional number that we called S_{term} decreased below a critical value of about 5, calving bodies began rapid retreat.

7.3 Synthesis and Future Work

The work presented in this dissertation contains the first ever detailed *in situ* field measurements of rift propagation on an ice shelf. We have demonstrated that the combination of GPS and seismometers provide valuable information about rift propagation such as the episodic bursts of propagation we detected. These short time-scale phenomena are not resolved by satellite imagery. However, the combination of long-term monitoring with satellite imagery and detailed field studies need to be more tightly integrated to include a greater overlap between time scales. The most feasible way of doing this is to extend our field sites to semi-permanent locations that operate continuously for several years. While this is currently technologically challenging, improvements in recording capacity and low-power systems will make this feasible within the next couple of years.

In a broad sense, the work presented here has advanced our knowledge of iceberg calving from ice shelves substantially. We now know that rift propagation is episodic, but more importantly we know that environmental variables play a minimal role in driving rift propagation. This contradicts some theories that increased storminess of the oceans may result in increased calving rates. Determining the driving primary drivers of rift propagation is essential for all future modeling studies.

While we have accomplished most of the objectives outlined in the introduction, two of the questions that we sought to address require further attention. The first is how rift propagation rates vary over time. We have some evidence that they do and have suggested that this variation is related to periods when rifts propagate into suture zones between ice streams. However, the intervals of our measurements are too short to make any definite statement. Answering this question requires developing instrumentation that is capable of recording semi-continuously over entire annual cycles. In addition it is necessary to contrast the behavior on the Amery Ice Shelf with rifts on other ice shelves. The second question requiring further study is the effect of climate change on iceberg calving. We hope that continued detailed measurements of rift propagation will continue to advance our knowledge of the mechanism and processes such that realistic models of rifting can be incorporated into future numerical models. However, our knowledge of the processes is not yet complete enough that this can be accomplished. One of the goals of the last chapter (Chapter 6) was to take a different approach to this problem. The stability analysis is promising but further confirmation requires a more complete inventory of advancing and receding glaciers. It is also an empirical estimate without a theoretical basis and as such is unsatisfying. We have begun to develop a physical theory based on perturbation theory that provides some theoretical grounding, but this remains a goal for future research.

References

Allen, R., 1982: Automatic phase pickers: Their present use and future prospects. *Bulletin of the Seismological Society of America*, **72**(6 B).

Alley, R. B., Dupont, T., Parizek, B., and Anandakrishnan, S., 2005: Access of surface meltwater to beds of sub-freezing glaciers: preliminary insights. *Annals of Glaciology*, **40**(1), 8–14.

Arendt, A., Echelmeyer, K., Harrison, W., Lingle, C., and Valentine, V., 2002: Rapid Wastage of Alaska Glaciers and Their Contribution to Rising Sea Level. *Science*, **297**(5580), 382–386.

Atkinson, B. K., and Meredith, P. G., 1987: The theory of subcritical crack growth with applications to minerals and rocks. In *Fracture Mechanics of Rock*, editor B. Atkinson, 111–166. Academic, San Diego, California.

Bamber, J. L., Vaughan, D. G., and Joughin, I., 2000: Widespread Complex Flow in the Interior of the Antarctic Ice Sheet. *Science*, **287**, 1248–1250.

Bassis, J. N., Coleman, R., Fricker, H. A., and Minster, J. B., 2005: Episodic propagation of a rift on the Amery Ice Shelf, East Antarctica. *Geophysical Research Letters*, **32**, 6502. doi:10.1029/2004GL022048.

Bindschadler, R. A., King, M. A., Alley, R. B., Anandakrishnan, S., and Padman, L., 2003: Tidally Controlled Stick-Slip Discharge of a West Antarctic Ice Stream. *Science*, **301**, 1087–1090. doi:10.1126/science.1087231.

Bock, Y., Nikolaidis, R., de Jonge, P. J., and Bevis, M., 2000: Instantaneous geodetic positioning at medium distances with the global positioning system. *Journal of Geophysical Reseach*, **105**, 28223–28254.

Bohren, C., 2004: Dimensional analysis, falling bodies, and the fine art of not solving differential equations. *American Journal of Physics*, **72**(4), 534–537.

Bond, G., and Lotti, R., 1995: Iceberg discharges into the north atlantic on millenial time scales during the last glaciation. *Science*, **267**, 1005–10.

Broberg, K., 1999: *Cracks and Fracture*. Academic Press.

Brown, C. S., Meier, M. F., and Post, A., 1982: Calving speed of Alaska tidewater glaciers, with applications to Columbia Glacier. *U.S. Geological Survey Professional Paper*, **1258-C**, 13p.

Budd, W., 1966: The dynamics of the Amery Ice Shelf. *Journal of Glaciology*, **6**(45), 335–358.

Bullard, E., 1936: Gravity Measurements in East Africa. *Philosophical Transactions of the Royal Society of London. Series A, Mathematical and Physical Sciences*, **235**(757), 445–531.

Chandrasekhar, S., 1961: *Hydrodynamic and hydromagnetic stability*. International Series of Monographs on Physics, Oxford: Clarendon, 1961.

Clarke, G., and Holdsworth, G., 1993: Satellite Image Atlas of Glaciers of the World - Glaciers of North America. Inv. Rpt. 1386-J-1, USGS Water-Resource.

Clarke, G., Marshall, S., Hillaire-Marcel, C., Bilodeau, G., and Veiga-Pires, C., 1999: A Glaciological Perspective on Heinrich Events. In *Mechanisms of Global Climate Change at Millennial Time Scales*, editors P. Clark, R. Webb, and L. Keigwin, 394.

De Angelis, H., and Svarkca, P., 2003: Glacier Surge after Ice Shelf Collapse. *Science*, **299**, 1560–1562.

De Bremaecker, J., 1977: Is the oceanic lithosphere elastic or viscous? *Journal of Geophysical Research*, **82**(B14), 2001–2004.

Debenham, F., 1965: The Glacier Tongues of McMurdo Sound. *The Geographical Journal*, **131**(3), 369–371.

Doake, C., and Vaughan, D., 1991: Rapid disintegration of the Wordie Ice Shelf in response to atmospheric warming. *Nature*, **350**, 328–330.

Doake, C. S. M., Corr, H. F. J., Rott, H., Skvarca, P., and Young, N. W., 1998: Breakup and conditions for stability of the northern Larsen Ice Shelf, Antarctica. *Nature*, **391**, 778. doi:10.1038/35832.

Domack, E., Duran, D., Leventer, A., Ishman, S., Doane, S., McCallum, S., Amblas, D., Ring, R., Gilbert, R., and Prentice, M., 2004: Stability of the Larsen B Ice Shelf on the Antarctic Peninsula during the Holocene epoch. *Nature*, **436**, 681–685.

Drazin, P. G., 2002: *Introduction to Hydrodynamic Stability*. Introduction to Hydrodynamic Stability, by P. G. Drazin, pp. 276. ISBN 0521804272. Cambridge, UK: Cambridge University Press, September 2002.

Drazin, P. G., and Reid, W. H., 2004: *Hydrodynamic Stability*. Hydrodynamic Stability, by P. G. Drazin and W. H. Reid, pp. 626. ISBN 0521525411. Cambridge, UK: Cambridge University Press, September 2004.

Earle, P., and Shearer, P., 1994: Characterization of global seismograms using an automatic-picking algorithm. *Bull. Seism. Soc. Am*, **84**(2), 366–376.

England, D., P. McKenzie, 1982: A thin viscous sheet model for continental deformation. *Geophysical Journal of the Royal Astronomy Society*, **73**, 523–532.

Fastook, J. L., and Schmidt, W. F., 1983: Finite element analysis of calving from ice fronts. *Annals of Glaciology, vol.3, pp.103-106*, **3**, 103–106.

Floyd, J., Tolstoy, M., Mutter, J., and C.H., S., 2002: Seismotectonics of mid-ocean ridge propagation in hess deep. *Science*, **298**, 1765–1768.

Fountain, A., 1982: *Columbia Glacier Photogrammetric Altitude and Velocity: Data Set (1957-1981)*. The Survey; Open-File Services Section, Western Distribution Branch, US Geological Survey, distributor.

Fricker, H., Young, N., Allison, I., and Coleman, R., 2002: Iceberg calving from the Amery Ice Shelf, East Antarctica. *Annals of Glaciology*, **34**(1), 241–246.

Fricker, H. A., Bassis, J. N., Minster, B., and MacAyeal, D. R., 2005a: ICESat's new perspective on ice shelf rifts: The vertical dimension. *Geophysical Research Letters*, **32**, 23. doi:10.1029/2005GL025070.

Fricker, H. A., Young, N. W., Coleman, R., Bassis, J. N., and Minster, J.-B., 2005b: Multi-year monitoring of rift propagation on the Amery Ice Shelf, East Antarctica. *Geophysical Research Letters*, **32**, 2502. doi:10.1029/2004GL021036.

Gillard, D., Rubin, A., and Okubo, P., 1996: Highly concentrated seismicity caused by deformation of Kilauea's deep magma system. *Nature*, **384**, 343–346.

Glen, J. W., 1952: Experiments on the deformation of ice. *Journal of Glaciology*, **2**, 111–114.

Goldsby, D., and Kohlstedt, D., 2001: Superplastic deformation of ice: Experimental observations. *Journal of Geophysical Research*, **106**(B6), 11017–11030.

Goodman, D. J., Wadhams, P., and Squire, V. A., 1980: The flexural response of a tabular ice island to ocean swell. *Annals of Glaciology*, **1**, 23–27.

Grosfeld, K., and Sandhäger, H., 2004: The evolution of a coupled ice shelf–ocean system under different climate states. *Global and Planetary Change*, **42**, 107–132.

Heinrich, H., 1988: Origin and consequences of cyclic ice rafting in the northeast atlantic ocean during the past 130,000 years. *Quaternary Research*, **29**, 143–52.

Hobbs, P., 1974: Ice physics. *Oxford: Clarendon Press, 1974*.

Holdsworth, G., and Glynn, J. E., 1981: A mechanism for the formation of large icebergs. *Journal of Geophysical Research*, **86**, 3203–3209.

Hook, R. L., 2005: *Principles of Glacier Mechanics*. Cambridge University Press, Cambridge, second edition edition.

Howat, I. M., Joughin, I., Tulaczyk, S., and Gogineni, S., 2005: Rapid retreat and acceleration of Helheim Glacier, east Greenland. *Geophysical Research Letters*, **32**, 22502. doi:10.1029/2005GL024737.

Hughes, T., 1983: On the disintegration of ice shelves: The role of fracture. *Journal of Glaciology*, **29**(101), 98–117.

Hughes, T., 1986: The Jakobshanvs effect. *Geophysical Research Letters*, **13**, 46–48.

Hughes, T., 1992: Theoretical calving rates from glaciers along ice walls grounded in water of variable depths. *Journal of Glaciology*, **38**, 282–294.

Hughes, T., and Nakagawa, M., 1989: Bending shear: the rate-controlling mechanism for calving ice walls. *Journal of Glaciology*, **35**, 260–266.

Hulbe, C. L., and MacAyeal, D. R., 1999: A new numerical model of coupled inland ice sheet, ice stream, and ice shelf flow and its application to the west antarctic ice sheet. *Journal of Geophysical Research*, **104**(B11), 25,349–25,366.

Hulbe, C. L., MacAyeal, D. R., Denton, G. H., Kleman, J., and Lowell, T. V., 2004: Catastrophic ice shelf breakup as the source of Heinrich event icebergs. *Paleoceanography*, **19**, 1004. doi:10.1029/2003PA000890.

Hulbe, C. L., Rignot, E., and Macayeal, D. R., 1998: Comparison of ice-shelf creep flow simulations with ice-front motion of Filchner-Ronne Ice Shelf, Antarctica, detected by SAR interferometry. *Annals of Glaciology, vol.27, pp.182-186*, **27**, 182–186.

Hutter, K., 1983: *Theoretical Glaciology*. D. Reidel Publishing Company, Dordrecht, Holland.

Iken, A., and Bindschadler, R., 1986: Combined measurements of subglacial water pressure and surface velocity of Findelengletscher, Switzerland: conclusions about drainage system and sliding mechanism. *Journal of Glaciology*, **32**(110), 101–119.

Ito, A., 1985: High resolution relative hypocenters of similar earthquakes by cross-spectral analysis method. *Journal of Physics of the Earth*, **33**(4), 279–294.

Jacobs, S., Helmer, H., Doake, C., Jenkins, A., and Frolich, R., 1992: Melting of the ice shelves and the mass balance of Antarctica. *Journal of Glaciology*, **38**(130), 375–387.

Jacobs, S., MacAyeal, D. M., and J.L. Ardai, J., 1986: The recent advance of the ross ice shelf, antarctica. *Journal of Glaciology*, **32**(112), 464–474.

Joughin, I., Abdalati, W., and M., F., 2004a: Large fluctuations in speed on greenland's jakobshavn isbrae glacier. *Nature*, **432**, 608–610.

Joughin, I., MacAyeal, D. R., and Tulaczyk, S., 2004b: Basal shear stress of the Ross ice streams from control method inversions. *Journal of Geophysical Research (Solid Earth)*, **109**(B18), 9405. doi:10.1029/2003JB002960.

Keys, H. J. R., Jacobs, S., and Brigham, L., 1998: Continued northward expansion of the Ross Ice Shelf, Antarctica. *Annals of Glaciology*, **27**.

King, E., 1994: Observations of a rift in the Ronne Ice Shelf, Antarctica. *Journal of Glaciology*, **40**(134).

Krimmel, R., 2001: Photogrammetric data set, 1957-2000, and bathymetric measurements for columbia glacier, alaska. Inv. Rpt. 01-4089, USGS Water-Resource.

Larour, E., Rignot, E., and Aubry, D., 2004a: Modelling of rift propagation on Ronne Ice Shelf, Antarctica, and sensitivity to climate change. *Geophysical Research Letters*, **31**(16). doi:10.1029/2004GL020077.

Larour, E., Rignot, E., Aubry, D., and MacAyeal, D., 2004b: Processes Involved in the Propagation of Rifts on Ronne Ice Shelf. *Annals of Glaciology*.

Lawn, B., 1993: *Fracture of Brittle Solids*. Cambridge University Press, Cambridge.

Lazzara, M., Jezek, K., Scambos, T., MacAyeal, D., and Van der Veen, C., 1999: On the recent calving of icebergs from the Ross Ice Shelf. *Polar Geography*, **23**, 201–212.

MacAyeal, D., 1993: Binge/purge oscillations of the Laurentide ice sheet as a cause of the North Atlantic's Heinrich events. *Paleoceanography*, **8**(6), 775–784.

MacAyeal, D., Okal, E., Aster, R., Bassis, J., Brunt, K., L.M., C., Drucker, R., Fricker, H., Martin, S., Okal, M., Sergienko, O., Sponsler, M., and Thom, J., 2006: Transoceanic wave propagation links iceberg calving margins of Antarctica with storms in tropics and Northern Hemisphere. *Geophysical Research Letters*, **33**. doi:doi:10.1029/2006GL027235.

MacAyeal, D. R., Rignot, E., and Hulbe, C. L., 1998: Ice-shelf dynamics near the front of the Filchner-Ronne Ice Shelf, Antarctica, revealed by SAR interferometry: model/interferogram comparison. *Journal of Glaciology*, **44**, 419–428.

Malvern, L., 1969: *Introduction to the mechanics of a continuous medium*. Prentice-Hall Englewood Cliffs, NJ.

McMahon, K. L., and Lackie, M. A., 2006: Seismic reflection studies of the Amery Ice Shelf, East Antarctica: delineating meteoric and marine ice. *Geophysical Journal International*, **166**, 757–766. doi:10.1111/j.1365-246X.2006.03043.x.

Meier, M., 1985: *Photogrammetric determination of surface altitude, terminus position, and ice velocity of Columbia Glacier, Alaska.* USGPO; For sale by the Distribution Branch, US Geological Survey.

Meier, M. F., and Post, A., 1987: Fast tidewater glaciers. *Journal of Geophysical Research*, **92**, 9051–9058.

Mercer, J. H., 1978: West Antarctic ice sheet and CO2 greenhouse effect: a threat of disaster. *Nature*, **271**, 321–325.

Meylan, M., Squire, V., and Fox, C., 1997: Toward realism in modeling ocean wave behavior in marginal ice zones. *Journal of Geophysical Research. C. Oceans*, **102**, 22.

Muskett, R., Lingle, C., Tangborn, W., and Rabus, B., 2003: Multi-decadal elevation changes on Bagley Ice Valley and Malaspina Glacier, Alaska. *Geophysical Research Letters*, **30**(16).

Nadai, A., 1950: *Theory of flow and fracture of solids: vol. 1.* McGraw-Hill.

Nemat-Nasser, S., Oranratnachai, A., and Keer, L. M., 1979: Spacing of water-free crevasses. *Journal of Geophysical Research*, **84**, 4611–4620.

Norton, F., 1929: *The Creep of Steel at High Temperatures.* McGraw-Hill, New York.

Nye, J., 1957: The Distribution of Stress and Velocity in Glaciers and Ice-Sheets. *Proceedings of the Royal Society of London. Series A, Mathematical and Physical Sciences*, **239**(1216), 113–133.

O'Neel, S., Pfeffer, W., Krimmel, R., and Meier, M., 2005: Evolving force balance at Columbia Glacier, Alaska, during its rapid retreat. *Journal of Geophysical Research*, **110**, F03012.

Oppenheimer, M., 1998: Global warming and the stability of the West Antarctic Ice Sheet. *Nature*, **393**(6683), 325–332.

Padman, L., Fricker, H., Coleman, R., Howard, S., and Erofeeva, L., 2002: A new tide model for the Antarctic ice shelves and seas. *Annals of Glaciology*, **34**(1), 247–254.

Paterson, W., 1994: *The Physics of Glaciers.* Reed Educational and Professional Publishing Ltd, Oxford, third edition edition.

Phillips, H. A., 1998: Surface meltstreams on the Amery Ice Shelf, East Antarctica. *Annals of Glaciology, vol.27, pp.177-181*, **27**, 177–181.

Poupinet, G., Ellsworth, V., and Frechet, J., 1984: Monitoring velocity variations in the crust using earthquake doublets: An application to the Calaveras fault, California. *Journal of Geophysical Research*, **89**(B7), 5719–5732.

Price, J., 2003: Dimensional analysis of models and data sets. *American Journal of Physics*, **71**(5), 437–447.

Rasmussen, L., and Meier, M., 1982: Continuity Equation Model of the Predicted Drastic Retreat of Columbia Glacier, Alaska. *Available from Supt. of Documents, GPO, Washington DC 20402, Price,$ 3. 50. Professional Paper 1258-A, 1982. 23 p, 22 Fig, 3 Tab, 12 Ref.*

Rasmussen, L., and Meier, M., 1985: Surface Topography of the Lower Part of Columbia Glacier, Alaska, 1974-1981. *Available from Dist Branch USGS 604 S. Pickett St. Alexandria, VA 22034. USGS Professional Paper 1258-E, 1985. 63 p, 17 fig, 8 tab, 20 ref.*

Reches, Z., and Lockner, D. A., 1994: Nucleation and growth of faults in brittle rocks. *Journal of Geophysical Research*, **99**(B9), 18,159–18,173.

Reeh, N., 1968: On the calving of ice from floating glaciers and ice shelves. *Journal of Glaciology*, **7**, 215–232.

Reid, H., 1910: *The Mechanics of the Earthquake.* Carnegie institution of Washington.

Reynolds, R., and Smith, T., 1981: Lakes on george vi ice shelf. *Polar Record*, **20**, 425–432.

Rignot, E., and MacAyeal, D., 1998: Ice-shelf dynamics near the ice front of the Filchner-Ronne Ice Shelf, Antarctica revealed by sar interferometry. *Journal of Glaciology*, **44**(147).

Rignot, E., Vaughan, D. G., Schmeltz, M., Dupont, T., and Macayeal, D., 2002: Acceleration of Pine Island and Thwaites Glaciers, West Antarctica. *Annals of Glaciology*, **34**, 189–194.

Rist, M. A., Sammonds, P. R., Oerter, H., and Doake, C. S., 2002: Fracture of Antarctic shelf ice. *Journal of Geophysical Reseach*, **107**(B1). doi: 10.1029/2000JB000058.

Robin, G. D. Q., 1979: Formation, flow, and disintegration of ice shelves. *Journal of Glaciology*, **24**, 259–271.

Rott, H., Skvarca, P., and Nalger, T., 1996: Rapid Collapse of the Northern Larsen Ice Shelf, Antarctica. *Science*, **271**, 788–792.

Saleur, H., Sammis, C., and Sornette, D., 1996: Discrete scale invariance, complex fractal dimensions and log-periodic fluctuations in seismicity. *Journal of Geophysical Research*, **101**(B8), 17,661–17,677.

Sanderson, T., 1979: Equilibrium profile of ice shelves. *Journal of Glaciology*, **22**(88), 435–460.

Scambos, T., Hulbe, C., and Fahnestock, M., 2003: Climate-Induced Ice Shelf Disintegration in the Antarctic Peninsula. *Antarctic Research Series*, **79**, 79–92.

Scambos, T., Sergienko, O., Sargent, A., MacAyeal, D., and Fastook, J., 2005: ICESat profiles of tabular iceberg margins and iceberg breakup at low latitudes. *Geophysical Research Letters*, **32**, L23S09.

Scambos, T. A., Bohlander, J. A., Shuman, C. A., and Skvarca, P., 2004: Glacier acceleration and thinning after ice shelf collapse in the Larsen B embayment, Antarctica. *Geophys. Res. Lett.*, **31**(18). doi:10.1029/2004GL020670.

Scambos, T. A., Hulbe, C., Fahnestock, M., and Bohlander, J., 2000: The link between climate warming and break-up of ice shelves in the Antarctic Peninsula. *Journal of Glaciology*, **46**, 516–530.

Scholz, C. H., 2002: *The Mechanics of Earthquakes and Faulting.* Cambride University Press, 2nd edition edition.

Schroeder, W., and Shephard, M., 1988: Geometry-based fully automatic mesh generation and the Delaunay triangulation. *International Journal for Numerical Methods in Engineering*, **26**, 2503–2515.

Schulson, E. M., 2001: Brittle failure of ice. *Engineering Fracture Mechancis*, 1839–1887. doi:10.1016/S0013-7944(01)00037-6.

Shearer, P., 1997: Improving local earthquake locations using the L1 norm and waveform cross correlation: Application to the Whittier Narrows, California, aftershock sequence. *J. Geophys. Res*, **102**, 8269–8283.

Shearer, P., 1999: *Introduction to Seismology.* Introduction to Seismology, by Peter Shearer, pp. 272. ISBN 0521660238. Cambridge, UK: Cambridge University Press, September 1999.

Shepherd, A., Wingham, D., Payne, T., and Skvarca, P., 2003: Larsen Ice Shelf Has Progressively Thinned. *Science*, **302**, 856–859. doi:10.1126/science.1089768.

Shepherd, A., Wingham, D. J., Mansley, J. A. D., and Corr, H. F. J., 2001: Inland Thinning of Pine Island Glacier, West Antarctica. *Science*, **291**, 862–864.

Shimazaki, K., and Nakata, T., 1980: Time-predictable recurrence model for large earthquakes. *Geophysical Research Letters*, **7**(4), 279–282.

Skvarca, P., de Angelis, H., Naruse, R., Warren, C. R., and Aniya, M., 2002: Calving rates in fresh water: new data from southern Patagonia. *Annals of Glaciology, vol.34, pp.379-384*, **34**, 379–384.

Smith, R. B., 1977: Formation of folds, boudinage and mullions in non-Newtonian materials. *Geological Society of America Bulletin*, **88**, 312–320.

Squire, V., Dugan, J., Wadhams, P., Rottier, P., and Liu, A., 1995: Of Ocean Waves and Sea Ice. *Annual Review of Fluid Mechanics*, **27**(1), 115–168.

Strutt, J., 1871: On the light from the sky, its polariztion and colour. *Philosophical Magazine*, **41**, 107–120.

Sturm, M., Hall, D., Benson, C., and Field, W., 1992: Glacier-terminus fluctuations in the Wrangell and Chugach mountains resulting from non-climate controls. Technical report, AD-P-007334/6/XAB, Army Cold Regions Research and Engineering Lab., Fort Wainwright, AK (United States).

Taylor, J., 1997: *An introduction to error analysis.* University Science Books Mill Valley, Calif.

Thomas, R., Abdalati, W., Frederick, E., Krabill, W., Manizade, S., and K., S., 2003: Investigation of surface melting and dynamic thinning on jakobshavn isbrae, geenland. *Journal of Glaciology*, **49**(165), 231–239.

Thomas, R., Rignot, E., Casassa, G., Kanagaratnam, P., Acuña, C., Akins, T., Brecher, H., Frederick, E., Gogineni, P., Krabill, W., Manizade, S., Ramamoorthy, H., Rivera, A., Russell, R., Sonntag, J., Swift, R., Yungel, J., and Zwally, J., 2004: Accelerated Sea-Level Rise from West Antarctica. *Science*, **306**, 255–258. doi:10.1126/science.1099650.

Turcotte, D. L., and Schubert, G., 2002: *Geodynamics.* Geodynamics, by Donald L. Turcotte and Gerald Schubert, pp. 472. ISBN 0521661862. Cambridge, UK: Cambridge University Press, March 2002.

Van der Veen, C., 1996: Tidewater calving. *Journal of Glaciology*, **42**, 375–385.

Van der Veen, C., 1998: Fracture mechanics approach to penetration of surface crevasses on glaciers. *Cold Regions Science and Techology*, **27**, 31–47.

Van der Veen, C., 1999: *Fundamentals of glacier dynamics.* Balkema.

Van der Veen, C. J., 2002: Calving glaciers. *Progress in Physical Geography*, **26**(1), 96–122.

Vaughan, D. G., 1993: Relating the occurance of crevasses to surface strain rates. *Journal of Glaciology*, **39**(132), 255.

Vaughan, D. G., and Doake, C. S. M., 1996: Recent atmospheric warming and retreat of ice shelves on the Antarctic Peninsula. *Nature*, **379**, 328–331.

Velicogna, I., and Wahr, J., 2006: Measurements of Time-Variable Gravity Show Mass Loss in Antarctica. *Science*, **311**, 1754–1756. doi:10.1126/science.1123785.

Vening Meinesz, F., 1950: Les graben africains resultant de compression ou de tension dans la croute terrestre. *Inst. R. Coll. Belge Bull*, **21**, 539–552.

Wadhams, P., 1986: The seasonal ice zone. *The Geophysics of Sea Ice*, 825–991.

Wadhams, P., 2000: *Ice in the Ocean*. Gordon and Breach Science Publishers, Amsteldijk.

Watts, A., 2001: *Isostasy and Flexure of the Lithosphere*. Cambridge University Press.

Weertman, J., 1974: Depth of water-filled crevasses that are closely spaced. *Journal of Glaciology*, **13**, 544–544.

Withers, M., Aster, R., Young, C., Beiriger, J., Harris, M., Moore, S., and Trujillo, J., 1998: A comparison of select trigger algorithms for automated global seismic phase and event detection. *Bulletin of the Seismological Society of America*, **88**(1), 95.

Young, N., and Hyland, G., 2002: Velocity and strain rates derived from InSAR analysis over the Amery Ice Shelf, East Antarctica. *Annals of Glaciology*, **34**, 229–234.